Sede Amministrativa: Università degli Studi di Padova

Facoltà di Scienze MM. FF. NN.

Dipartimento di Fisica "Galileo Galilei"

SCUOLA DI DOTTORATO DI RICERCA IN:

SCIENZA ED INGEGNERIA DEI MATERIALI

INDIRIZZO UNICO

CICLO XXII

MECHANISM OF FLUORINE REDISTRIBUTION AND INCORPORATION DURING SOLID PHASE EPITAXIAL REGROWTH OF PRE-AMORPHIZED SILICON

Direttore della Scuola: Ch.mo Prof. Gaetano Granozzi

Supervisore: Dott. Enrico Napolitani

Dottorando: Massimo Mastromatteo

To my family

Alla mia famiglia

Mechanism of Fluorine redistribution and
incorporation during Solid Phase Epitaxial
Regrowth of pre-amorphized Silicon
Massimo Mastromatteo
Ph.D. Thesis - University of Padova
Printed the 31th of January 2010

“Two things fill the mind with ever-increasing wonder and awe, the more often and the more intensely the mind of thought is drawn to them: the starry heavens above me and the moral law within me.”

“Due cose riempiono l'animo di ammirazione e venerazione sempre nuova e crescente, quanto più spesso e più a lungo la riflessione si occupa di esse: il cielo stellato sopra di me, e la legge morale in me.”

(Immanuel Kant)

“All truths are easy to understand once they are discovered; the point is to discover them.”

“Tutte le verità sono facili da capire una volta che sono state scoperte; il punto è scoprirle.”

(Galileo Galilei)

The work described in this thesis was mainly performed at the National Research & Development Center of *MAterials and Technologies for Information, communication and Solar energy* (MATIS), within the *National Institute for the Physics of Matter* (INFM) – *Italian National Research Council* (CNR), at the Department of Physics of the University of Padova (Italy) and at the Department of Physics and Astronomy of the University of Catania (Italy).

Abstract

The redistribution of impurities during phase transitions is a widely studied phenomenon that has a great relevance in many fields and especially in microelectronics for the realization of Ultra Shallow Junctions (USJs) with abrupt profiles and high electrical activation. The redistribution of fluorine during solid phase epitaxial regrowth (SPER) of pre-amorphized Si has been experimentally investigated, explained and simulated, for different F concentrations and temperatures. We demonstrate, by a detailed analysis and modelling of F secondary ion mass spectrometry chemical concentration profiles, that F segregates in amorphous Si during SPER by splitting in three possible states: i) a diffusive one that migrates in amorphous Si; ii) an interface segregated state evidenced by the presence of a F accumulation peak at the amorphous-crystal interface; iii) a clustered F state. The interplay among these states and their roles in the F incorporation into crystalline Si are fully described in this thesis. It is shown that diffusive F moves by a trap limited diffusion and interacts with the advancing interface by a sticking-release dynamics that regulates the amount of F segregated at the interface. We demonstrate that this last quantity regulates the regrowth rate by an exponential law. On the other hand we show that nor the diffusive F nor the one segregated at the interface can directly incorporate into the crystal but clustering has to occur in order to have incorporation. This is in agreement with the element specific structural information on the F incorporated in crystalline Si given by a specific X-ray absorption spectroscopy analysis performed in this thesis, and also with recent experimental observations, reported in literature. The trends of the model parameters as a function of the temperature are shown and discussed obtaining a clear energetic scheme of the F redistribution in pre-amorphized Si. The above physical understanding and the model could have a strong impact on the use of F as a tool for optimising the doping profiles in the fabrication of ultra-shallow junctions.

Abstract

La redistribuzione di impurezze durante le transizioni di fase è un fenomeno ampiamente studiato che ha una grande rilevanza in molti campi di ricerca e specialmente nella microelettronica per la realizzazione di giunzioni ultra sottili (USJs) caratterizzate da profili di drogante ben confinati e da un'alta attivazione elettrica.

La redistribuzione del fluoro durante la ricrescita epitassiale in fase solida (SPER) del silicio pre-amorfizzato è stata studiata sperimentalmente, descritta e simulata in un ampio range di concentrazioni di F impiantato e temperature di ricrescita. Mediante una dettagliata analisi modellizzazione matematica dei profili in concentrazione di F misurati tramite la spettrometria di massa di ioni secondari, dimostriamo che il F segrega in silicio amorfo durante la SPER suddividendosi in tre possibili stati: i) uno stato diffusivo che migra in silicio amorfo; ii) uno stato segregato all'interfaccia evidenziato dalla presenza di un picco di accumulazione di F all'interfaccia amorfo-cristallo; iii) uno stato di F clusterizzato.

Questo lavoro ha descritto nel dettaglio quali scambi avvengono tra questi stati e che ruolo hanno nell'incorporazione del F nel silicio cristallino. È stato osservato che il F diffusivo è soggetto ad una diffusione limitata dalle trappole presenti nel substrato amorfo. Il F che diffonde in amorfo interagisce con l'interfaccia che avanza tramite una dinamica di tipo "attacca-stacca", che regola l'ammontare del F segregato all'interfaccia. Dimostriamo che questa ultima quantità regola la velocità di ricrescita tramite una legge esponenziale. Dall'altra parte noi mostriamo che né il F diffusivo né quello segregato all'interfaccia possono incorporarsi direttamente nel cristallo ma del clustering deve accadere per avere l'incorporazione del F. Questa osservazione è in accordo con le informazioni strutturali del F incorporato in Silicio cristallino ottenute da una specifica analisi tramite spettroscopia di assorbimento a raggi X svolta in questa tesi e anche con le recenti osservazioni sperimentali riportate in letteratura. Gli andamenti dei parametri del modello in funzione della temperatura sono mostrati e discussi ottenendo un chiaro schema energetico della redistribuzione del F in silicio pre-amorfizzato. La suddetta comprensione fisica dei meccanismi coinvolti e il relativo modello predittivo da noi sviluppato potrebbero avere una forte impatto sull'uso del F come strumento per ottimizzare i profili dei droganti nella fabbricazione di giunzioni ultra-sottili.

CONTENTS

Introduction 11

Chapter 1 – Review on point defect engineering and the use of Fluorine in Silicon 17

1.1 Points defects in Silicon 18

1.2 Dopant diffusion in equilibrium conditions 20

1.3 Dopant diffusion in non-equilibrium conditions 26

1.3.1 The Transient Enhanced Diffusion 28

1.3.2 Boron Interstitial Clustering (BIC) 31

1.4 Solid Phase Epitaxial Regrowth (SPER) 32

1.5 Point defect engineering 41

1.5.1 Use of He and vacancy engineering 42

1.5.2 Pre-amorphization implant (PAI) method 44

1.5.3 Dopant diffusion and de-activation post SPER 45

1.6 PAI with C 46

1.7 PAI with F 48

1.7.1 F as a trap for Is: F – V clusters 51

1.7.2 F effect on the SPER rate 55

1.7.3 F segregation at the a-c interface 56

1.7.4 F diffusion in a-Si 58

1.7.5 F in corporation in c-Si 60

Chapter 2 – Experimental 65

2.1 Experimental methodology 66

2.2 Sample preparation 67

2.3 Thermal Processes 70

2.3.1 Furnace annealing 71

2.3.2 Rapid Thermal Annealing (RTA) 71

2.4 Sample Characterization 73

2.4.1 Secondary Ion Mass Spectrometry (SIMS) 73

2.4.2 High Resolution X-Rays Diffraction (HRXRD) 76

2.4.3 X-Ray Absorption Spectroscopy (XAS) 77

Chapter 3 – Results and discussion 81

3.1 Experimental evidences 82

3.1.1 SIMS profiles 82

3.1.2 The analysis of a typical F segregated peak 88

3.1.3 Formation of SiF_4 molecules is a-Si and their incorporation in c-Si 93

3.2 The rate equations model 98

3.2.1 F clustering in a-Si 98

3.2.2 F diffusion in a-Si 102

3.2.3 F segregation at the a–c interface 106

3.2.4 The complete model 112

3.2.5 The C++ code 114

3.2.6 The simulations results 117

3.3 Discussion and interpretation of the results 123

3.3.1 The parameters relative to the F diffusion in a-Si 124

3.3.2 The parameters relative to the F segregation at the a-c interface 126

3.3.3 The parameters relative to the F retardation effect on the SPER rate 128

3.3.4 The parameters relative to the F clustering in a-Si 130

Conclusions 137

Appendix 139

References 151

List of Publications 161

Acknowledgements 163

Introduction

Nowadays, microelectronics has a big presence and impact in our daily life with its products (personal computers, notebooks, mp3 players, phone mobiles, ...) and has changed a lot of economical and industrial fields with its inventions and applications. All of that would not be possible without the invention of the first transistor at the Bell Laboratories in 1947 and the realization of the first integrated circuit at both the Texas Instruments and the Fairchild Company twelve years later. These inventions revolutionized the electronic industry and created a new scientific field: microelectronics, exactly. Microelectronics studies the manipulation and elaboration of information by means of electrons and manufactures devices based on semiconductors with electronic components which are very small (in the micrometer-scale, but also smaller). The most used semiconductor is silicon. Silicon is a very abundant element in nature and it has a very good electrical, thermal and mechanical stability. Its peculiarity is to have a native oxide (SiO_2) that is an effective electric insulator with high chemical stability, unlike other semiconductors, i.e. germanium. One of the more used device is the Metal-Oxide-Semiconductor Field-Effect Transistor (MOSFET). In Fig. I.1 a MOSFET with p-channel is shown.

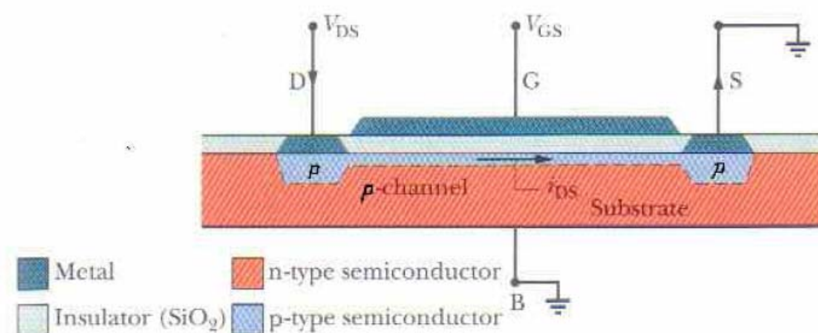

Figure I.1: *Schematic representation of a p-MOS.*

The MOS transistor is constituted by a n-type Si substrate with a low dopant level (~ 10^{15} at/cm^3) and two p-type Si zones with a high dopant level ($10^{18} \div 10^{20}$ at/cm^3), called source (S) and drain (D). The source region provides a supply of mobile charge when the device is

turned on. The region between source and drain at surface level is called channel. Over the channel there is another electrode called gate (G) but they are divided by an insulating silicon oxide layer. When a voltage is applied to the gate and it is higher than a threshold voltage, a conductive channel is formed between the source and the drain under the oxide, modifying the distribution of charges and turning on the device. If a voltage is applied between the source and the drain, a current will flow in the conductive channel. Reducing the gate voltage at a lower value than the threshold one, the conductive layer can be removed. Building in the same substrate simultaneously two complementary MOS transistors, one p-MOS and one n-Mos, a Complementary MOS (CMOS) is produced. CMOS is the most common device of modern integrate circuits because it has ability to reduce the current leakage considerably.

A phenomenological law that regulates the scaling in the design of the microelectronics devices, the Moore's law (Fig. I.2), is very famous.

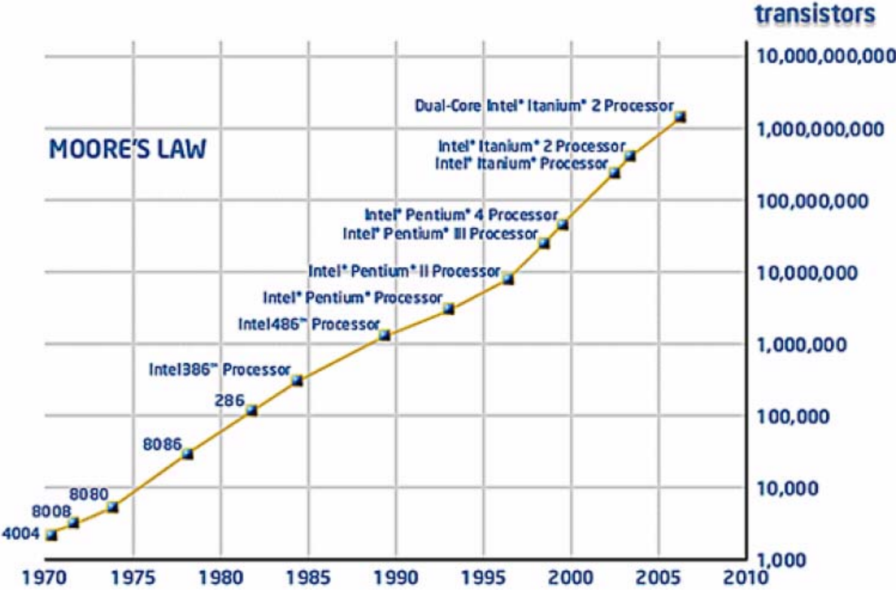

Figure I.2: *Representation of the Moore's law: number of transistor in a processor vs. years.*

It affirms that the number of transistors contained on a square inch of silicon doubled every 12 months. This law was almost followed by microelectronics industry even if with a different time step of doubling every 18 months. Notwithstanding, the main economical consequence was the reduction of the price of transistors by a factor of two every 18 months, reducing the production costs and permitting the mass production.

Device scaling down needs to the reduction of all vertical and lateral dimensions of the transistor. Scaling the width and depth of source and drain regions decreases the free charge with a consequent undesired increase in device resistance. In order to avoid this effect,

the scaling down should be accompanied by an increase of the free charge concentration in source and drain regions. The charge in source and drain regions is given by adding dopant atoms to the silicon substrates.

The most used technique to introduce dopants in silicon controlling precisely and independently dopants fluencies or positions is ion implantation. The ion implantation is a process in which energetic charged particles are introduced into targets with enough energy to penetrate beyond the surface. The energetic ions of the implant can remove Si atoms from their locations in the lattice in a series of displacement collisions, producing an extremely large number of Si point defects. The penetration depth is determined by the energy of the incident ions, the angle of incidence and the target. The dopants can be introduced by ion implantation at concentrations higher than their solubility limits. In order to electrically activate the implanted dopant, a post-implantation annealing is necessary because impurities needs enough thermal energy to reach substitutional lattice positions. The thermal annealing also annihilates the damage produced by the implant favouring the lattice reconstruction. In B implants at concentration more than 10^{18} at/cm^3, electrically inactive and stable clusters form around the B concentration peak. The B clusters are a big limitation to the design of ultra shallow junctions with abrupt profiles and high electrical activation, wished to satisfy the continuous scaling down of the devices. Beside an enhanced diffusion with respect to the equilibrium one happens for the doping elements (i.e. B and P) during the thermal annealing. This phenomenon is called Transient Enhanced Diffusion (TED) and causes a significant abruptness of the junction. The origin of TED is understandable considering the microscopical mechanism that regulates the B diffusion in silicon. The B diffusion in Si is mediated by native point defects constituted by self-interstitials (Si atoms in non-substitutional positions) and the B mobile concentration is proportional to self-interstitials concentration. TED happens when there is a non equilibrium concentration of self-interstitials, i.e. after ion implantation that introduces extra interstitials in the lattice, and persists until the complete dissolution of the implant damage determining its transient behavior.

In the last decades, different methods were created and developed to reduce or eventually avoid the TED. The more effective solutions are vacancy and point defect engineering, or the Pre-Amorphization Implant (PAI) followed by Solid Phase Epitaxial Regrowth (SPER). In the PAI method the crystal is pre-amorphized by a Si or Ge implant in the Si substrate; then dopants are implanted in the amorphous layer avoiding channeling effect and not introducing further damage of the crystal. Subsequently, the substrate is re-

crystallized during anneal process by SPER. After such process, very high concentration of electrically active dopants are achieved far above equilibrium (also more than 10^{20} at/cm^3). However, PAI method is not exempt by undesired effects. During post-annealing treatments, TED and B clusters are again observed experimentally. They are arisen by the interaction between dopant and defects originated after the amorphization implant and the SPER. In fact not all the layer damaged by the implant accumulates enough damage to transit to the amorphous state, and a deep tail of the implant left a crystalline region beyond the amorphous-crystal interface supersaturated by interstitials. During the thermal annealing necessary to re-crystallize the amorphous layer by SPER and electrically activate the dopant, these interstitials either diffuse away or precipitate beyond the original a-c interface into extended defects, called end of range defects (EOR).

B electrical deactivation, caused by TED and B clusters formation, can be reduced by trapping or annihilating self-interstitials introducing C or F between B implant and the EOR damage. Using C or F in the correct way, the TED can be also eliminated. While the trapping ability of F is well known and studied, a little is known about the microscopical mechanisms that induce and govern the redistribution of F during the SPER.

The main aim of this work is to describe and model the redistribution of fluorine during solid phase epitaxial regrowth (SPER) of pre-amorphized Si. The physical phenomena concerning F diffusion and segregation in amorphous silicon and F incorporation in crystal silicon are investigated experimentally, explained and simulated for different F concentrations and SPER temperatures. The final goal is to create an overall mathematical model able to predict the entire evolution of F chemical profiles in a wide range of concentrations and SPER temperatures starting from the as-implanted profile.

This thesis is organized as follows. In Chapter 1 a briefly review on the point defect engineering is reported. In particular, the dopant diffusion will be described in equilibrium and not equilibrium conditions and how it depends on the interactions between dopant and silicon point defects. The microscopical mechanisms that govern TED and B clustering will be explained. Then different point defect engineering methods able to reduce TED will be presented, especially the PAI method followed by SPER. SPER will analyzed in details according to its more actual description proposed in literature. Lastly, the effects of the C or F

co-implantation will be shown, with a particular attention on the known behavior of F during the SPER of a pre-amorphized Silicon.

In Chapter 2 the set up of the experimental work is outlined. The concentration profiles of the implanted samples will be described and shown. The samples preparation and the techniques used to characterize them will be reported.

In Chapter 3 the results of the samples characterization are reported and discussed. These results will be the basis of a predictive model able to simulate the F redistribution during Si SPER, that will described in details in this Chapter. Then the simulations obtained by the model will be compared to experimental data and the parameters of the model will be discussed with the aim to describe more deeply that physics of this system.

After the Chapter 3, conclusion and future work will be reported.

Lastly, in Appendix, the preliminary results about our recent study about H segregation and redistribution during SPER of a pre-amorphized Silicon will be presented and discussed. This work is the result of the collaboration, that I promoted, between our research group and the group of B. C. Johnson from School of Physics of the University of Melbourne (Australia).

This Ph.D. thesis is the result of my work carried at the Dipartimento di Fisica dell'Università di Padova within a research collaboration with the MATIS CNR-INFM centre at the Dipartimento di Fisica ed Astronomia di Catania. I list below my personal contribution to the different part of the work.

I participated actively at the design and implementation of the experiments. I carried out autonomously part of the processing of the samples, namely all the thermal processes, that where done with the conventional furnace and the rapid thermal processing apparatus located within the Dipartimento di Fisica. I have made all the analysis of experimental data except the XAS analysis. I have given a significant contribution to invent the model of the system studied in this work. I tested the C++ code that we have used to simulate this system, for each version of the code on our experimental data to verify its reliability, to minimize the number of free parameters and to understand any possible changes to the code, suggesting some improvements of the model. Finally, I have participated in the discussion and interpretation of the results.

During my Ph.D. I participated also at the research activity about B diffusion in crystalline Germanium and the characterization of defects in Ge made by MATIS CNR-INFM

at the Dipartimento di Fisica dell'Università di Padova and at the Dipartimento di Fisica ed Astronomia di Catania, simulating the diffusive phenomena and realizing thermal processes.

Chapter 1

REVIEW ON POINT DEFECT ENGINEERING AND THE USE OF FLUORINE IN SILICON

Doping is one of the crucial operations in the design and fabrication of Si-based devices. In this Chapter of literature review, after an exposition about the different types of point defects in Si and their interactions with dopants, critical obstacles for the realization of ultra-shallow junctions (USJs) with high electrical activation, as Transient Enhanced Diffusion (TED) and B clustering, will be presented. Then some possible solutions to reduce or avoid these hindrances will be shown such as vacancy engineering, using of He, and, most importantly, the pre-amorphization implant (PAI) method.

In particular, the PAI method for USJs design consists in introducing dopant by ion implantation in a pre-amorphized Si substrate and then re-crystallizing it by Solid Phase Epitaxial Regrowth (SPER). Such method allows, for suitable process conditions, to obtain shallower and more electrically active junctions than those realized by implanting the dopant directly in c-Si. However, even in regrown PAI Si samples TED and electrical deactivation after post-annealing treatments happen. TED can be reduced or even suppressed by adding by ion implantation other impurities such as C or F. After a short review about the beneficial effect of C co-implant, a deepen analysis about the state of the art understanding of F effects in PAI Si will be reported.

1.1 POINTS DEFECTS IN SILICON

The crystal structure of silicon is diamond cubic with a lattice parameter of 0.543 Å. At temperature higher than 0 K silicon, as all crystalline solids, contains native point defects due to fundamental principles of the thermodynamics [Hu]. In a crystal, a point defect is defined as a deviation from the regular periodicity of the lattice in a single lattice position.

Point defects can exist in the pure silicon lattice, *native point defects*, or be introduced by foreign impurities into the silicon lattice, *impurity-related defects*. Point defects can be present in a charged or neutral electronic state.

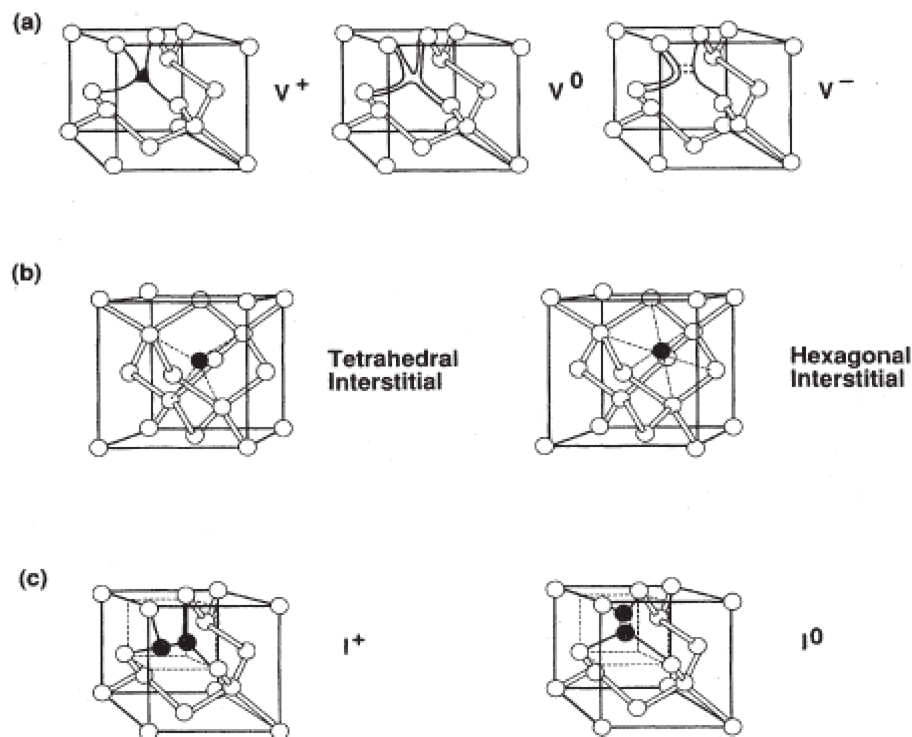

Figure 1.1: Example of possible *native point defects configurations in Si according to reference [Fahey].* **(a**) *Vacancy in the +, 0 and – charged state.* **(b)** *Dark spheres indicate atoms in two different interstitial positions.* **(c**) *Interstitialcy in the + and 0 charged state. [Fahey]*

There are three types of native point defects in crystalline silicon: the vacancy, the interstitial and the interstitialcy. A *vacancy* (V) is a lattice site with a missing atom. The vacancy defect can be in the positive, neutral and negative state [Fig. 1.1(a)] depending on how the resultant unsatisfied bonds have reconfigured themselves to accommodate the vacancy in the lattice. A *silicon-* or *self-interstitial* (I) is a Si atom placed anywhere in a crystal except at a lattice site, although for energetic reasons there is only a limited number of

such off-lattice potential locations for Is. Figure 1.1(b) shows the two possible interstitial positions with the highest symmetry: the tetrahedral configuration and the hexagonal one. The *silicon-* or *self-interstitialcy* defect consists of two Si atoms in non-substitutional positions configured around a lattice atom: it is formed by placing an extra atom around a substitutional lattice site even if two possible configurations are likely as shown in Fig. 1.1(c). Commonly, silicon interstitial or interstitialcy are considered as self interstitials, silicon interstitials or, simply, interstitials (Is) without a clear distinction between them because both are extra Si atoms. In the crystal lattice, small clusters of Is and Vs, complexes made with point defects and impurity atoms or other extended defects can be present.

Two mechanisms are responsible for native point defect generation: the Frenkel process and the Schottky process. The Frenkel process occurs when a Si atom leaves spontaneously its substitutional site in a perfect crystal silicon and it produces a vacancy generating the so-called Frenkel pairs, i.e. a vacancy-interstitial couple:

$$0 \Leftrightarrow V + I \tag{1.1}$$

The reverse process, equally probable, is called annihilation. In a finite crystal with a significant surface to volume ratio, vacancies and interstitials are generated independently of each other by the Schottky process. In terms of net result, a V is generated by moving a lattice atom in the bulk to the surface and attaching it to a kink of a surface step so as to conserve the surface area and kink density, and hence the surface free energy of the crystal while the volume of the crystal has increased by one atomic volume; an I is created next to the surface when an atom moves towards the bulk. Other mechanisms may alter the net generation and annihilation rates of point defects, such as: chemical reaction at the silicon surface, precipitation of impurities dislocations, radiation damage, ion implantation and so on [Fahey] (see Section 1.3).

The equilibrium concentrations of these point defects are determined by their enthalpies and entropies of formation and are thermodynamically defined functions of temperature, stress and electron concentration. A point defect increases the energy of the system, introducing a structural distortion in the lattice, and its entropy, contributing to the disorder of the whole system. So, for temperatures higher than 0 K the free energy changes with the formation of point defects N_X, where X could be V or I alternatively, in a lattice of N_L lattice sites as [Hu]:

$$\Delta G_X = N_X(-\Delta S_X^f T + \Delta H_X^f) - k_B T \ln \frac{N_L!}{N_X!(N_L - N_X)!} \tag{1.2}$$

where ΔS_X^f and ΔH_X^f are the vibrational entropy and the enthalpy (associated to lattice distortions) variation for the single point defect formation, respectively; k_B is the Boltzmann's constant and T is the absolute temperature. Since the vacancies and interstitials can be generated independently of each other, the minimum of the free energy variation $\Delta G_V + \Delta G_I$ is achieved by minimizing with respect to vacancies and interstitials independently, obtaining the equilibrium point defect concentrations [Hu]:

$$c_X^{eq} = N_L \theta_X \exp\left(\frac{\Delta S_X^f}{k_B}\right) \exp\left(-\frac{\Delta H_X^f}{k_B T}\right) \quad (1.3)$$

where θ_X is the number of internal degrees of freedom of the X defect on a lattice site (for example, spin degeneracy).

So, the presence of point defects is thermally activated and the concentrations of interstitials (Is) and vacancies (Vs) in equilibrium conditions are not necessarily equal; in fact they were founded experimentally to be [Bracht95]:

$$c_I^{eq} \cong 2.9 \times 10^{24} \exp\left(-\frac{3.18 eV}{k_B T}\right) cm^{-3}, \quad (1.4)$$

and

$$c_V^{eq} \cong 1.4 \times 10^{23} \exp\left(-\frac{2.0 eV}{k_B T}\right) cm^{-3}. \quad (1.5)$$

Their concentrations depend strongly on the temperature. For example, for T = 1000 °C the equilibrium concentrations of Is and Vs are about 7.5 x 10^{11} at/cm^3 and 1.7 x 10^{15} at/cm^3, respectively. These values are rather low compared to the silicon concentration in the lattice, i.e. 5 x 10^{22} at/cm^3 and are negligible at room temperature. So the native point defects are not a big obstacle in the working of Si-based devices; however they start to have a huge role in the atomic diffusion phenomena of impurities in silicon at higher temperatures than room temperature and/or in non equilibrium conditions.

1.2 DOPANT DIFFUSION IN EQUILIBRIUM CONDITIONS

The introduction and the substitutional incorporation of dopants in the lattice allow to modify some physical proprieties of the silicon making it suitable for electrical applications. A crucial issue for the production of electronic devices is the control of the dopants

incorporation and diffusion processes because of the scaling down of the Si–based devices dimensions.

The basic equations governing diffusion in solids are called Fick's first and second law of diffusion in which the diffusion of a quantity is generally driven by a concentration gradient: atoms will diffuse from regions of high concentration to region of low one. The first law, presented here in the one dimensional case for simplicity, describes the impurity flux, J, as:

$$J = -D\frac{\partial C}{\partial x} \tag{1.6}$$

where D is the constant of proportionality called diffusion coefficient or diffusivity and C refers to the impurity concentration. The time dependence of C is given by the so-called continuity equation (the Fick's second law):

$$\frac{\partial C}{\partial t} = \frac{\partial}{\partial x}\left(D\frac{\partial C}{\partial x}\right) \tag{1.7}$$

Figure 1.2 shows two simple microscopic mechanisms responsible for the diffusion of impurities in crystalline solids, that are referred as "direct" diffusion mechanisms.

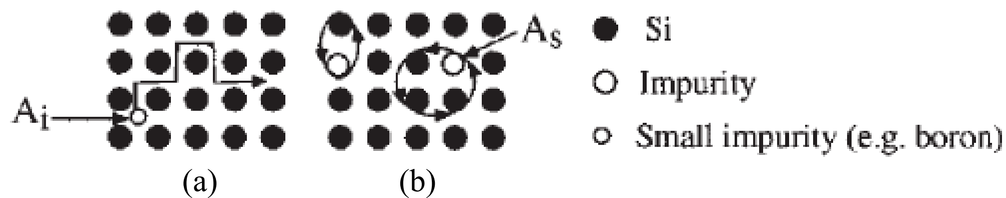

Figure 1.2: *Schematic two-dimensional representation of direct diffusion mechanisms in solid of* **(a)** *an interstitial element A,* A_i*, or* **(b)** *substitutionally dissolved one,* A_s*.*

As described in Fig. 1.2, in the case of impurities that are dissolved mainly interstitially in the lattice, i.e. hydrogen in silicon, the diffusion proceeds via interstitial lattice sites without involving any point defects [Fig. 1.2(a)]. Another direct diffusion happens when atoms on substitutional sites exchange their positions with an adjacent Si atom or by means of a ring mechanism [Fig. 1.2(b)]. However direct mechanism for substitutionally dissolved impurities in semiconductors are rare, and their diffusion mechanisms, as will be described in the following, are usually more complex than the ones depicted in Fig. 1.2.

The equilibrium diffusion coefficient D of impurities in solid follows generally an Arrhenius behavior [Fahey]:

$$D = D_0 \exp\left(-\frac{E_D}{k_B T} \right) \tag{1.8}$$

where D_0 is the pre-exponential factor and E_D is the activation energy of the process, k_B is the Boltzmann's constant and T is the absolute temperature.

In Fig. 1.3 the diffusion coefficients of a lot of impurities in crystalline silicon, compared with silicon self-diffusion, are plotted against the reciprocal of the temperature. The elements that diffuse via the direct interstitial mechanism (H, O and metals as Cu, Ni, Fe) are indicated by short-dashed lines. The diffusivities of the common dopants (B, Sb, P, As) and the isovalent impurities (Ge and C) are also indicated by continuous lines. Their diffusivities are always much slower than the ones of other impurities ones, but faster than Si self-diffusion, irrespective of the impurity's atomic radius, whether it is smaller or larger than Si.

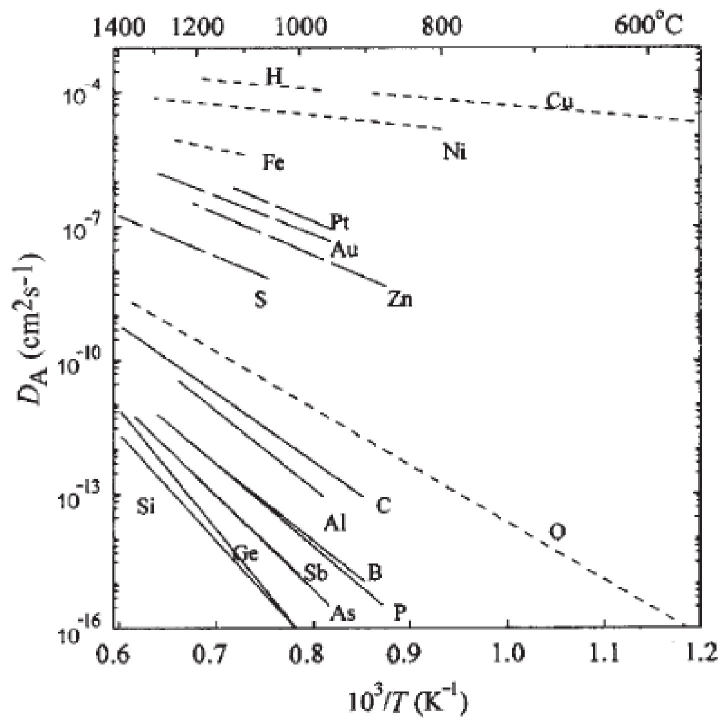

Figure 1.3: *Temperature dependence of the diffusion coefficient of foreign atoms (A) in Si, compared with self-diffusion. The elements that diffuse via the direct interstitial mechanism are indicate by short-dashed lines. Long-dashed lines concern hybrid elements, which are mainly dissolved on the substitutional lattice site, but their diffusion proceeds via a minor fraction in an interstitial configuration. Solid lines represent elements that are mainly dissolved substitutionally and diffuse via the vacancy or interstitialcy mechanism [Bracht00].*

Their diffusion mechanisms are indirect mechanisms mediated by native point defects, Vs and Is. Various indirect diffusion mechanisms are described by the following reactions, in which a substitutional impurity (A) interacts with native point defects (I or V), and represented in Fig. 1.4:

$A_S + V \leftrightarrow AV$ vacancy mechanism (1.9)

$A_S + I \leftrightarrow AI$ interstitialcy mechanism (1.10)

$A_S \leftrightarrow A_i + V$ dissociative mechanism (1.11)

$A_S + I \leftrightarrow A_i$ kick-out (1.12)

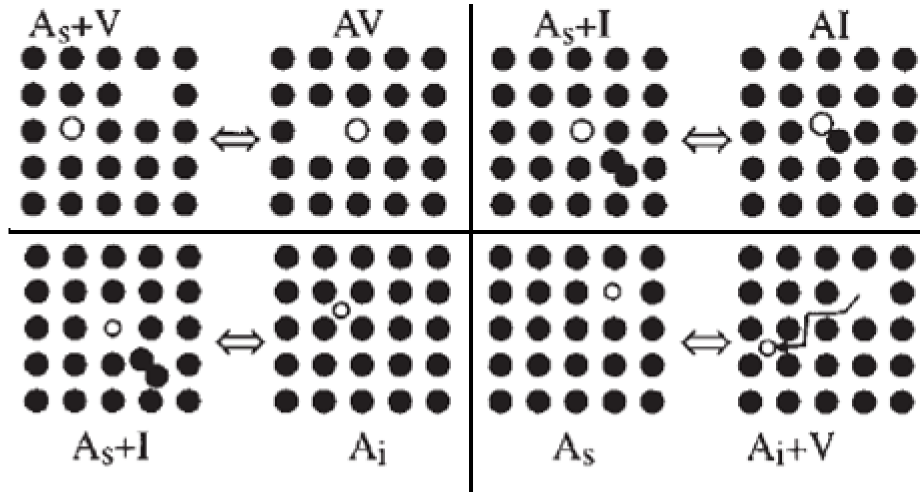

Figure 1.4: *Schematic two-dimensional representation of indirect diffusion mechanisms of an element A in solid. A_i, A_s, V and I denote interstitially and substitutionally dissolved foreign atoms, vacancies and silicon self-interstitials, respectevely. AV and AI are pairs of A with the corresponding defects [Bracht00].*

In Eqs. (1.9) and (1.10) a substitutional impurity joins with native point defects creating a diffusive species and these reactions are called the vacancy and interstitialcy mechanisms, respectively. The AI and AV pairs can migrate in some cases for relatively long distance before dissociating through inverse. The Eq. (1.11) represents a dissociative mechanism where a substitutional impurity leaves a lattice site creating a mobile interstitial species and leaving behind itself a vacancy. The kick-out mechanism [Eq. (1.12)] occurs when a self-interstitial “kicks out” a substitutional impurity to an interstitial configuration in which the impurity can make more than one diffusion step before returning substitutional through the inverse reaction.The energetic scheme of the kick-out mechanism is shown in Fig. 1.5. The diagram represents the total energy of the system as a function of its configuration. At far left, the system consists of a crystal with a free surface and one substitutional impurity atom, A_S. Moving to the right, a self-interstitial is thermally generated at a large distance from the impurity atom. The energy of the system fluctuates while the self-interstitial migrates between adjacent stable locations in crystal, until the self-interstitial encounters and reacts with the substitutional dopant atom A_S. This event produces a mobile dopant species A_i, able to migrate for some distance before dissociating and returning again substitutional.

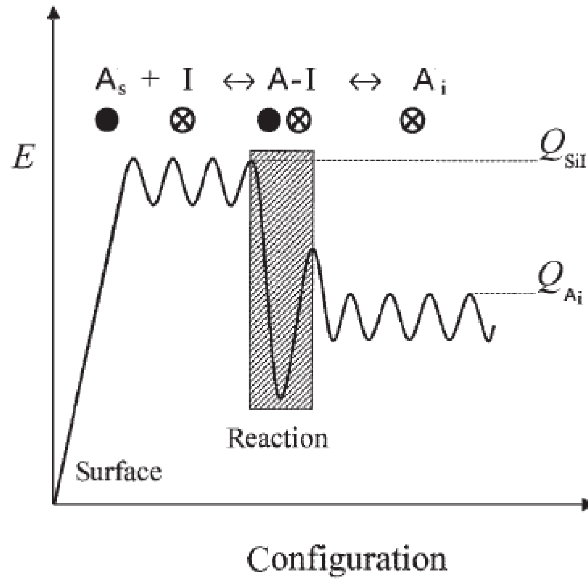

Figure 1.5: *Configuration diagram showing the energetic of interstitial-mediated dopant diffusion [Cowern99].*

The energetic scheme for the interstitialcy mechanism is exactly the same as the one described in Fig 1.5 except for the mobile species that it is AI instead of A_i. In the following we will make no distinction between the two phenomena as they are almost identical from an experimental point of view. Their key feature is that they produce a diffusivity that is proportional to the concentration of self-interstitials. Correspondently a mechanism mediated by vacancies [Eq. (1.9)] is responsible for a diffusivity proportional to the concentration of vacancies. The dissociative mechanism of Eq. (1.11) is uncommon in semiconductors.

Therefore, in general the diffusivity of a silicon dopant or a isovalent impurity (A) is mediated by vacancies and interstitials. So the diffusivity can be written as follows:

$$D_A = D_A^{AV} + D_A^{AI} \qquad (1.13)$$

where D_A^{AV} and D_A^{AI} are the contributions to the dopant A diffusivity due to a V-type mechanism or a I-type one, respectively. From the ratio between a single component to the total diffusivity, the fractional point defect component of diffusion, ϕ_X, can be defined as:

$$\phi_X = \frac{D_A^{AX}}{D_A} \qquad (1.14)$$

where X could be V or I.

This quantity is characteristic for each element and depends on the temperature. In Fig. 1.6, ϕ_I is plotted for some common silicon dopants, as also for C, Ge and Si, as a function of their atomic radius normalized to the Si one at the temperature of 1100 °C. While Ge and Si,

having ϕ_I approximately equal to 0.5, have the vacancy and interstitial related components to their diffusion in Si, species as C and B diffuses in crystal Si essentially by Is.

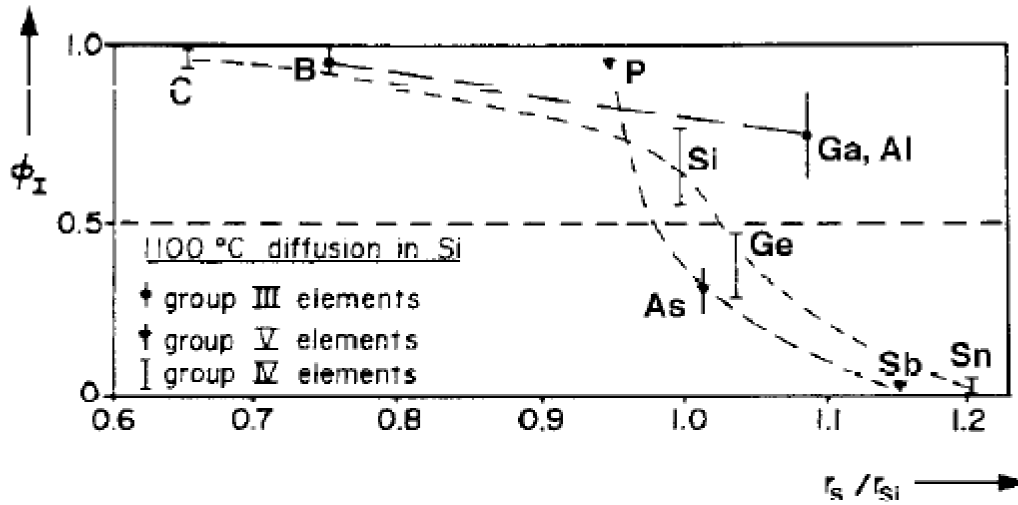

Figure 1.6: *Interstitial-related fractional diffusion components ϕ_I for group III, IV and V elements versus their atomic radius in units of the atomic radius r_{Si} for Si [Gösele].*

The first experimental evidences of the interstitial-mediated diffusion mechanism of the B in crystal Si were presented by Cowern *et al.* [Cowern90, Cowern91] at the beginning of the 90's. They found with a detailed and accurate experimental and modelling work that in particular conditions the diffusion profile of a B spike does not show the expected Gaussian broadening predicted by a Fickian diffusion, but it has exponential-like tails (Fig. 1.7).

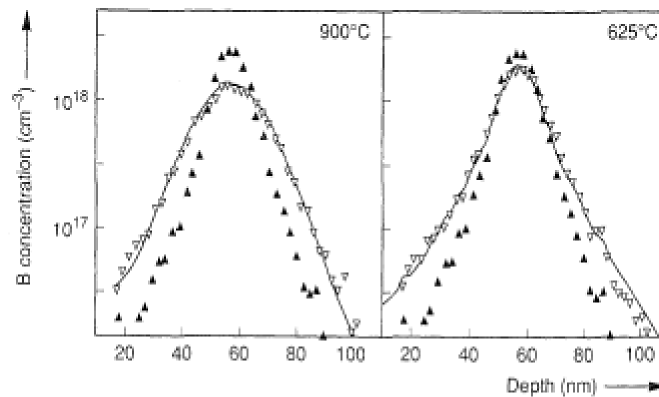

Figure 1.7: *Comparison to diffused MBE-grown B delta at 900 °C (5 min in N_2 ambient, rapid annealing) and at 625 °C (110h, in O_2 dry ambient). Solid symbols indicated the as-grown B profile and open symbols represent the profile after diffusion [Cowern91].*

These exponential-like tails were attributed to a B diffusion via an intermediated species according to the kick-out mechanism [Eq. (1.12)]. The kick-out reaction has a direct reaction

frequency called g that is proportional to the concentration of self-interstitials, C_I, as expressed by Eq. (1.15):

$$g = g^* \frac{C_I}{C_I^*} \tag{1.15}$$

where * refers to equilibrium conditions.

After B has become diffusive, it can move in the lattice for a migration length, λ, before returning substitutional through the inverse reaction (kick-in). Therefore the B diffusion does not follow the Fick's law and it is described by two parameters, g and λ. When the number of migration events per atom increases, i.e. for gt >> 1, the diffusion starts to be well approximated by the Fick's law, and in this case the coefficient diffusion is equal to [Cowern91]

$$D_B = g\lambda^2 \tag{1.16}$$

Recently, it was demonstrated by means of theoretical studies that B diffuses by an interstitialcy mechanism described by Eq. (1.12) [Sadigh, Windl].

Quite recently, it was demonstrated that the B diffusion occurs under interaction with I^0 or I^{++} interstitials. The reaction promotes the formation of BI^- and BI^+ interstitialcy that has to convert into BI^0 states (by getting or loosing a hole respectively) before diffusing. The I^{++} interaction channels dominate at high p-doping while the interaction with I^0 dominates in intrinsic or moderate doping [DeSalvador06, Bracht07].

1.3 DOPANT DIFFUSION IN NON EQUILIBRIUM CONDITIONS

The dopant diffusivity can be heavily influenced by a change in the equilibrium value of native point defects concentration. This concentration can be modified by chemical reactions at the silicon surface as the thermal oxidation or the thermal nitridation of Si [Fahey], that inject interstitials or vacancies, respectively. Another process able to alter the point defect concentration is ion implantation [Rimini].

Ion implantation is the best most used technique to introduce dopants in silicon, being able to control precisely and independently dopants fluencies or positions, also through oxide layers. The ion implantation is a process in which energetic charged particles are introduced into targets with enough energy to penetrate beyond the surface. The penetration depth is determined by the energy of the incident ions, the angle of incidence and the target structure and composition. Their final concentration profile follows roughly a Gaussian distribution

characterized by a projected range R_p (that indicates the average of the implanted ions position) and by the dispersion from R_p, ΔR_p. The total number of implanted ions, called dose or fluence, is given by the product of the total flux of incident ions and the implantation time. The implanted particles, before stopping, move with a random walk in the lattice and lose energy gradually by collision with Si lattice atoms and excitation and polarization of the substrate electron cloud. As only 10-25 eV of transferred energy is necessary to remove a Si atom from a lattice location, even at low energy, few keV ion can create a large number of substrate atoms displacements. For example, Montecarlo simulations [TRIM] predict that a 0.5 keV B implant in silicon should displace about 10 Si atoms per implanted ion, and such number increases considerably by increasing the ion energy and mass. Each displaced Si substrate atom gains energy in the collision and then moves through the crystal, causing its own path of damage. The total damage caused by a single implanted ion and the displaced substrate ions is called the collision cascade (Fig. 1.8).

In the region of the damage cascade, the crystalline Si is modified heavily from relatively perfect material with point defect concentrations at thermal equilibrium to highly disordered material with supersaturated concentrations of point defects like Si interstitials (Is) and vacancies (Vs), small interstitials and vacancies clusters, point defects-dopant atoms complexes, and amorphous pockets. The isolated point defects can migrate for long distances at room temperature and then stop their path if a I-V recombination happens, or I and V complexes form or they interact with impurities such as O and C and dopant atoms.

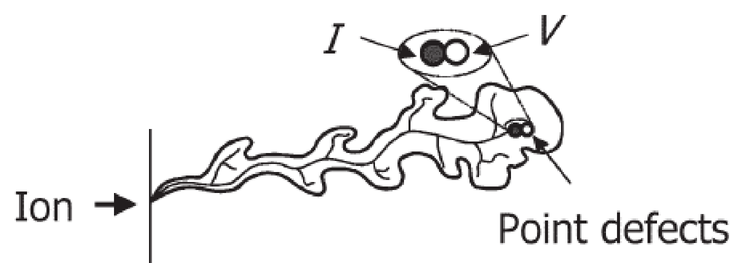

Figure 1.8: *Collision cascade induced by ion implantation in materials. An interstitial-vacancy pair is indicated.*

In order to electrically activate the implanted dopant, a post-implantation annealing is necessary, in order to annihilate the damage favouring the lattice reconstruction and give to impurities enough thermal energy to reach substitutional lattice positions. However, during this thermal annealing, an enhanced diffusion with respect to the equilibrium one happens for

the doping elements that diffuse essentially via mediated-interstitial mechanism (i.e. B and P). During the thermal treatment the recombination I + V → 0 initially prevails on the other reactions and only a few % of point defects survives recombination. Nevertheless, considering that the implanted dopant concentrations may be quite high, the residual point defect concentration may be still orders of magnitude higher than at the thermodynamic equilibrium. A simple model called "plus-one model" [Giles91] allows to calculate easily the number of self-interstitials survived after the post-implantation annealing, overcoming the great complexity of the implantation process. The model assumes that all processes involve Frenkel pairs (I-V) formation, except in the points where the implanted ions come at rest in interstitial positions. Thus, each ion creates n vacancies and (n+1) interstitials. After subsequent annealing all I-V pairs annihilate and only a number of interstitials equal to the dopant concentration survives. Recent experimental and theoretical studies showed that the ratio between the interstitials left after the Frenkel pairs recombination and the dose of implanted ions could be indeed slightly greater than one [Eaglesham95, Pelaz].

In conditions of non-thermal equilibrium for point defects concentrations, as after ion implantation, the diffusivity (D_B) of mediated-interstitial diffusing impurities, i.e. B, will be different to the diffusivity at equilibrium conditions (D_B^{eq}) being described by the following equation [Fahey, Bracht00]:

$$D_B \cong \frac{c_I}{c_I^{eq}} D_B^{eq} = S \cdot D_B^{eq} \tag{1.17}$$

where the ratio between the interstitial concentration and the one at equilibrium conditions is called "interstitial supersaturation", S. At the same time, a measure of the B diffusion can be used as an important tool to measure S in non-equilibrium conditions through Eq. (1.17).

1.3.1 The Transient Enhanced Diffusion

After ion implantation an enhanced diffusion with respect to the equilibrium one was observed and is called Transient Enhanced Diffusion (TED). This phenomenon has been extensively investigated and understood in the past decades [Michel, Cowern90, Chao, Napolitani99, Saleh]. In Fig. 1.9 the TED for a B implant in Si is shown.

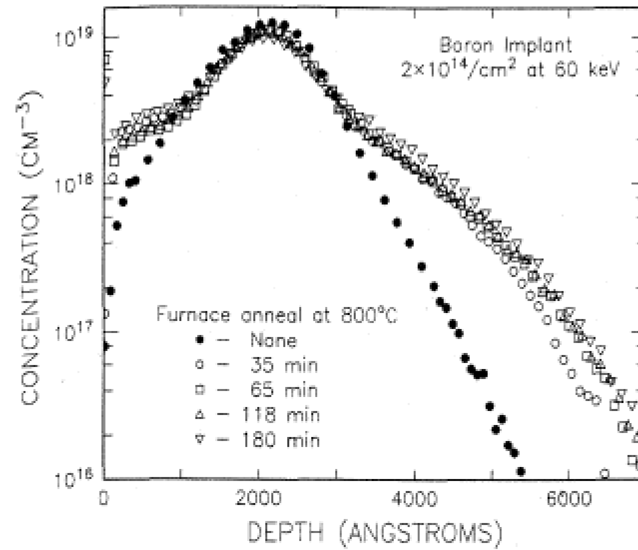

Figure 1.9: *B profiles for different times annealing at 800 °C, experimental evidence of TED [Michel].*

At 800 °C the most of B diffusion occurs in the first 35 min and this non-equilibrium diffusion does not occur for longer annealing, revealing its transient behavior. In fact TED happens until the implantation damage disappears by thermal annealing. The displacement below a B concentration of 10^{17} at/cm^3 is large, on the order of 150-200 nm, whereas the calculated equilibrium diffusion length for B diffusion in the same annealing conditions is ~ 2.5 nm [Fahey]. In addition, the enhanced diffusion occurs only below a concentration level of 2 x 10^{18} at/cm^3, which is about one order of magnitude below the solubility limit of B in Si at 800 °C. Above this concentration a B immobile and electrical inactive peak is present. The time duration and the intensity of the boron TED depend on the implantation dose and energy, annealing temperature and time. It is well established that the anomalous diffusion of ion implanted B arises from excess of Si self-interstitials that are generated by the implant. In fact, under TED conditions the initial interstitial supersaturation value S is approximately > 10^4 [see Eq. (1.17) and Fig. 1.10].

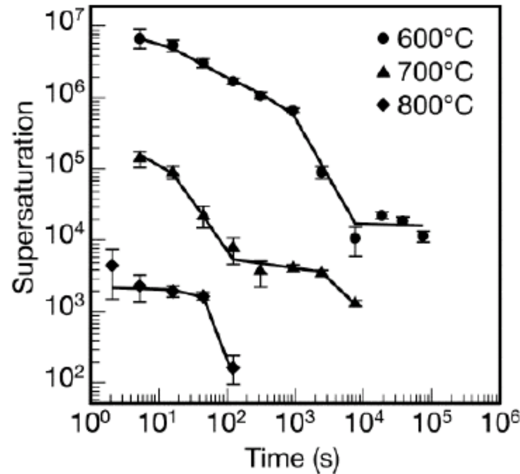

Figue 1.10: *Supersaturation of interstitials during annealing of a 2 x 10^{13} at/cm^2 40 keV Si^+ implant [Cowern99].*

The supersaturation of Si interstitials is high initially and then decreases with the annealing time, first rapidly and then slowly. The TED ends when S decays to the equilibrium concentration of the Is. During the first moments of the annealing, Is and Vs migrate to the surface, encounter one another and annihilate or form clusters. The clusters size increases with both increasing ion dose and annealing temperature.

Transmission electron microscopy (TEM) measurements demonstrated the existence of extend rod-like defects containing the excess interstitials in samples implanted with a few times 10^{13} at/cm^3 Si, as shown in Fig. 1.11 [Eaglesham94].

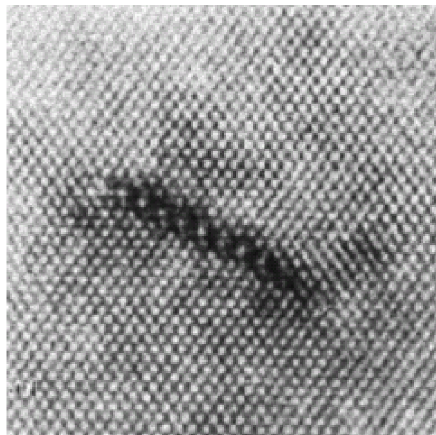

Figure 1.11: *Cross-section HREM showing {311} defect habit-plane, and typical image constrast of {311} defects [Eaglesham94].*

These extended defects are usually called {311} defects, because they run along [110] directions and consist of interstitials precipitating on {311} planes [Takeda]. Both sub-microscopic clusters and {311} clusters emit interstitials as they dissolve, enhancing the B

diffusion. At B low doses and energies, TED is driven by the annealing of small interstitial clusters [Cowern99b], while at higher doses and energies the majority of TED is caused by Is emitted by {311} defects [Eaglesham94].

During the annealing the smallest and less stable clusters dissolve favouring the growth of bigger and more stable clusters, following the Ostwald ripening process [Bonafos]. Therefore these defects sustain the local supersaturation of Is by emitting and recapturing Is during continued annealing. The rate at which this decay occurs is determined by the evaporation energy of Is from {311}, which TEM investigations of the clusters evolution determined to be (3.8 ± 0.2) eV [Stolk97]. This activation energy agrees with the energy determined from the decay of TED supersaturation (3.7 eV) [Solmi91], thus confirming once more the correlation between {311} dissolution and TED.

Increasing the implantation dose, above a threshold of ~ 10^{14} at/cm^2 but below the amorphization threshold, leads to the formation of other greater defect agglomerates (faulted Frank loops and perfect dislocations) that are more stable than {311} defects [Stolk97].

1.3.2 Boron Interstitial Clustering (BIC)

In addition to TED, another main obstacle to the realization of highly doped USJs is the formation of stable clusters of B and interstitials called BIC (Boron-Interstitials-Cluster). BICs are clusters such as B_nI_m with n B atoms and m interstitials atoms, that can be otherwise B and/or Si atoms. The formation of BICs is induced by the interaction of B with a supersaturation of Si, as after ion implantation. As shown in Fig. 1.9, it is possible to observe the immobile B peak at concentrations higher than 2 x 10^{18} at/cm^3. The peak region increases by increasing implant fluence and reduces by increasing the annealing temperature. B clustering reduces both the self-interstitial clusters formation and the TED of B [Mannino]. Such clusters transform one into the other in the formation (dissolution) process by two possible paths that are the capture (release) of an I or a B-I mobile species. B clustering is driven by the formation of precursor BI_2. Once a B-I pair is formed as a consequence of interstitialcy reaction [Eq. (1.10)], the high Is supersaturation leads to the formation of BI_2 through the reaction:

$$B - I + I \Leftrightarrow BI_2 \qquad (1.18)$$

This reaction inhibits the B diffusion and creates the nucleation centers for the formation of larger clusters by incorporating further I and/or B_I. If the amount of interstitials is low, as it is

the case at the end of TED, BICs increase in size by getting a B_I and rapidly releasing an I, thus lowering the I fraction (B_2I, B_2, B_3I, …). Hence, B clustering reduces TED in the earliest stage of annealing by absorbing interstitials, whereas it sustains non-equilibrium B diffusion for longer times even after the complete dissolution of {311} defects.
In fact the B clusters are quite stable with very high energetic barrier for dissolution. Small clusters (up to 4 B atoms) dissolve with an energy of about 3.2 eV [Mirabella03], while larger clusters, that form at high B concentration (above 5 x 10^{19} at/cm^3), are also more stable (4.83 eV) [Desalvador05].

Thus, in the B implanted c-Si, the Is cause not only the boron TED process but also the clustering of B atoms. These are huge limitations for the realization of USJs and several efforts have been made in order to reduce B diffusion and clustering. A lot of effective solutions have been developed in order to avoid these unwanted limiting effects, such vacancy [Smith] and point defect engineering [Shao], implantation in preamorphized Si [Jin, Pawlak04], and co-implantation with C [Cowern96, Napolitani01] or F [Downey98, Impellizzeri04], as we shall see.

Before to describe and compare these different methods of point defect engineering in Si, an extensive discussion about the Solid Phase Epitaxial Regrowth (SPER), the process that regulates the phase transition from amorphous to crystalline Si, will be presented in next Section. Such process is a fundamental step in the PAI method and will be crucial for the understanding of the present thesis work.

1.4. SOLID PHASE EPITAXIAL REGROWTH (SPER)

The re-organization of Si amorphous layers on a crystalline substrate was interesting and well-studied research issue for the material science community, from the first report about this in 1975 by Csepregi *et al.* [Csepregi75]. A lot of efforts were done to develop a comprehensive understanding of the kinetics and mechanism of solid phase transformation of amorphous silicon thin films in crystal.

It was observed that when an a-Si layer, realized as in our case by ion implantation, is at planar contact with the residual c-Si layer and is annealed, its re-crystallization starts and proceeds by the movement of the planar amorphous-crystal (a-c) interface layer by layer (Solid Phase Epitaxial Regrowth, SPER), as shown in Fig. 1.12. Under a continued annealing, the amorphous layer thickness reduces and the crystal thickness increases.

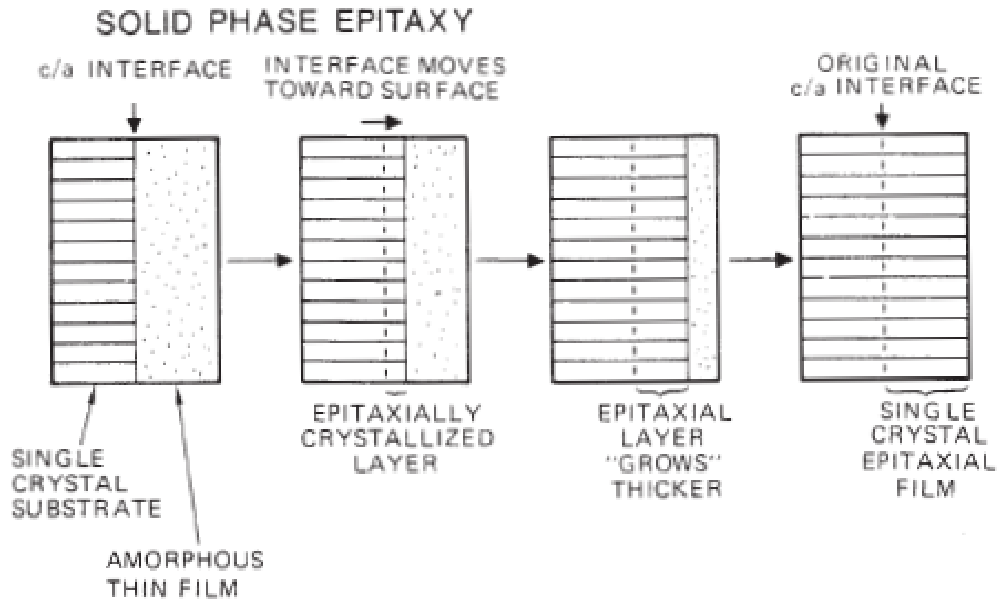

Figure 1.12: *Schematic illustration of the Solid Phase Epitaxial Regrowth (SPER) process in a-Si.*

The regrowth velocity depends on the annealing temperature, the substrate orientation, the doping and the stress applied on the Si substrate [Csepregi75, Olson, Williams, Rudawski08].

It was demonstrated experimentally that the Si SPER is a thermally activated process, well described by an Arrhenius-type plot [Olson]:

$$v = v_0 \exp\left(-\frac{\Delta G^*}{k_B T}\right) \tag{1.19}$$

where v_0 is the pre-exponential factor, ΔG^* is the activation energy of the process, k_B is the Boltzmann constant equal to of 8.617×10^{-5} eV/K and T is the absolute temperature.

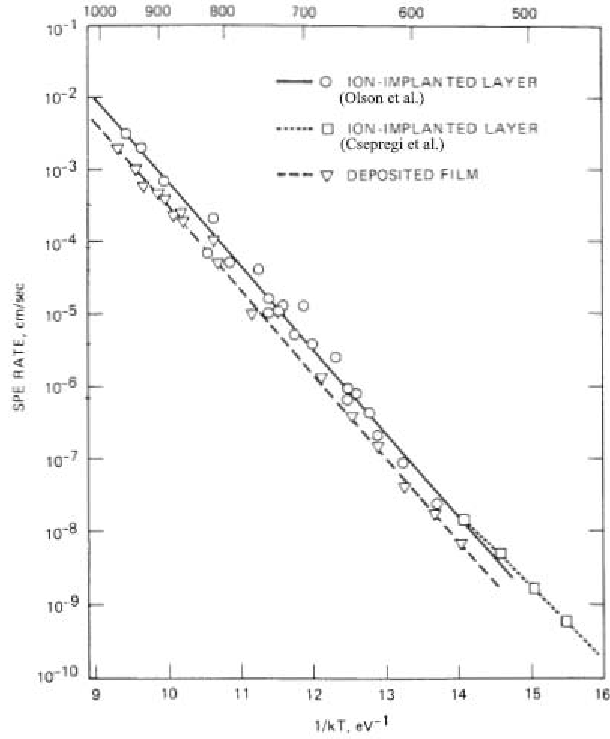

Figure 1.13: *Temperature dependence of intrinsic SPER rate in Si^+-implanted and e-beam evaporated (deposited) a-Si [Olson]. Low-temperature implanted film data of Csepregi et al. [Csepregi75] are also shown.*

The values of v_0 and ΔG*, deduced for Si^+-implanted layers, are $v_0 = 3.1 \times 10^{15}$ nm^2/s and ΔG* = (2.68 ± 0.05) eV [Olson]. For example, the SPER velocity is about 0.456 nm/s at 580 °C and 40.9 nm/s at 700 °C. The relationship described by Eq. (1.19) works well in an extremely wide range of rates (from ~ 10^{-3} to 10^5 nm/s) and temperatures (from ~ 500 °C to ~ 1000 °C), as well represented in Fig. 1.13. This suggests that the intrinsic solid phase epitaxial regrowth mechanism is the same over a broad temperature range.

According to thermodynamic considerations, the SPER process is energetically favored since the free Gibbs energy, G, of the system is lowered by the transformation of an interface atom from amorphous to crystalline phase (Fig. 1.14). As shown in Fig. 1.14, ΔG* is the energy difference between the free energy G_1, that the system has in the amorphous state, and the free energy G* at a transition state. The free energy difference between the initial and the final state has a negligible impact on v compared to ΔG [Olson]. As explained before, in the crystal Si atoms form strongly covalent and directional bonds and their configuration of minimum energy is achieved by having these bonds arranged in a tetrahedral configuration. Extending this arrangement in three dimensions, the diamond lattice characteristic of c-Si can be achieved. Although a-Si maintains a local order, arising from the strong energy minimum associated with tetrahedral bonding, on the contrary, it loses the long-range order seen in the

crystal (i.e. the order is lost already beyond two interatomic distances). The fact that the crystalline state has lower energy (Fig. 1.14) is the driving force inducing the local reorder of the bond angles and distances in a-Si.

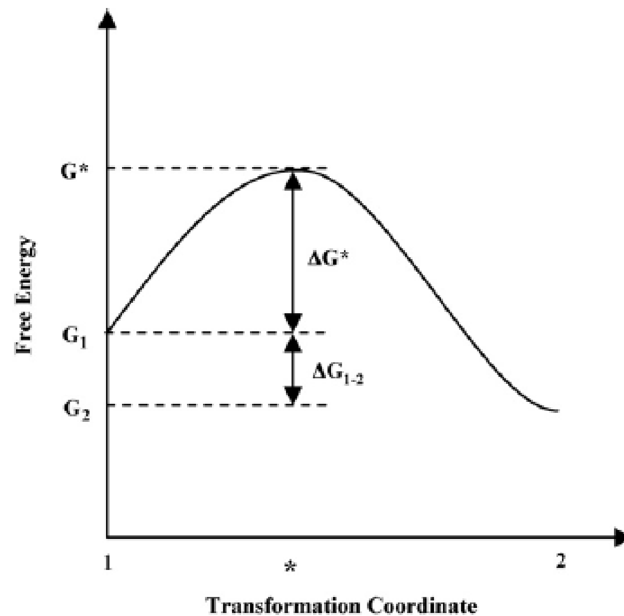

Figure 1.14: *Energetic scheme of a transformation between states 1 (in our case is a-Si) and 2 (c-Si) [Rudawski08b].*

Early atomistic SPER models were able to predict the orientation dependence of the SPER rate [Csepregi77]. Csepregi *et al.* suggested that the regrowth interface is resolved into minimum free energy {111} planes or terraces during regrowth and the crystallization proceeds via the propagation of [110] edges on this terrace interface surface [Csepregi77]. Spaepen and Turnbull [Spaepen] added that the interface should be highly saturated (i.e. with few unbounded atoms) and regrowth occurs via a bond-breaking process and a subsequent rearrangement along the [110] edges. Since the number of [110] edges on {111} oriented terraces strongly depends on crystal orientation, this description is useful to qualitatively explain the orientation dependence observed. However, this modelling approach did not predict the growth rate dependence on impurity concentration. In fact, the presence of the impurities concentration > 0.1 % can dramatically influence and modify the SPER rate [Olson]. Dopants of the groups III and V can greatly increase the SPER rate, but when both n-type and p-type dopants are present at the same time a compensation effect occurs [Suni82]. With the aim to explain the dopants effect on the SPER rate, Suni *et al.* [Suni82, Suni82b] suggested that the bond-breaking process is mediated by vacancies that form and migrate at the a-c interface. They related the concentration of charged vacancies to the position of the

Fermi level in the band gap and its dependence on doping concentration. However, this assumption has been ruled out due to the studies about the pressure dependence of the SPER rate [Lu90, Lu91]. Considering the pressure contribute to the energy difference ΔG*, it is possible to determine the change in volume, called activation volume, as:

$$\Delta V^* = -kT\frac{\partial \ln(v)}{\partial P}. \qquad (1.20)$$

Fitting the experimental Si or Ge SPER rates in function of pressure, Lu *et al.* estimated a negative activation. Since the experimental activation volume of vacancies in Si [Lu91] and in Ge [Werner] is positive, Suni's supposition was confuted. Notwithstanding, Suni *et al.* pointed out the attention to the correlation between rate enhancement and energy levels of dopant induced defect and the band gap.

Williams and Elliman [Williams], extending the Spaepen and Tunrbull's atomistic model, proposed that the defect, or "growth site" responsible for re-crystallization, is a kink along a [110] ledge (Fig. 1.15). Amorphous atoms at a kink site, unlike other atoms at the a-c interface, have at least two bonds with the crystalline phase. Kink nucleation and motion are the basic steps for the regrowth. They proposed that the Fermi level on the amorphous side of the a-c interface is pinned near midgap and the number of charged kink-related defects promoting SPER would be governed by the doping dependence of the Fermi level in c-Si. They did not specify the nature of the defects.

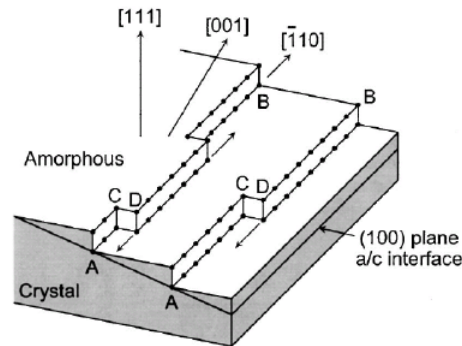

Figure 1.15: *Kink-like steps at the a-c interface. The lower part of the figure (gray) represents crystal, while the upper part is amorphous. The (001) a-c interface is composed of {111} oriented terraces; along the [110] ledges (AB), present on this terraced structure, kink steps (CD) form. The motion of these kinks (indicated by arrows) produces crystallization [Priolo90].*

Afterwards, Lu *et al.* [Lu91] considered the kink-site model to be a special case of the dangling bond model of Spaepen and Turnbull: kink motion occurs if bonds at the a-c interface break, locally rearrange and the dangling bonds recombinate. They reworked the

electronic aspects of the charge kink-site model, relaxing some of the assumptions which had been made. The reworked model is called Generalized Fermi Level Shift model (GFLS) [Lu91]. In the GFLS model, SPER is mediated by a neutral defect D^0 and its positively or negatively charged counterparts $D^{\pm}$ and the band structure and density of states determine their concentration. The model does not specify the nature of the defect, so it could be a dangling bond or some other defect with a negative activation volume. So, the SPER rate is expected to be proportional to the concentration of these defects. For a n-type semiconductor and its intrinsic counterpart, the velocities are given, respectively, by:

$$v \propto \left(\left[D^0\right] + \left[D^-\right]_{doped} \right) \tag{1.21}$$

and

$$v_0 \propto \left(\left[D^0\right] + \left[D^-\right]_{\text{int}rinsic} \right). \tag{1.22}$$

The charged fraction of defects is determined by Fermi-Dirac statistic, according to:

$$\frac{\left[D^-\right]_{doped}}{\left[D^0\right]} = g \cdot \exp\left(\frac{E_F - E^-}{k_B T} \right) \tag{1.23}$$

where E_F is the Fermi level and E^- represents the energy level within the band gap of the defect responsible for the SPER process, k_B has the usual meaning and T is the temperature. g is the degeneracy factor associated with E^- and depends on the internal degeneracies of the D^- and D^0 defect states. Recently, the GFLS model was further developed by using the actual best values for temperature and concentration dependences of the parameters involved [Johnson07] and by incorporating degenerate semiconductor statistics, band bending [Johnson07] and the role of the strain [D'Angelo].

In the attempting to identify the SPER mechanism, Molecular Dynamics (MD) simulations have been useful to discern between different proposed models. Early models attributed the re-crystallization to the motion of a dangling bond type defect [Saito81, Saito84], that induces rearrangement of atoms via bond breaking. More recently, Bernstein *et al.* [Bernstein98, Bernstein00], using empirical potential simulations, proposed that the SPER may occur through a number of both simple and complex mechanisms. One simple mechanism involves the rotation of two atoms aided by coordination defects which are locally created and annihilated during SPER and a more complex mechanism, indeed, involves the migration to the interface of a fivefold coordinated defect promoting the incorporation of two atoms into the crystal. The MD simulations suggest a doubt on the generally accepted idea that SPER is a single thermally activated process.

The most recent complete SPER description, developed by Rudawski *et al.* [Rudawski08, Rudawski08b] studying the stress dependence of SPER of ion implanted Si, affirms exactly that SPER starts from crystalline islands nucleation at the a-c interface and it proceeds by migration of kink-like growth site along [110] ledges (Fig. 1.16).

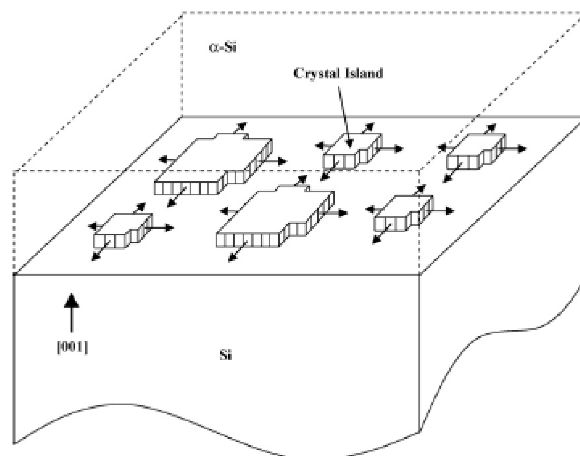

Figure 1.16: *Schematic of the defects-mediation model of [001] SPER [Rudawski08b].*

This interpretation is compatible with the previous models, but the substantial difference with respect to them is that nucleation and migration are two different processes that happen at the a-c interface. Until Rudawski *et al.*'s interpretation, ΔG* of 2.7 eV was attributable at the sum of kink nucleation and ledges migration. On the contrary, Rudawski *et al.* found experimentally that nucleation and migration processes have a ΔG* energy equal to (2.5 ± 0.1) eV and (2.7 ± 0.1) eV, respectively. These values approach to the Si-Si bond energy (~2.5 eV) very much. The reason would be that, on the most basic level, SPER consists in the rearrangement breaking and reforming Si-Si bonds. However, they noticed that, in absence of any stress, the nucleation is the limiting step for the regrowth having a pre-factor of two orders of magnitude higher than the migration one. The difference between nucleation energy and the accepted value of ΔG* = 2.7 eV may be related to the larger relative portion of ramp-up time to total anneal time in higher temperature samples as well as the larger error in SPER rates observer with in-plane tension at higher temperatures. The difference between nucleation and migration pre-factors may be related to the relative scales or geometry of the two processes. In the case of nucleation, presumably only small groups of atoms must rearrange to form a crystal island to start growth, while in the case of migration large numbers of atoms along the island ledges are involved in continuing growth (coordinated motion).

An extensive model of the intrinsic Si SPER under stress was developed considering a lot of experimental evidences [Aziz, Rudawski08, Rudawski08b, Rudawski09]. The model

affirms that if a stress state, σ_{ij}, is applied on the sample, the SPER rate described by Eq. (1.19) will become:

$$v = v_0 \exp\left(\frac{-\Delta G^*}{kT}\right)\exp\left(\frac{\sigma_{ij}\Delta V_{ij}^*}{kT}\right), \qquad (1.24)$$

where *i* and *j* refer to axes in the coordinate frame of Ref. [Aziz]: in particular, when *i, j* = 1 or 2, they refer to a-c interface plane directions and when *i, j* = 3 to the perpendicular direction to the interface. $\Delta V_{ij}*$ is called activation strain tensor and it is the volumetric deformation between the initial and transition states. $\Delta V_{ij}*$ can be estimated by

$$\Delta V_{ij}^* = kT\frac{\partial \ln(v)}{\partial \sigma_{ij}}. \qquad (1.25)$$

Hence, a positive (negative) value of $\sigma_{ij}\ \Delta V_{ij}*$ product decreases (increases) of the activation barrier and an increase (decrease) of the SPER rate. A recent complete study showed extensively what happens applying external stress and inducing SPER rate on a-Si samples [Rudawski08b]. Under hydrostatic pressure the SPER rate increases by increasing pressure, as showed in Fig. 1.17, while ΔV_h* was estimated to be – 0.28 Ω (Ω is the atomic volume of Si) separately [Lu91]; so Eq. (1.24) remains true.

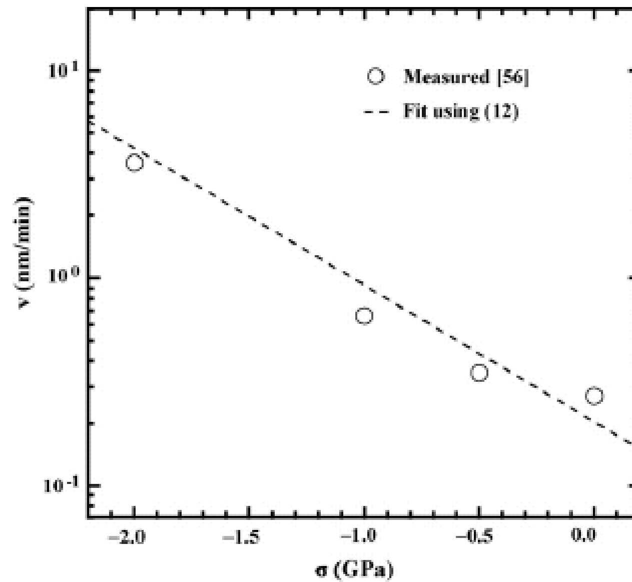

Figure 1.17: *Plot of SPER velocity vs. σ at 500 °C as measured using RBS [Nygren]*

In the case of uniaxial stress on the a-c plane, the observations are surprisingly different than those of hydrostatic stress. Uniaxial compression ($\sigma_{11} < 0$) causes retardation where as hydrostatic pressure causes enhancement. The experimental data of SPER rate under uniaxial

compression can be modelled assuming a positive $\Delta V_{ij}*$ in the interface plane coordinations equal to 0.15 Ω. So the complete $\Delta V_{ij}*$ tensor is equal to

$$\Delta V_{ij}^* = \begin{pmatrix} 0.15 & 0 & 0 \\ 0 & 0.15 & 0 \\ 0 & 0 & -0.58 \end{pmatrix} \Omega \tag{1.26}$$

assuming that

$$\Delta V_h^* = 2\Delta V_{11}^* + \Delta V_{33}^* . \tag{1.27}$$

All experimental evidences about SPER rate under uniaxial stress on the a-c plane can be resumed in Fig. 1.18, where the SPER rate is plotted vs. σ_{11}.

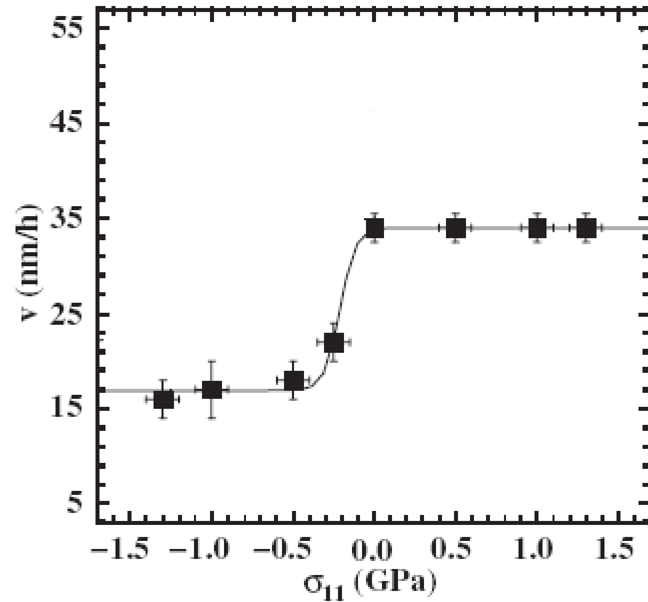

Figure 1.18: *Plot SPER rate (v) vs. σ_{11} at 525 °C[Rudawski08].*

A huge in-plane uniaxial compression can halve the intrinsic SPER rate (when $\sigma_{11} = 0$) while a stress oriented in the same direction but with $\sigma_{11} > 0$ does not modify the velocity. The explanation of these results can be accounted using the Rudawski *et al.*'s interpretation of SPER. The in-plane uniaxial stress influences only the migration of the islands' edges along the planar direction and does not modify the nucleation rate. In this way, a compressive stress suppresses the migration along the direction of the applied stress reducing the SPER rate also until a factor 2. A tensile stress speeds up the regrowth along one direction, but this fact does not change the global SPER rate because the nucleation event is the limiting step for the regrowth, as we discussed previously. In Fig. 1.19 an atomistic schematics of the in-plane SPER migration process is reported as exemplification.

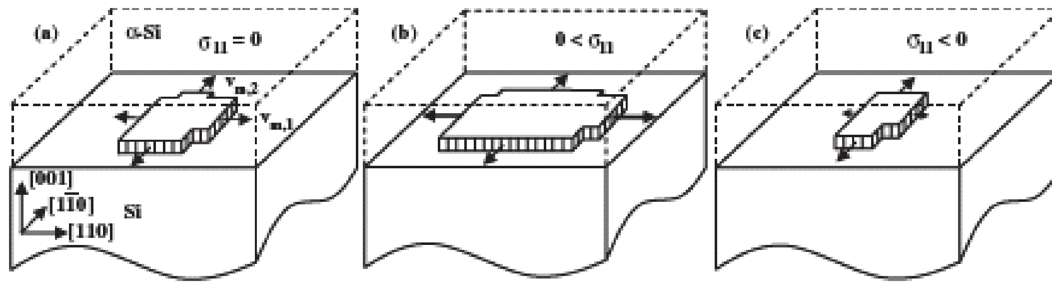

Figure 1.19: *Atomistic schematics of the in-plane SPER migration process with* **(a)** $\sigma_{11} = 0$, **(b)** $0 < \sigma_{11}$ **(c)** $\sigma_{11} < 0$ *[Rudawski08].*

This atomistic model will be used in Section 3.3 to explain how F retards the Si SPER rate.

While SPER of intrinsic silicon in presence of dopants or under stress is well modelled, instead little is known about the effect of non-doping impurities, i.e.: H, N, O, C and F. It is note that all of them retard SPER rate [Kennedy, Olson, Johnson04], but there is not any microscopical model explaining their behaviour. Rudawski *et al*. [Rudawski09] suggested that the nucleation kinetics are probably unaltered by electrically inactive species and they attributed the slowdown of SPER to the additional time needed to incorporate inactive impurities that tend to cause local lattice distortions incorporating non-substitionally. H and C have different behavior during the Si SPER: H segregates at the a-c interface while C incorporates substitutionally in c-Si. Both of them cause a linear reduction to the SPER rate in function of the impurity concentration at the a-c interface: H reduces the SPER rate by up to ~ 50% [OlsonHB] while when C concentration at the a-c interface is equal to ~ 5.6 x 10^{20} at/cm^3 the SPER is blocked [Mastromatteo]. For experimental observations of the F effect on the SPER rate, see Section 1.7.2.

1.5 POINT DEFECT ENGINEERING

The realization of Ultra Shallow Junctions (USJs) with abrupt profiles and high electrical activation has become an important technological challenging task [ITRS]. So it is fundamental to control the point defects populations in silicon to prevent their interactions with dopant atoms. In particular, as discussed before, the interstitials left by ion implantation evolve during the post-implantation annealing, as a function of many parameters: annealing temperature, energy and dose of the implantation. This evolution could result in interstitials

clustering, interactions of interstitials with impurities and, consequently enhanced diffusion of dopant, i.e. B and P, mainly because of Is influence on dopants diffusion. In this paragraph different methods created in order to avoid these undesired phenomena will be presented.

The aim of this thesis will be to deepen the understanding of a particular kind of point defect engineering i.e. the implantation in pre-amorphized Si method (explained in Section 1.5.2) with F co-implantation (Section 1.6).

1.5.1 Use of vacancy engineering and He

Vacancy engineering is a technique that uses a high energy silicon co-implant in c-Si (500 keV – MeV) before the dopant implant [Smith06]. The high energy ions transfer momentum to the host atoms causing the formation of Frenkel pairs (Is and Vs) and spatially separating Is and Vs: the net excess of Is is around the ion projected range and beyond, while the excess of Vs is close to the surface. When B is implanted in this vacancy engineered surface region, the excess of Vs annihilate the extra Is induced by B implant (see Section 1.3 about “plus-one model”), reducing the BICs formation and increasing the B electrical activation.

Another efficient method to trap Is is the He ion implantation in c-Si [Mirabella06, Bruno07, Bruno07b, Kilpelainen09, Kilpelainen09b]. High-dose implants of He stabilize, during subsequent annealing, vacancy-type defects produced by the implantation itself, leading to the formation of empty cavities (or voids), while He permeates out of the sample. In particular these V-type defects consist in a well defined layer of big cavities (10-50 nm in diameter) at the depth of the projected range (R_p) and an uniform band of very small cavities (nanovoids) centered at about half the R_p of He and extending from R_p to the surface, as shown in Fig. 1.20. These nanovoids are smaller than EOR deep voids but larger than divacancies.

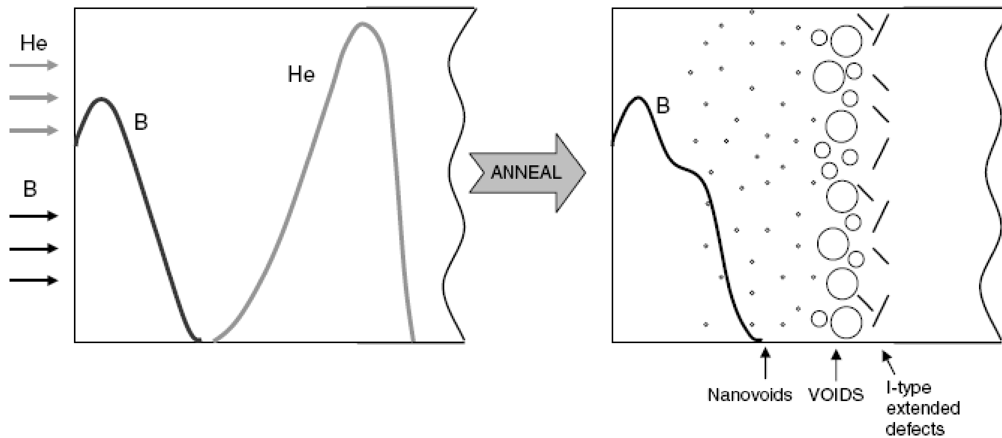

Figure 1.20: *Schematic of the creation of He induced voids and nanovoids and their effect on the B-implanted diffusion in c-Si. [Bruno07b]*

B diffusion becomes as more reduced as higher is the He implanted fluence. In Fig. 1.21 it is possible to observe how the induced voids reduce B diffusion: B profiles tend to assume a progressively narrower, steeper and higher shape, and B diffusing atoms accumulate where B diffusivity is reduced.

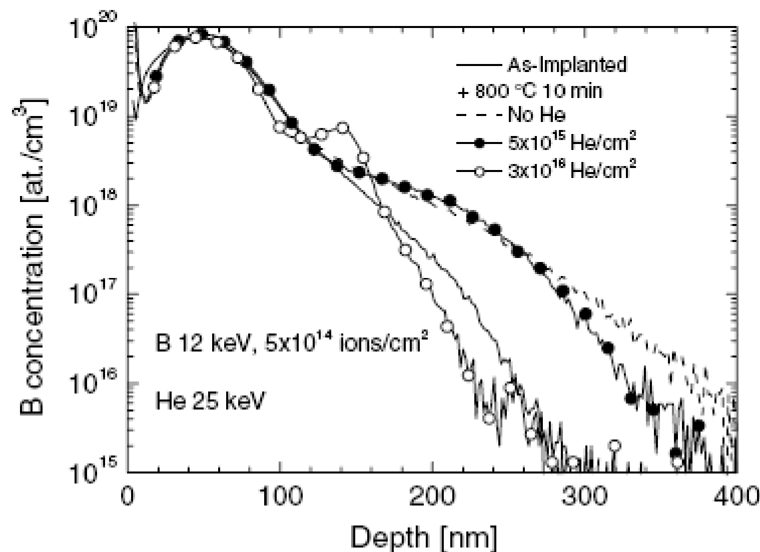

Figure 1.21: *Chemical B profiles after implantation (12 keV, 5 x 10^{14} ions/cm^2, continuous line) and after thermal annealing at 800 °C for 10 min in a He free sample (dashed line) and in samples implanted with He at 25 keV with fluencies of 5 x 10^{15} (line plus closed circles) and 3 x 10^{16} (line plus open circles) ions/cm^2. [Bruno07b]*

The reason is the local suppression of Is supersaturation, induced by B implant, due to the presence of the nanovoids which efficiently trap Is and lead to a peculiar B boxlike shape. This reduction occurs already at the first stages of annealing. The best optimization is

achieved if the nanovoids are sufficiently closed to the boron R_p, otherwise detrimental to device performances deep voids forms.
This method is promising to realize USJs junctions but it has again disadvantages as:

- the reduction of B diffusion is as stronger as lower is the temperature, while a higher B activation is achieved for higher temperature, so a compromise has to been reached;
- He induced cavities introduce deep levels in the Si-energy gap that act as recombination centers for carriers, leading to quite high leakage currents;
- if cavities overlap the B profile, B segregation occurs at their edges.

1.5.2 Pre-amorphization implant (PAI) method

Another efficient method to improve the B electrical activation and reduce B diffusion simultaneously is the dopant implantation in pre-amorphized Si, followed by re-crystallization of the Si substrate trough SPER (Section 1.4).

Amorphous silicon layers are usually achieved by implanting very high dose of heavy iso-electronic ions, such as silicon or germanium. Both primary and secondary recoil processes, caused by the incident ions, displaced the atoms of the silicon crystal from their lattice sites. The amount of displacement depending on the mass, dose and energy of the ions, while the thickness of the amorphous surface layer depends mainly on the beam energy. In order to strongly reduce the dynamic recombination of the point defects during the implantation itself, the amorphization implants can also be performed keeping the substrate at a low temperature (such as the temperature of the liquid nitrogen, 77 K).

Amorphous silicon (a-Si) maintains the tetrahedral coordination and consequently the short-range order typical of the crystalline Si (c-Si) but it has lost the long-range order, suppressed by the ideal crystalline angle distortions. a-Si differs from c-Si because it has a slower melt temperature [Olson] and a lower density [Custer]. Amorphous Si contains a lot of point defects as interstitials and vacancies, but also dangling bonds and floating bonds [Pantelides, van den Hoven, Urli, Roorda, Coffa, Bernstein06]. In a tetrahedral coordination, there are four sp^3 hybrid orbitals direct toward the central atom. A dangling bond (DB) exists when the fourth linear combination remains unbounded. A floating bond (FB) exists when the sp^3 hybrids are five toward the central atom; the fifth linear combination remains largely unbounded and has an energy level in the gap and, unlike DB, the wave function is not centered on the fifth bond, but it is distribuited over the five sp^3 hybrids. These defects

influence the crystal-amorphous transitions and the impurities diffusion in a-Si, similar at what happens in c-Si thanks to the point defects.

In the PAI method the crystal is pre-amorphizated by a Si or Ge implant of Si substrate; then dopants are implanted in the amorphous layer avoiding channeling effect [Rimini] and not introducing further damage of the crystal. Subsequently, the substrate is re-crystallized during anneal process by Solid Phase Epitaxial Regrowth (SPER) (extensively discussed in Section 1.4). After such process, very high concentration of electrically active dopants are achieved far above equilibrium [Solmi90]. However, PAI method is not exempt by undesired effects. During post-annealing treatments, TED and BICs formation were again observed experimentally. They are arisen by the interaction between dopant and defects originated after the SPER. These detrimental phenomena will be described deeply in the next Section.

1.5.3 Dopant diffusion and de-activation post SPER

After the amorphization implant, a layer of damage exists beyond the amorphous-crystal (a-c) interface. In fact not all the layer damaged by the implant accumulates enough damage to transit to the amorphous state, and a deep tail of the implant left a crystalline region supersaturated by interstitials. During the thermal annealing necessary to recrystallize the amorphous layer by SPER and electrically activate the dopant, these interstitials either diffuse away or precipitate beyond the original a-c interface into extended defects, called end of range defects (EOR). TEM measurements characterized these EOR defects [Claverie, Jones] and demonstrated that they are constituted by {311} defects and dislocation loops. Implantation in a-Si instead of in c-Si avoids the channeling tails and the superposition of dopant profiles with the damage layer. In this way, it could be possible to control them separately (as will be shown in Sections 1.6 and 1.7). As discussed in Section 1.3, the flux of Is from the EOR defects, however, can cause TED or BICs formation post-SPER annealings.

A lot of studies were made about the effect of post-annealing processes on Si samples that were pre-amorphized, B implanted and regrown by SPER at 550 °C or 650 °C, subsequently [Jin, Cristiano]. After annealings at temperatures higher than 750 °C, some B atoms lose their substitutional positions, deactivating electrically the junction. The maximum of this degeneration is achieved at 850 °C, while at higher temperature electrical re-activation occurs (Fig. 1.22).

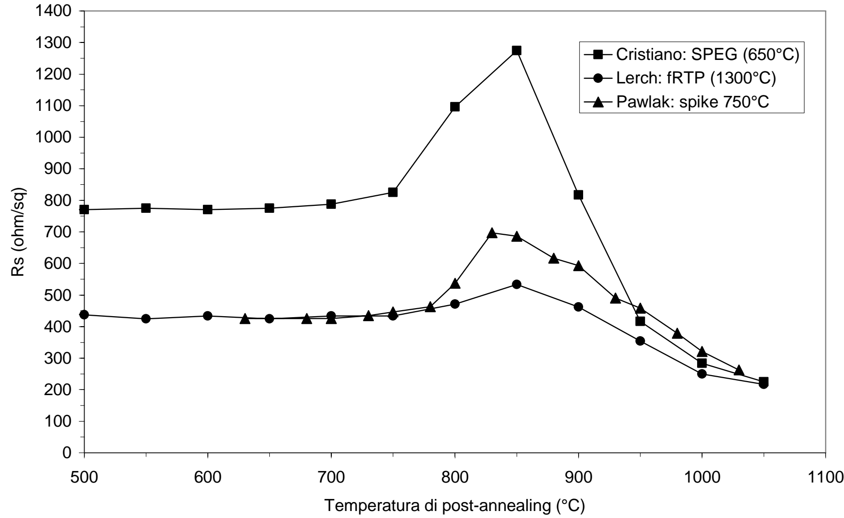

Figure 1.22: *Post-annealing temperature dependence of sheet resistance: values of 10^{15}at/cm^2 B implant in a-Si are reported. Cristiano: implant energy 0.5 keV, annealing at 650 °C for 5 s and post-annealing for 30 s [Cristiano]; Lerch: same Cristiano's conditions but activation by fRTP at 1300 °C [Lerch]; Pawlak: implant energy 1.5 keV and activated by spike annealing at 750 °C [Pawlak05].*

The origin of the electrical deactivation of B was attribuited by TEM analyses to the evolution of EOR [Pawlak04, Cristiano]. The concentration of EOR decreases releasing interstitials towards the sample surface during annealings at temperatures higher than 750 °C, until they reach an equilibrium configuration at 850 °C in which {311} defects have dissolved or evolved in dislocation loops, that are more stable defects. At this temperature the supersaturation of interstitials decays near to equilibrium values and the deactivation stops. At temperature higher than 850 °C the BICs clusters dissolve by emitting B interstitials and therefore increasing B electrical activation. Electrical deactivation and reactivation are thermally activated processes but reactivation has a higher activation energy.

1.6 PAI WITH C

Since the rensponsible for B TED and BICs formation is the excess of self-interstitials of the EOR defects, B electrical deactivation can be reduced by trapping or annihilating self-interstitials. An efficient method for trapping Is is to introduce C or F between B implant and the EOR region.

It was demonstrated experimentally [Mirabella02] that each self-interstitial deactivates two substitutional C atoms, C_S, as according the reaction:

$$I + 2C_S \rightarrow 2C_{cl} \qquad (1.28)$$

where the immobile clustered carbon C_{cl} was found to be non longer active as an interstitial trap and it does not release Is. An explanation was given assuming that substitutional C appears to be a trap for Is through the following reactions:

$I + C_S \rightarrow C_I$ (mobile) (1.29)

$C_S + C_I \rightarrow C_S C_I$ (immobile). (1.30)

The C diffusion is mediated by Is (Fig. 1.6) through the kick-out mechanism [Eq. (1.12)], creating a mobile interstitials C (C_I). The mobile C_I does not undergo an out-diffusion, but pairs with another substitutional C_S stopping his motion and forming an immobile couple $C_S C_I$.

The B TED was studied when no supersaturation of self-interstitials due to implantation is present [Rucker, Scholz] either when there is [Stolk95, Stolk97]. A C-rich layer between B implant and the a-c interface can be interposed by molecular beam epitaxy (MBE) growth [Napolitani01] (Fig. 1.23). In this way, C-rich layer acts as a membrane for capturing of self-interstitials.

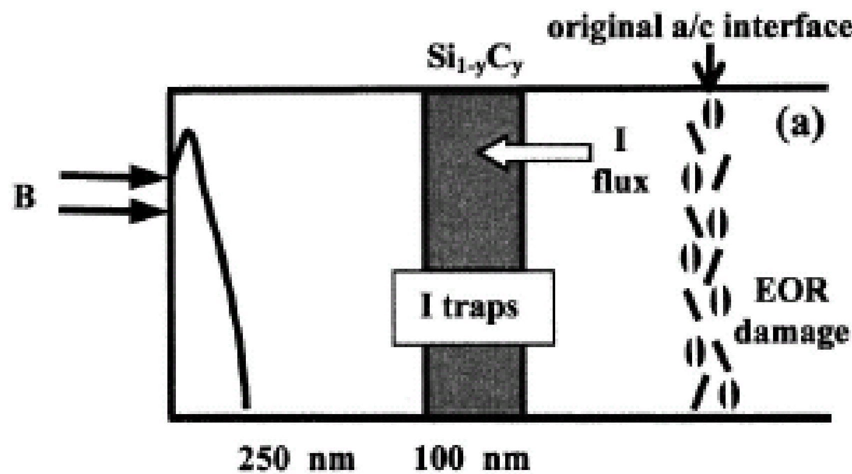

Figure 1.23: *Schematic of the sample used in [Napolitani01].*

C can be introduced also by ion implantation, simplifying the junction creation process [Moroz, Di Marino, Edelman] (Fig. 1.24).

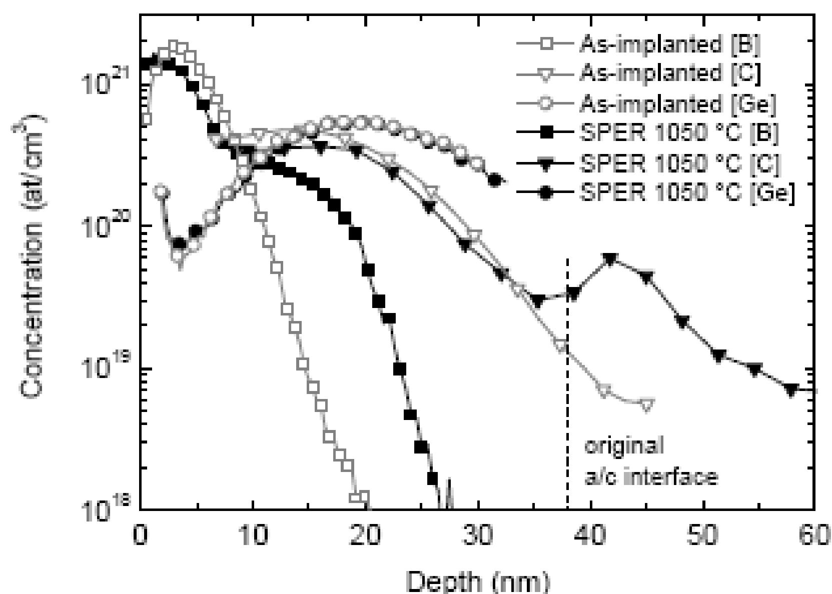

Figure 1.24: *B, C and Ge profiles measured by SIMS before (grey empty symbols) and after regrowth obtained by spike RTA at 1050 °C (black full symbols). Ge was used to amorphize the original crystalline substrate. The original position of a-c interface is also shown [DiMarino].*

Unfortunately, the C clusters are strongly stable, so the substrate remains full of defects that could destabilize the junction causing a current of leakage.

1.7 PAI WITH F

Similarly to C co-implantation, also implanting F can be an useful method to reduce and avoid TED and BIC phenomena processes in USJs created by PAI method and implanted with B [Jin, Cowern05].

Since 1982, p-type junctions were realized by BF_2^+ implantation instead of simple B^+ implant [Fuse]. The ion implantation of BF_2^+ needs higher energy than B^+ to form the same B range distribution; it is well known that low energy ion beams are less stable and give lower current density than high energy ion beams. Moreover, being BF_2^+ molecule heavier than the B^+ ion, the channeling problem is reduced because the crystal is more easily damaged reaching amorphization at lower doses. In presence of F, sheet resistance is reduced [Tsai, Shauly] improving the B electrical activation. In BF_2^+ implanted PAI Si samples, the B TED is more reduced than when B is implanted alone [Wilson].

The effect of F on B TED in PAI Si is studied extensively since more than ten years ago. In the first work [Downey] the authors affirmed that F reduces B TED influencing Is

diffusion after their release from the EOR region or Is ability to kick out B atoms. A rate equations model based on F-I complexes was proposed to explain the F diffusion and the reduction of B TED [Park99]. Mokhberi *et al.* [Mokhberi] found that more F is retained in the bulk after the anneal in presence of B but the same does not occur when As is present instead of B. So, they attributed the F reduction effect on B diffusion to a F-B chemical interaction, excluding any F-I interaction. The chemical reaction between B and F was finally rejected by Impellizzeri *et al.* [Impellizzeri04, Impellizzeri05]. In their work [Impellizzeri04], sample grown by molecular beam epitaxy (MBE) with a B delta layer were amorphized and implanted with different doses of F at the energy of 100 keV (Fig. 1.25).

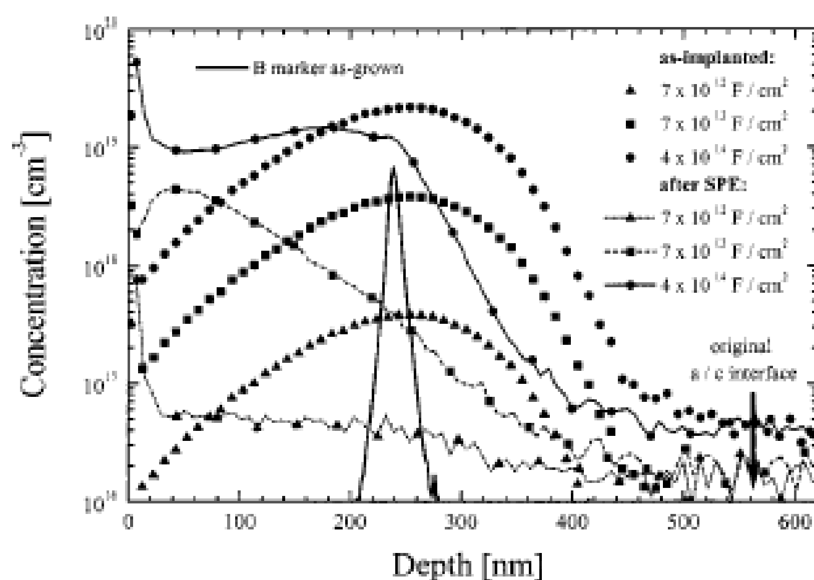

Figure 1.25: *F profiles as-implanted (symbols) and after solid phase epitaxial regrowth (SPER) (lines plus symbols) for three different F doses, and B spike profile in the as-grown sample [Impellizzeri04].*

During the annealing to induce SPER F redistributes and out-diffuses and the effect is more pronounced in samples implanted with a lower dose. In addition, B TED diminishes by increasing the F dose (Fig. 1.26).

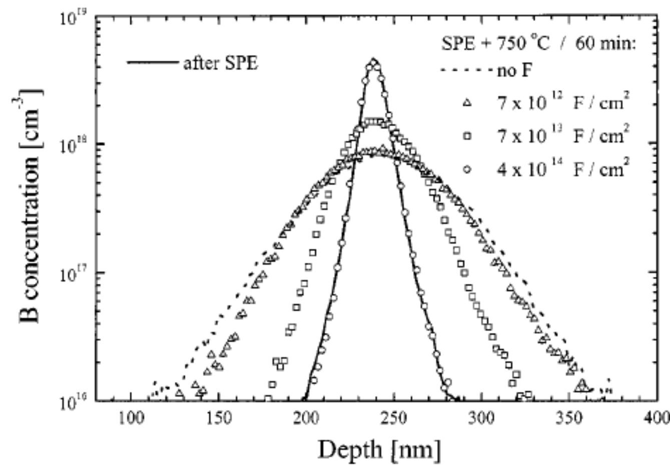

Figure 1.26: *B diffused profiles for three different doses of F implantation after SPER plus thermal anneals (open symbols) at 750 °C / 60 min. B profile for a similar sample without F is also shown for reference (dashed line) [Impellizzeri04].*

During the post-SPER annealing a F diffusion toward the surface and the bulk occurs with a subsequent accumulation in the region of the EOR defects, as shown in Fig. 1.27 for the medium and high implant doses.

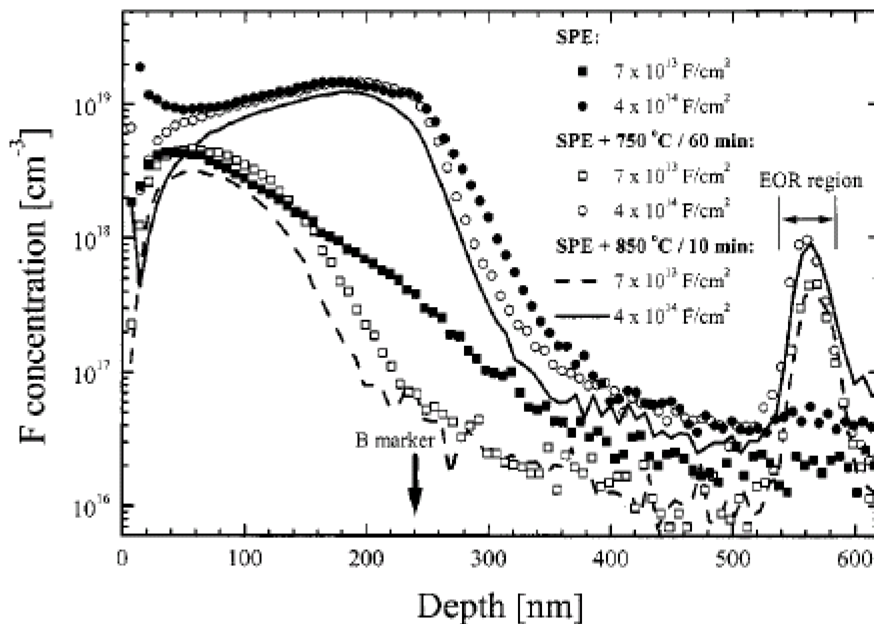

Figure 1.27: *F profiles after SPER (closed symbols), SPER plus thermal annealing at 750 °C / 60 min (open symbols) or 850 °C / min (lines) for the two highest F implanted doses [Impellizzeri04].*

At the B delta depth, the F concentration for the medium implant dose is about two orders of magnitude lower than B one after SPER at 750 °C for 60 minutes, even if a consistent B TED reduction is observed (Fig. 1.26). Moreover, the F diffusion profiles after both anneals are not

affected by the presence of B: as a matter of fact, there is not any evidence for F accumulation at the B depth. These two facts refute the possible existence of any interaction between B and F, but they support the F effect on the Is release by EOR defects. F could reach EOR damage and stabilize these defects or intercept the Is flux towards the sample surface. It was subsequently performed an experiment to distinguish if F stabilizes EOR defects or traps mobile Is [Impellizzeri05]. A multi-delta array was grown in Si by MBE. Then the substrate was amorphized and F co-implanted in such a way to amorphize the first 4 deltas and leave the others in c-Si beyond the EOR damage region (Fig. 1.28). B TED was suppressed for delta covered by F implants, while a B diffusion occurred in the other deltas, quantitatively similar to the diffusion observed in a reference sample without F. In conclusion, F does not prevent the Is emission from EOR damage but reduces the Is supersaturation intercepting their flux towards the sample surface.

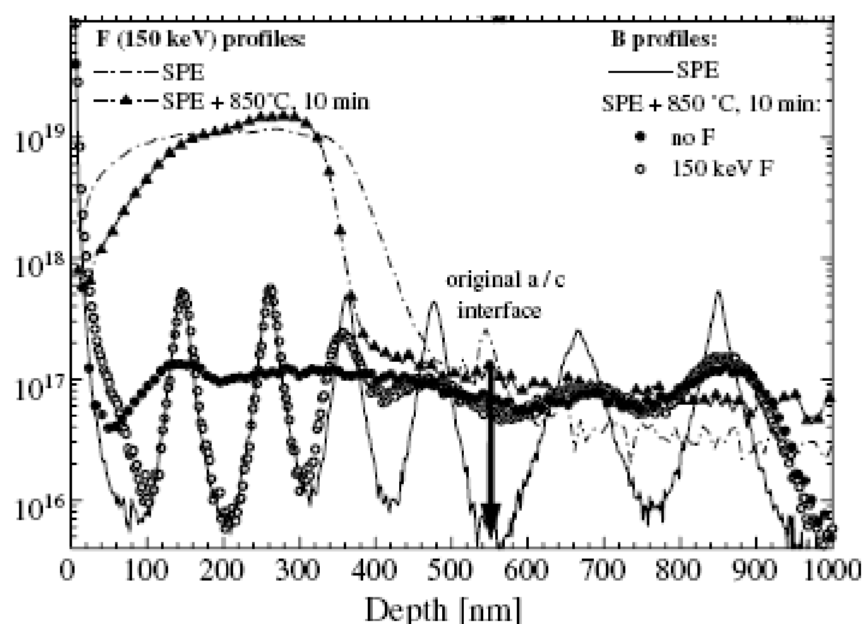

Figure 1.28: *B profiles after SPER (continuous line) and after the 850 °C thermal anneal for the sample with (open circles) and without F (closed circles) implanted at 150 keV. F profiles after SPER (dotted line) and after the 850 °C thermal anneal (closed triangles) [Impellizzeri05].*

1.7.1 F as a trap for Is: F-V clusters

The F trapping effect on Is could be due to the creation of highly mobile F-I clusters that outdiffuse from the sample or to the formation of F induced Vs [El Mubarek03, El Mubarek04, Kham05, Kham07, Impellizzeri06, Impellizzeri06b].

Recently, transmission electron microscopy (TEM) and positron annihilation spectroscopy (PAS) analyses supported this last interpretation. In particular, the defects formed during annealing in PAI Si implanted with BF_2^+ were studied and classified considering their nature, distribution and evolution during post-annealing by TEM measurements [Sands, Wu]. Mainly F bubbles were observed near the original a-c interface, the projected range of BF_2^+ implant and at the surface [Nieh]. The effects of point defect injection on the formation of F bubbles were also investigated by TEM analysis [Chu], while the formation and evolution of F bubbles were characterized recently after SPER regrown at 700 °C followed by an annealing at 740 °C for 15 minutes [Boninelli06]. These bubbles are indeed called nano-bubbles, as they are small with an average diameter of (3.7 ± 1.0) nm (Fig. 1.29). They are cavities enriched with F and the concentration of Vs inside the bubbles was estimated to be about 2 x 10^{14} Vs/cm^2.

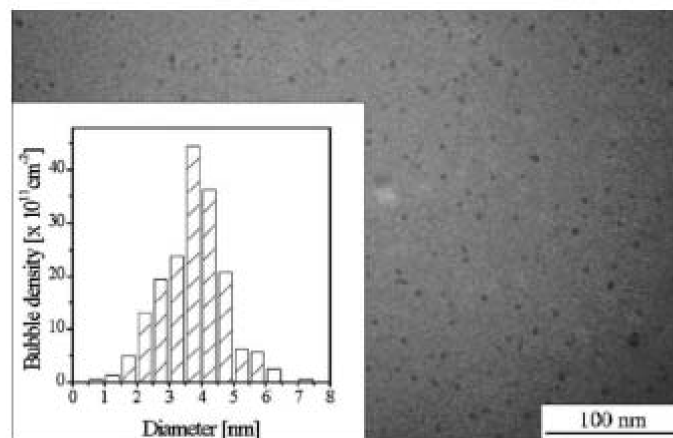

Figure 1.29: *Plan view (TEM) images of samples implanted with F, after SPER at 700 °C, followed by a thermal annealing at 740 °C for 15 minites. In the inset, the histograms of the size distribution of bubbles are reported [Boninelli06].*

The above value could be an underestimate due to bubbles contraction during sample preparation and to TEM resolution limit (bubbles with radius smaller than 0.5 nm are not detectable by TEM). The nano-bubbles are formed already in the amorphous side of partially regrown samples might as the result of the diffusion and coalescence of complexes constituted by F atoms and dangling bonds in the amorphous bulk. These nano-bubbles are then incorporated directly into the c-Si during the passage of the a-c interface. TEM measurements of a sample partially regrown for 25 s at 700 °C revealed that a band of bubbles is located around the maximum of the F concentration profile, clearly suggesting that F atoms are involved in the mechanism of bubbles formation (Fig. 1.30) [Boninelli08].

During post-SPER annealing they partially dissolve and transform from spherical- to cylinder- shaped bubbles [Boninelli08]. Indeed in c-Si, while F partially evaporates from the surface, the total volume occupied by bubbles proportionally reduces. Hence F also stabilized the bubbles by its presence, as, once F evaporates, the bands are rearranged and the bubble volume proportionally decreases.

Other experimental evidences of the coexistence of F with vacancies aggregates were given by PAS studies that identified F-V complexes in c-Si [Pi, Simpson] and in SiGe [Abdulmalik].

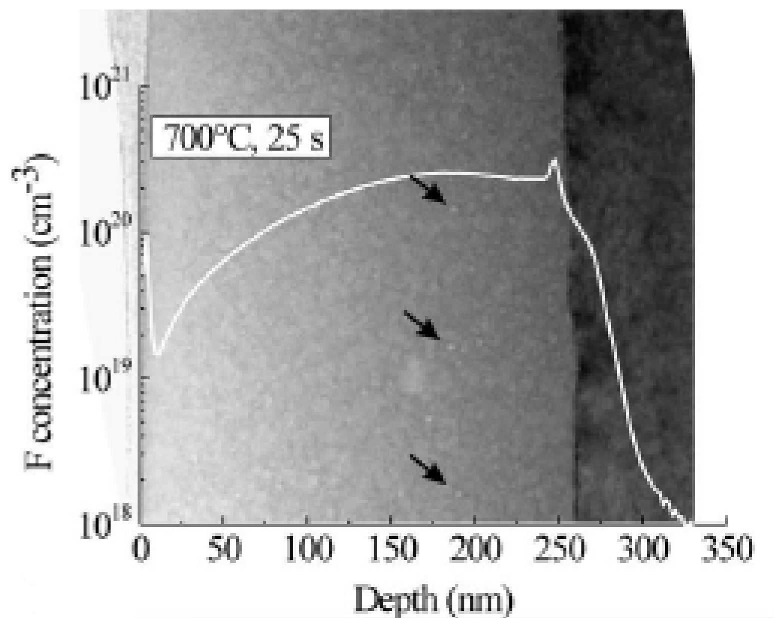

Figure 1.30: *SIMS F concentration profile overlapped with TEM cross-sectional view of samples implanted with F and partially regrown by SPER at 700 °C for 25 s. The arrows point to some bubbles. [Boninelli08]*

In addition several ab-initio calculations support the idea of the existence of F-V complexes [Diebel04, Lopez05, Fiorentini, Diebel06, Lopez06]. Calculations showed how F-B or F-I bond energy is lower than B_S-I one, so these bonds have not been considered anymore. A lot of calculations were done about the more stable F_nV_m complexes, constituted by n F atoms and m Vs. The complex F_1V is created when a substitutional F in c-Si moves towards one of the first neighbor forming a covalent bond of length 1.68 Å. Saturating the other dangling bonds, a F_4V complex is constituted. This process induces a distortion to the matrix: the sum of F-Si bond length and F covalent radius is 2.40 Å and it is greater than the Si-Si interatomic distance (2.35 Å), so it is not possible to introduce more than one F-Si bond along the direction of V-Si without inducing stress to the lattice. Then this is the reason why the minimum energy state is achieved by moving F-Si bonds from the ideal direction relaxing

at a configuration [Fig. 1.31(a)] of lower energy, 2.0 eV less, than the non-relaxed one [Fig. 1.31(b)] .

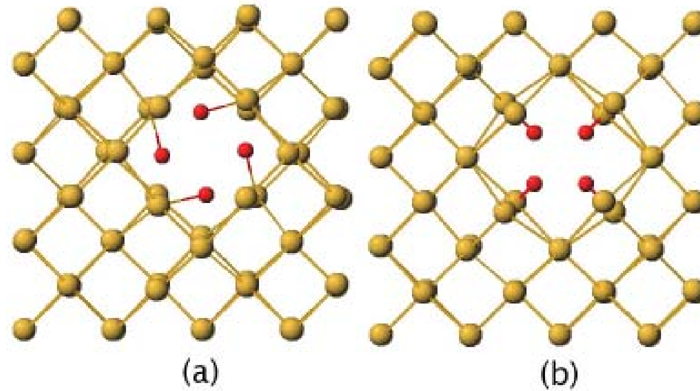

Figure 1.31: *View along <100> direction of (a) F_4V relaxed complex and (b) F_4V non-relaxed one [Fiorentini].*

Besides FV complex, the most stable configurations are those with all dangling bonds saturated following the stechiometry n = 2m + 2 (F_4V, F_6V_2, F_8V_3, $F_{10}V_4$, …). Basing on the F_nV_m formation energies, the F_nV_m concentration as a function of F concentration was calculated (Fig. 1.32): at high F concentrations, large complexes are more probable.

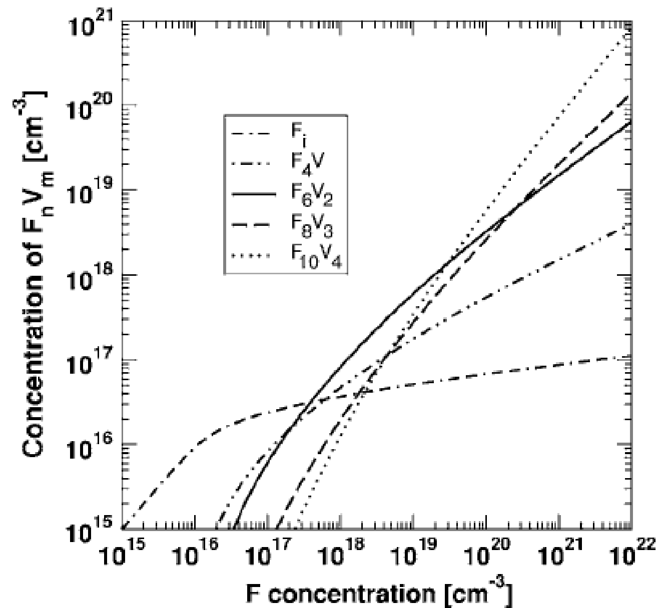

Figure 1.32: *F_nV_m concentrations in function with F incorporated at SPER temperature of 800 °C, according to calculations of [Lopez06].*

However, this theoretical approach is only an approximation because it does not consider any possible energetic barriers and do not consider the actual process of introducing of F in c-Si, that includes PAI and SPER.

1.7.2 F effect on the SPER rate

As shown in Section 1.4, non doping impurities, including F, reduce the SPER rate but the mechanism responsible for this effect has not been explained yet.

Suni *et al.* [Suni84], studying the SPER rate in presence of halogen impurities, noted that a segregation peak of these elements appears at the a-c interface during SPER. So, they suggested that the retardation effect can be attributed to this anomalous peak. The first systematic work about the F effect on the SPER rate was realized by Olson and Roth [Olson]. They studied the SPER rate as a function of temperature for F implanted a-Si in the temperature range from 520 °C to ~ 1000 °C (Fig. 1.33).

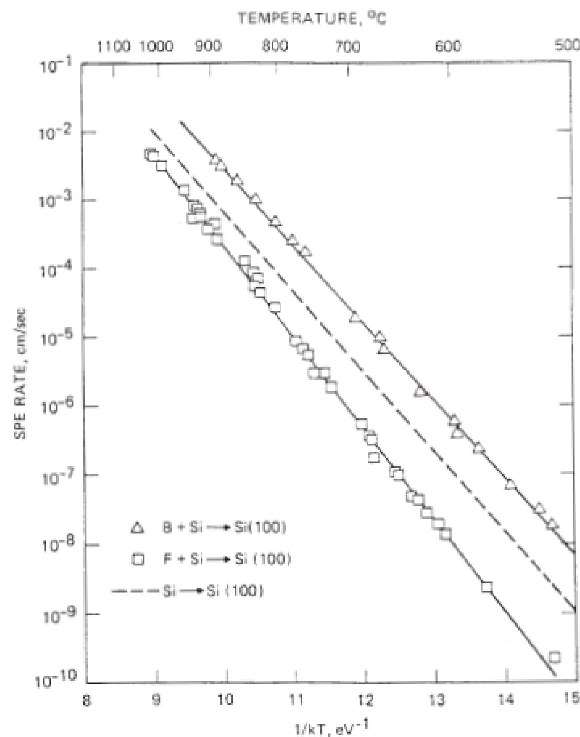

Figure 1.33: *Temperature dependence of the SPER rate in F and B implanted a-Si. Intrinsic rate is given by dashed line for comparison. The implantation energies and fluencies are 18 keV and 6 x 10^{15} ions/cm^2 for F, 10 keV and 3 x 10^{15} ions/cm^2 for B, with peak concentration of 1 x 10^{21} at/cm^3 and 5 x 10^{20} at/cm^3 respectively [Olson].*

In comparison to intrinsic rate (dashed line in Fig. 1.33), the activation energy for F implanted substrate is higher (3.06 eV). This high activation energy is the consequence of the F retardation effect, even if no microscopic description of its causes was presented in literature.

A microscopic interpretation of the F role during the recrystallization was given by Park [Park96]. After bond breaking at the a-c interface, necessary to induce the epitaxial

regrowth, the broken dangling bonds migrate along the interface. The rearrangement of the random network can be considered as the result of dangling bonds migration. Impurities, as F, could immobilize the broken bonds inhibiting the rearrangement and, thereby, preventing the motion of the ledges and retarding the SPER rate. In the more comprehensive and recent SPER model [Rudawski08, Rudawski08b], the slowdown of SPER was attributed to the additional time needed to incorporate inactive impurities that tend to cause local lattice distorsions if non substitutionally incorporated, as the case of F, but a clear relation that describes this phenomenon is not discovered yet.

It is correct to report here for completeness that, recently, it was discovered that F dopes Si [Impellizzeri07] but not a level high enough to influence the regrowth rate. So, F can be again considered as non dopant impurity for the SPER point of view.

1.7.3 F segregation at the a-c interface

An evidence of the F accumulation at the moving a-c interface is reported in Fig. 1.34.

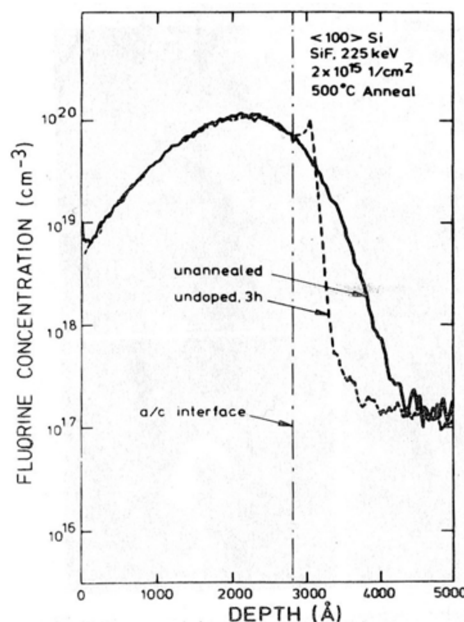

Figure 1.34: *SIMS depth profiles of F in Si <100> wafers amorphized with Si^+ irradiation and subsequently implanted with a dose of 2 x 10^{15} (SiF^+)/cm2 and annealed at 500 °C [Suni84].*

The segregation of impurities in Si has been usually described by a first order kinetic model [Ho] yielding for the total interface transport flux $f = h(C_1\text{-}C_2\ m)$, with h the transport coefficient, C_1 and C_2 the impurity concentrations at the two sides of the interface that separates the two phases and $m = C_1^*/C_2^*$ the equilibrium segregation coefficient, i.e. the ratio of the equilibrium solid solubility in the two phases (C*) estimated at the equilibrium

condition. Another way to study these systems is to consider the classic solute redistribution during solidification [Smith55], in which the concentration of solid (C_S) is proportional to the concentration of solute (C_L) according to $C_S = k * C_L$, where k is called segregation coefficient and, in general, is less than 1.

Unfortunately, the F segregation at the a-c interface is different with respect to the above model because the segregation coefficient changes with depth, as Mirabella *et al.* [Mirabella05] determined some years ago. They characterized first the F segregation phenomenon characterising partial and complete regrowths at 580 °C of PAI Si samples, previously implanted with 4 x 10^{14} F/cm^2 at 100 keV [Fig. 1.35(a)].

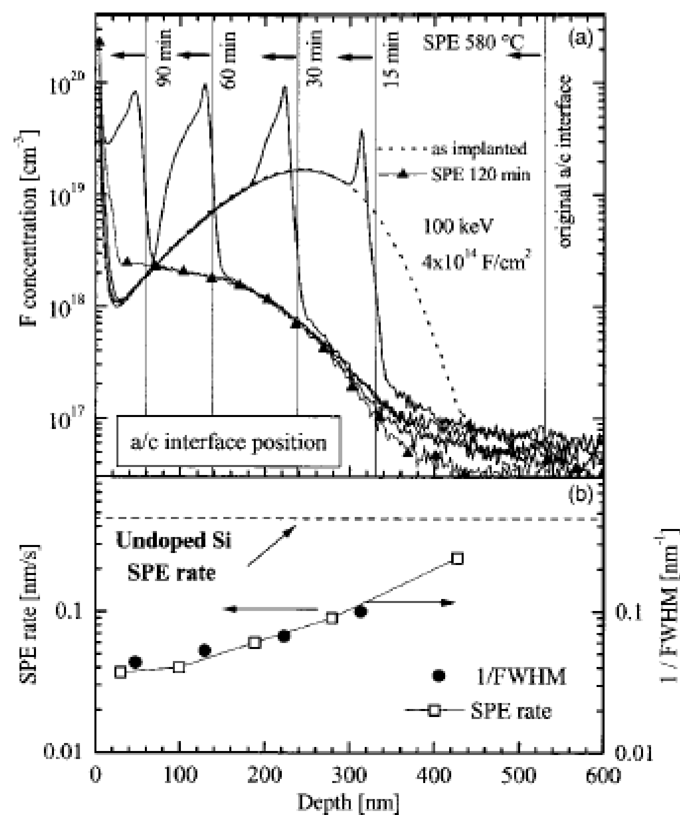

Figure 1.35: **(a)** *SIMS profiles of F incorporation after implantation (dotted line,100 keV, 4 x 10^{14} at/cm^2), during (continuous lines) and after (triangles) SPER at 580 °C. The a–c interface positions during SPE, as determined by channeling measurements, are also indicated by vertical lines.* **(b)** *Averaged SPER rate (squares, left-hand vertical axis) and reciprocal of F peak FWHM (circles, right-hand vertical axis) versus depth. The undoped Si SPER rate at 580 °C[Olson] is reported too (horizontal dashed line) [Mirabella05].*

In Fig. 1.35(a) the F profiles snapshots after partial and complete SPER are reported together with the a-c interface positions reported as vertical lines. F is pushed toward the surface by the a-c moving interface. The F peak is clearly located at the amorphous side of the a-c interface and disappears, once SPER is completed, evaporating from the surface. The segregation coefficient k, defined in the paper as the concentration in the crystal over the one

in the amorphous at the interface depth varies from 0.005 to 0.03 because, although the concentration in the amorphous is quite constant, the one in crystal keeps on increasing also more than one order of magnitude. The k variability could mean that the system is not in steady-state conditions.

A way to describe this kind of system is to consider the interface layer as a third region as well as the amorphous bulk and the crystal one. This "three phase system" approach was introduced and used in past by some authors to study P segregation and redistribution at the Silicon-Silicon Dioxide interface [Lau, Orlowski] or As out-diffusion from poly-silicon into monosilicon [Orlowski]. This method regards directly the dynamics of the system considering the exchanges between each bulk phases and the interface layer of finite thickness. This approach will be used in our work.

1.7.4 F diffusion in a-Si

Very little is known about F diffusion in c-Si and in a-Si. A theoretical calculation suggests that F atom may diffuse as F^- through interstitials channels in c-Si [van der Walle]. In fact, it was discovered experimentally that F diffusion in c-Si is anomalous because F atoms migrate preferentially towards the surface of Si, and the diffusion of F into bulk silicon is completely suppressed. This happens only for F and not for other impurities [Jeng]. This outdiffusion causes a depletion of the as-implanted F profile, as it is possible to observe in Fig. 1.33. Moreover, the F redistribution does not occur below (or equal to) 500 °C, and the F migration starts at a temperature of ~ 550 °C, suggesting a strongly temperatures dependent thermally activated process. Studying the F-enhanced B diffusion in a-Si, Jacques *et al.* [Jacques] suggested that dangling bonds in a-Si would preferentially bond with F.

In Fig. 1.35(b), the SPER rate and the reciprocal of the full-width at half-maximum (FWHM) of the F segregation peaks were plotted. According to the classic segregation theory [Pfann], the impurity diffusivity in the amorphous phase is equal to the ratio between the SPER rate and the FWHM. So, F diffusivity, estimated in [Mirabella05], is constant and equal to $(0.9 \pm 0.1) \times 10^{14}$ cm^2/s at 580 °C.

However, the first determination of F diffusivity in a-Si was made by Nash *et al.* [Nash]. In their work, F was implanted at room temperature at an energy of 30 keV and a dose of 5×10^{15} at/cm^2 in a-Si previously deposited on Si wafers at 560 °C using a conventional

low-pressure chemical-vapor deposition (LPCVD) furnace. The samples were annealed for 30 s in the range 600 – 700 °C (Fig. 1.36).

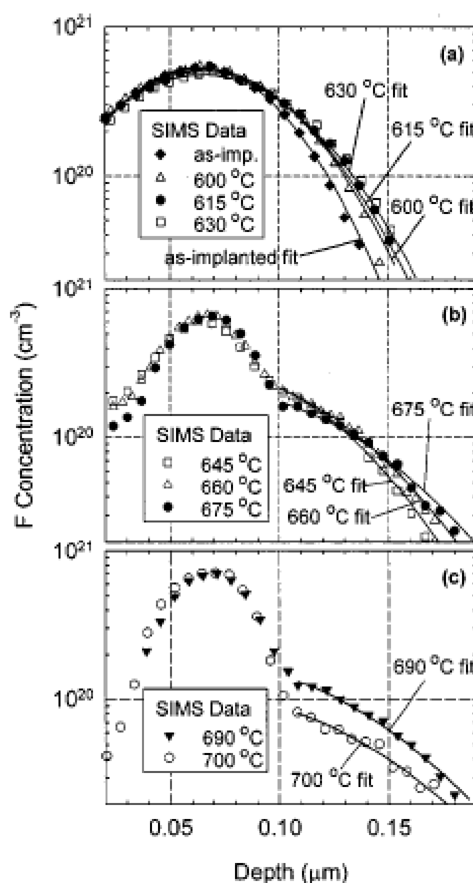

Figure 1.35: *F SIMS profiles for a-Si samples implanted with 5 x 10^{15} at/cm^2 F^+* **(a)** *as implanted and annealed for 30 s at 600 – 630 °C,* **(b)** *annealed for 30 s at 645–675 °C, and* **(c)** *annealed for 30 s at 690 and 700 °C. Solid lines are Gaussian fits to the SIMS data [Nash].*

Each F profile after annealing showed a Gaussian diffusive tail and the diffusion coefficient was extracted by simulations of these tails (solid lines) as a fitting parameter at each temperature. Figure 1.37 shows the Arrhenius plot of the extracted diffusion coefficient. Nash *et al.* found an activation energy of (2.2 ± 0.4) eV and a pre-factor of ~ 0.1 cm^2/s, considering an uncertainity of ± 20 °C in the absolute process temperature. So, F diffusivity estimated in [Mirabella05] agrees well the determination made by Nash *et al.*.

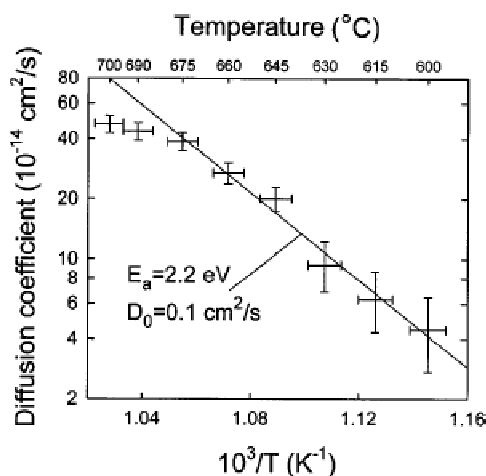

Figure 1.37: *Arrhenius plot of the diffusion coefficients obtained from fitting the Gaussian profile to the experimental data [Nash].*

1.7.5 F incorporation in c-Si

Nash *et al.* [Nash] also noticed that a trapping of implanted F in a-Si occurs around the implant peak [Fig. 1.36(b) and (c)], increasing with temperature. They suggested that some F is trapped at the damage associated with ion implantation. After the results obtained by Boninelli *et al.* [Boninelli06, Boninelli08], this effect is recognized to be the result of F clustering in a-Si nano-bubbles (Sect. 1.7.1).

It is not known how F is redistributed and organized into these nano-bubbles. Kumeda *et al.* [Kumeda] investigated the F incorporation scheme in fluorinated a-Si (a-Si:F) by nuclear magnetic resonance (NMR) and infrared measurements. The observed NMR signals of F can be simulated by superimposing signals from dispersed F atoms, clustered ones, SiF_3 species and SiF_4 molecules. They also noted that the presence of SiF_4 increases with temperature.

The F incorporation is the result of the F redistribution during Si SPER. F redistribution is governed by several processes involving F, i.e.: the F push-forward movement induced by the a-c interface, F diffusion in a-Si and F induced nano-bubbles creation and, obviously, the SPER that is influenced by F [Fig. 1.35(a)].

All these phenomena are thermally activated. So, F profiles can be modulated by changing SPER temperature. In Fig. 1.38 samples enriched with 4 x 10^{14} F/cm^2 at 100 keV were recrystallized at three different temperatures: at 580 °C for 120 min, 700 °C for 80 s and 800 °C for 3 s [Impellizzeri06c]. It is clear that the F incorporated amount increases with the SPER temperature, going from 15% to 90% of the implanted one.

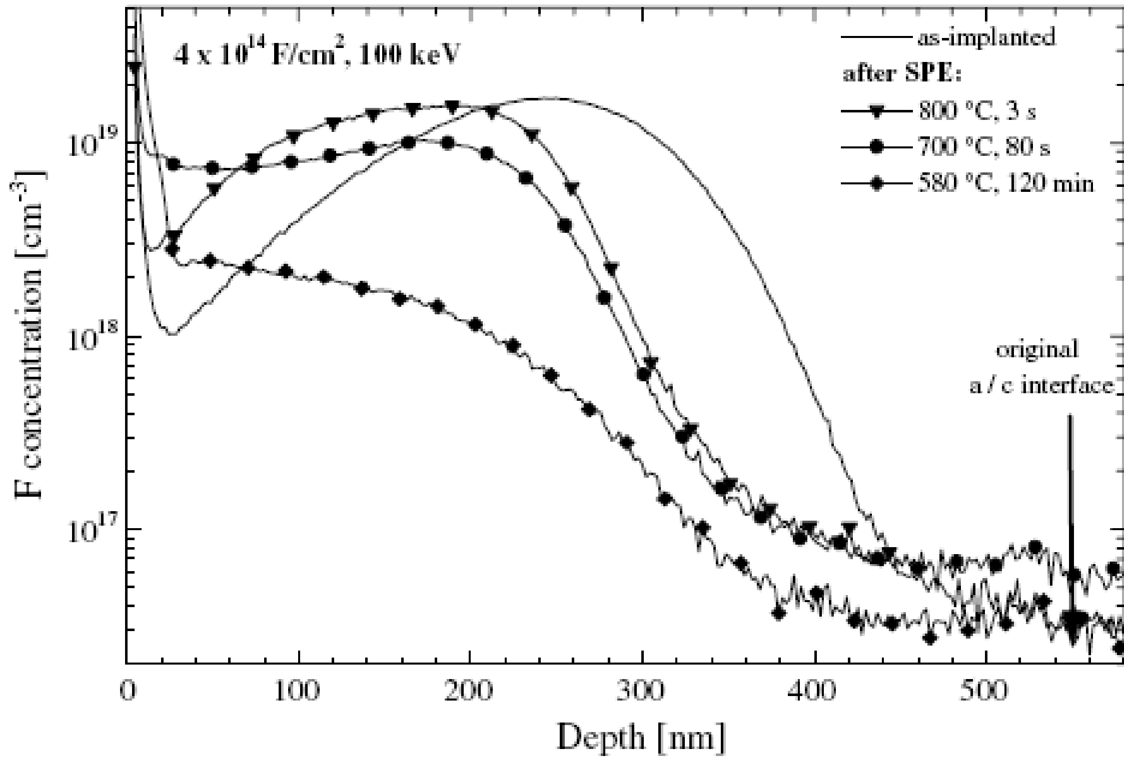

Figure 1.38: *F concentration profiles in the as-implanted sample (line; 100 keV, 4 x 10^{14} at/cm^2) and after SPER at different temperatures: 580 °C for 120 min (diamonds), 700 °C for 80 s (circles), 800 °C for 3 s (down triangles) [Impellizzeri06c].*

Despite the above investigation, the different pieces of the puzzle governing the microscopic mechanism of the F redistribution and incorporation in c-Si are not yet complete and merged in a predictive model. Recently, some authors tried to model and simulate the data presented in literature.

Zhang *et al.* [Zhang] described the F redistribution by ab initio calculation considering F-V, F-I and F-B interactions and using classical segregation theory (Fig. 1.39). From Fig. 1.39, it is evident how the F diffusion is not reproduced correctly and the F concentration at a-c interface and F incorporation profile are overestimated.

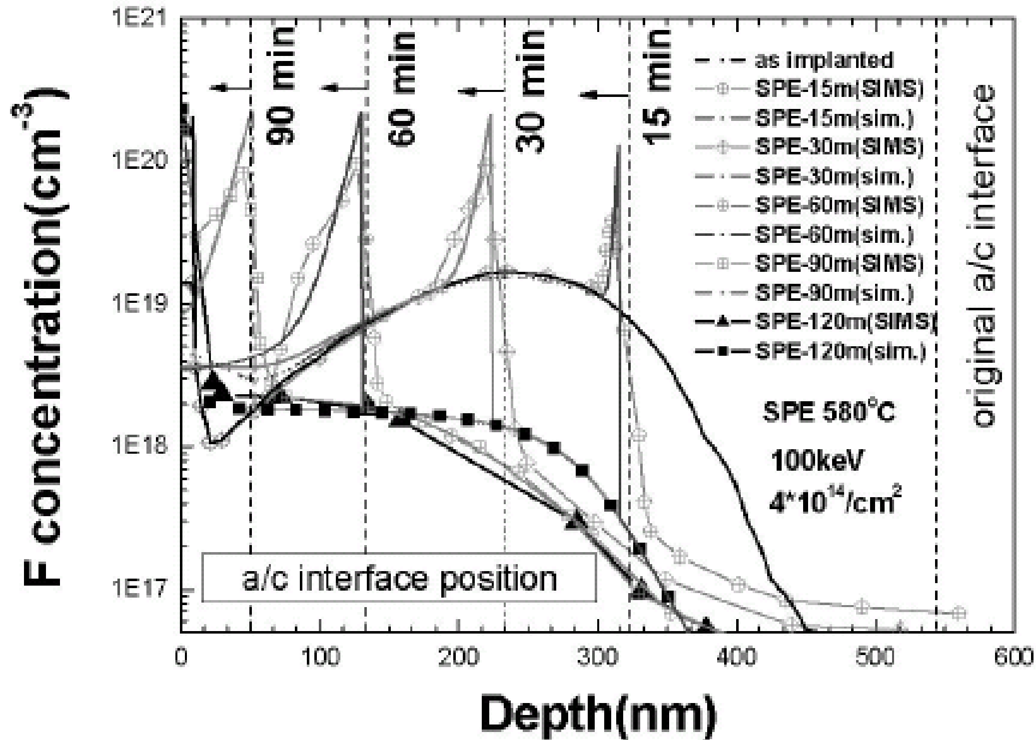

Figure 1.39: *SIMS profiles presented by Mirabella et al. [Mirabella05, also reported in Fig. 1.30(a)] and simulation results of F incorporation after implantation, during and after SPER at 580 °C. The a-c interface positions during SPER are indicated by vertical dash lines [Zhang].*

Instead, Zographos *et al.* [Zographos] modelled the F complete redistribution after complete SPER describing F slow down of the SPER rate by impurity effect on SPER [Olson] and considering a competion between regrowth and F diffusion in a-Si, and a temperature dependent probability for F to be incorporated (~ 1% at 580 °C, ~ 20% at 800 °C) during recrystallization. Their results are reported in Fig. 1.40. Zographos *et al.* did not show any simulation of the F partial regrown profiles, but only complete regrown ones. The simulations are optimized on a single starting F profile (4 x 10^{14} at/cm^3 at 100 keV). The change in temperature of the incorporation probability allows to reproduce quite correctly the incorporation at different temperatures. During the work of this thesis we implemented a similar approach and demonstrated how it is not able to reproduce the profile starting from different concentration of F in the as-implanted amorphous layer. This strong limit will be overcome by our work.

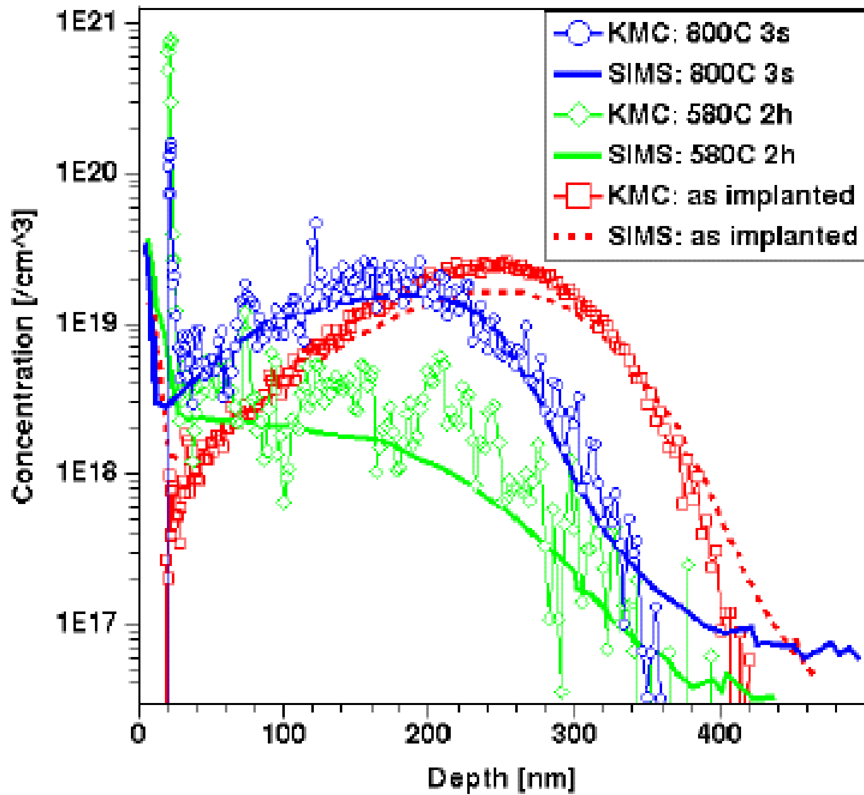

Figure 1.40: *F concentration profiles of the as-implanted sample (SIMS data from [Impellizzeri06]) and after SPER at different temperatures: 580 °C for 120 minutes and 800 °C for 3 s [Zographos].*

In this thesis a broad experimental investigation on the chemical profile redistribution of F will be reported. A new model able to predict the evolution of F chemical profile and states (i.e., clustered, diffusing, segregated) during SPER starting from the as-implanted profile will be proposed. The model will combine together the F diffusion and F clustering in a-Si, the F retardation effect on the SPER rate and the F incorporation in c-Si. This model with its physical understanding should increase and improve the knowledge and the use of F as a tool for optimizing the doping profile in the fabrication of USJs. This kind of experimental approach and modellization could be used in similar systems, in which the redistribution of impurities occurs during phase transition.

Chapter 2

EXPERIMENTAL

As described previously, the aim of this work is to characterize and model the evolution of the F chemical profile implanted in pre-amorphized silicon during SPER. To do this, it was necessary to join an intense and accurate experimental analysis with a precise and reliable simulation code based on a complete rate equations system. In this Chapter the samples realization and the techniques used for experimental analyses will be presented in details.

2.1 EXPERIMENTAL METHODOLOGY

First of all, the design of the samples used in this work considered different Si and F implants and annealing temperatures to study this system in wide ranges of amorphization depths, F concentrations and SPER temperatures.

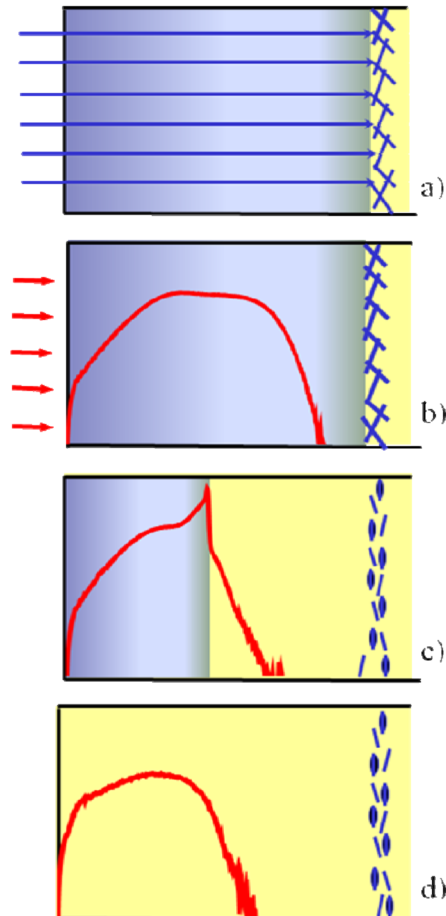

Figure 2.1: *Schematic description of our experimental approach:* **(a)** *pre-amorphization process by Si^- implants (a-Si is represented by blue area, while c-Si by yellow one; EOR defects are also shown),* **(b)** *F implantation in a-Si (red profile),* **(c)** *partial SPER and F redistribution, and* **(d)** *complete SPER.*

In Fig. 2.1 a schematic description of our experimental approach is shown. Initially c-Si samples were pre-amorphized by implanting Si^- ions [Fig. 2.1(a)] and then PAI Si samples were implanted with different F implants [Fig.2.1(b)]. Subsequently these samples were annealed in order to partially [Fig.2.1(c)] or completely regrow [Fig.2.1(d)] the amorphous layer.

The F concentration profiles were investigated by performing Secondary Ions Mass Spectrometry (SIMS) measurements. X-ray absorption spectroscopy (XAS) analyses were

made to provide element specific structural information on the F incorporated in c-Si. Finally, high resolution X-ray diffraction analyses were done in two samples in order to characterize the strain profile.

A brief description of the ion implantation, thermal processes, and the characteristics of techniques will be provided in the next Sections.

2.2 SAMPLE PREPARATION

Two sets of samples were produced: the first one for the study of F redistribution during SPER (see Table 2.1), the second one for the investigation by XAS of the chemical surrounding of F in PAI with and without the co-presence of B atoms (see Table 2.2).

Sample	low conc. A	low conc. B	Medium conc.	high conc. A	high conc. B
Si PAI					
3e15 at/cm^2 250 keV + 2e15 at/cm^2 40 keV	X			X	X
3e15 at/cm^2 500 keV + 2e15 at/cm^2 40 keV		X	X		
F implants					
4e14 at/cm^2 100 keV	X				
1.08e14 at/cm^2 130 keV + 1.08e14 at/cm^2 180 keV + 2.4e14 at/cm^2 250 keV		X			
5.4e14 at/cm^2 130 keV + 5.4e14 at/cm^2 180 keV + 1.2e15 at/cm^2 250 keV			X		
2e15 at/cm^2 100 keV				X	
3e15 at/cm^2 65 keV + 9e14 at/cm^2 30 keV					X

TABLE 2.1: *Description of the implanted samples.*

Sample: high concentration C	
Si PAI	3e15 at/cm^2 250 keV + 2e15 at/cm^2 40 keV
F	3e15 at/cm^2 65 keV + 9e14 at/cm^2 30 keV
B	3.8e14 at/cm^2 12 keV + 1.3e15 at/cm^2 30 keV

TABLE 2.2: *B + F implanted sample for XAS analysis.*

In details, the samples reported in Tables 2.1 and 2.2 were produced as follows. Some Czochralski n-type (100) Si wafers were cut into several pieces, which were then amorphized from the surface to a depth of ~ 550 nm by implanting Si^- ions (3 x 10^{15} ions/cm^2 at 250 keV plus 2 x 10^{15} ions/cm^2 at 40 keV) or to a depth of ~ 1 um by implanting Si^- ions (3 x 10^{15} ions/cm^2 at 500 keV plus 2 x 10^{15} ions/cm^2 at 40 keV). The 40 keV implants were done to ensure the complete amorphization up to the surface. The silicon implants were performed by cooling the samples at the liquid nitrogen temperature (T = 77 K), in order to reduce the dynamic recombination of the point defect during the implantation itself, favoring the amorphization process. All the silicon amorphization implants were performed at the IMM-CNR section of Catania by a 1.7 MV High Voltage Engineering Europe (HVEE) Tandetron accelerator, equipped with a negative ion source.

The pre-amorphized samples were next enriched in fluorine by implanting F ions at several energies and doses as reported in Table 2.1. All F implants were performed by a 400 kV HVEE ion implanter at the MATIS CNR-INFM center in the Department of Physics and Astronomy of the University of Catania. We have realized 5 different samples divided in 3 different concentration regimes: low, medium and high dose. The low concentration regime has two samples: the sample “A” with a shallow amorphous layer and a single F implant and the sample “B” with a thicker amorphous layer and with three F implants in order to realize an uniform F concentration profile with the aim to follow the F redistribution until it reaches a steady state. The sample called “high concentration A” differs from “high concentration B” because it was created with an only F implant.

In Figs. 2.2 and 2.3 the as-implanted profiles of “low concentration A”, “low concentration B”, “medium concentration”, “high concentration A” and “high concentration B” samples are reported.

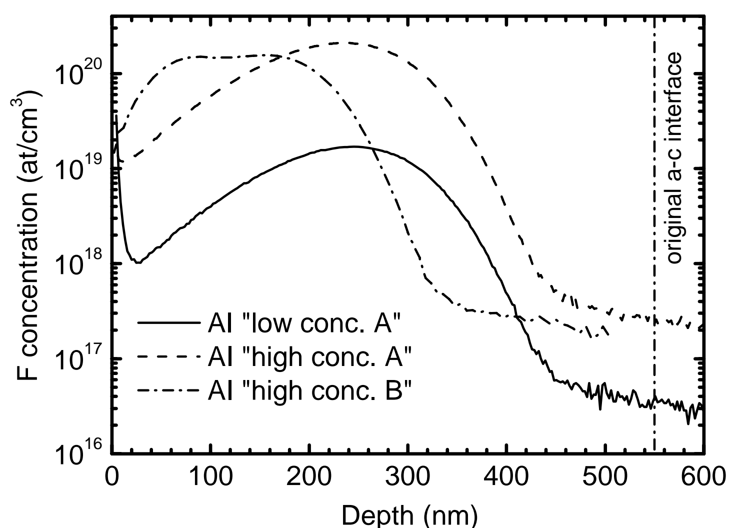

Figure 2.2: *As-implanted profiles of "low concentration A" (continuous line), "high concentration A" (dashed line) and "high concentration B" (dash-dotted line) measured by SIMS. The original a-c interface is reported by a continuous line.*

The "high concentration A" has the same energy implant of "low concentration A" but a dose nearly 10 times higher.

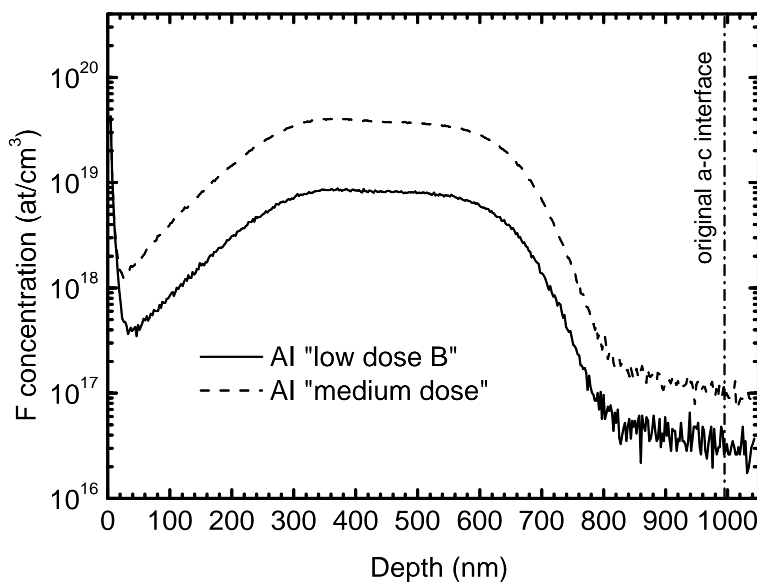

Figure 2.3: *As-implanted profiles of "low concentration B" (continuous line) and "medium concentration A" (dashed line) measured by SIMS. The original a-c interface is reported by a continuous line.*

The "medium concentration" has the same energy implant of "low concentration B" but a dose 5 times higher.

It is possible to observe how the as-implanted F profiles cover a wide range of concentrations (the F concentration peaks differ also more than an order of magnitude) and two PAI Si substrates with different initial amorphous layers were used.

For XAS analysis, we used one "high concentration B" sample and one "high concentration C". This last one was also co-implanted with B overlapping the F implanted profile. Their as-implanted profiles are reported in Fig. 2.4.

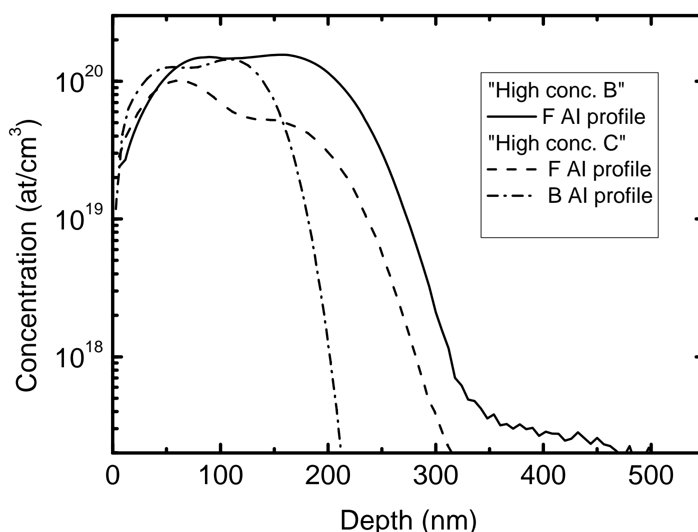

Figure 2.4: *SIMS as-implanted profiles of F and B. The continuous line refers to the F profile of the sample with F alone ("high concentration B"); dashed (dash-dotted) line is relative to the F (B) profiles of a coimplanted F and B sample. The difference in the two F profile is mainly due to different F implant conditions.*

2.3 THERMAL PROCESSES

Prior the annealing to induce the SPER, all the amorphized samples were annealed at 450 °C for 30 min to sharpen the a-c interface. The cleaning of the samples was done with isopropyl alcohol. Then the samples were partially or completely regrown by annealing in N_2 atmosphere at three different temperatures: 580 °C, 650 °C and 700 °C. The annealings at 450 °C and at 580 °C were made in a conventional horizontal furnace, while the ones at higher temperatures were done by rapid thermal annealing (RTA) processes.

The Table 2.3 indicates which samples were annealed at each temperature.

Sample	Pre-annealing	Annealing		
	450 °C 30 min	580 °C	650 °C	700 °C
Low conc. A	X	X		
Low conc. B	X	X	X	X
Medium conc.	X	X	X	X
High conc. A	X	X		X
High conc. B	X		X	

Table 2.3: *Thermal processes.*

2.3.1 Furnace annealing

The used furnace was the horizontal tubular chamber Carbolite Eurotherm 2416 CG furnace of the MATIS CNR-INFM center in the Department of Physics and Astronomy of the University of Catania.

A resistance heats the chamber by Joule's effect wrapping the central part of the tube. A retroaction automatic system controls the thermal power by reading the temperature near the resistance with a thermocouple and modulating the power in order to maintain the temperature at the pre-fixed constant value.

The samples are placed within a quartz samples-holder in the central part of the chamber, where the temperature is homogeneous within 1 °C in a position range of 10 cm. Indeed, the furnace is designed to work from room temperature to 1500 °C with the accuracy of 2 °C. Since it is necessary to wait some minutes before the samples reach the desired temperature, the furnace is not suited for annealings shorter than 10-15 minutes. The atmosphere of the chamber can be controlled by fluxing gas from an extremity to the other one of the tube. Using inert gas (N_2) the oxidation of Si is avoided.

2.3.2 Rapid Thermal Annealing (RTA)

Rapid Thermal Annealing (RTA), also referred to as Rapid Thermal Processing (RTP), is one of the most popular techniques used today to activate dopants after ion implantation. RTA offers the possibility to apply heating and cooling rates up to several hundred °C/s and to conduct processes also with a time duration of few seconds.

For this thesis, the RTA Processor Jipelec Jetfirst 150 located in the Department of Physics of Padova has been used. The scheme of the system is shown in Fig. 2.5.

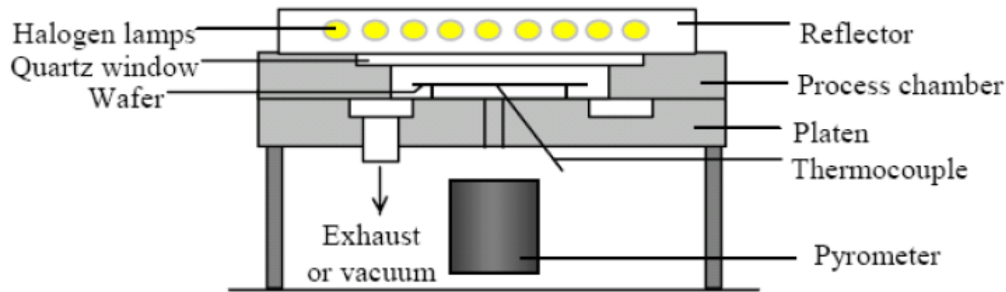

Figure 2.5: *Scheme of the RTA processor used in this work.*

The furnace consists basically of a stainless steel chamber equipped with 18 tubular infrared heating lamps. An infrared quartz window separates the process chamber from the furnace. The sample holder is a 6 inches Si wafer placed at the center of the chamber and, in order to reduce thermal conduction and avoid contaminations, is sustained only by three small beveled quartz pins. The lamp ventilation is done by compressed air, while the furnace is fully water-cooled in order to avoid secondary radiation sources and contaminations. The system is equipped with vacuum pumps and a N_2 gas line. The gas is injected by a thin circular aperture under the quartz window to give best temperature uniformity and gas distribution. Before starting the annealing, the chamber is purged by several cycles of vacuum pumping and N_2 refilling. The optical pyrometer points at the center of the wafer back side and measures the temperature using the blackbody radiation emitted from the wafer. The pyrometer reads the radiation range comprised between 4.7 μm and 5.2 μm which is different from the emission range of the lamps, avoiding wrong measurements due to lamps emission spectrum. Pyrometer calibration is carried out using a wafer with an embedded precision thermocouple, and verified by comparison of both equilibrium B diffusivity in Si and Si SPER rate to several published data. The accuracy of the calibration was tested in a previous work [Stefan] and it is equal to ± 3.5 °C. After that, calibration tables are created and used by the control system of the RTA processor. The wafer temperature is constantly monitored with the pyrometer by a P.I.D. (Proportional Integral & Derivative) controller, and the lamp power is adjusted many times per second: in this way, ramp-up rates up to 150 °C/s, overshoots less than 2 °C, and constant plateau temperatures can be achieved. An example of temperature data recorded during a 252 s annealing at 650 °C is reported in Fig. 2.6.

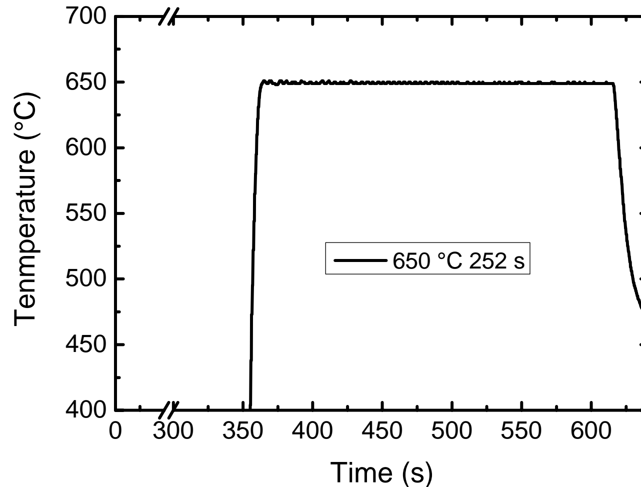

Figure 2.6: *Scheme of an RTA annealing at 650 °C for 252 s.*

Ramp-down rates are instead limited to about 50 °C/s. Error on time annealing is less than 1 s. Maximum temperatures of 1200 °C can be achieved. There are small discrepancies in temperature according to different zones of the Si wafer, that can be eliminate putting the samples in the same area of the wafer. At last the whole temperature error is estimated to be 3.5 °C.

2.4 SAMPLE CHARACTERIZATION

As said before, the characterization of the samples was done by Secondary Ions Mass Spectrometry (SIMS) measurements, X-ray Absorption Spectroscopy (XAS) analyses and High Resolution X-Ray Diffraction (HRXRD) analyses.

2.4.1 Secondary Ion Mass Spectrometry (SIMS)

The Secondary Ion Mass Spectrometry (SIMS) technique is a powerful tool to quantify the concentration of elemental impurities in a solid matrix as a function of depth. The SIMS technique is sensitive to all the chemical elements (from H to U), even if they are present only in some parts to million. SIMS allows also a very high depth resolution and dynamic range. However, it is a destructive technique and needs concentration calibration by means of measurements of suitable standards.

During a typical SIMS analysis a solid sample is bombarded in vacuum by a focused ion beam having energy in the keV range. The ions interact with the solid causing the

emission of particles from the surface. The primary ions (projectiles) penetrate into the solid transferring kinetic energy to the target atoms via nuclear (elastic) collisions. The kinetics energy, that a target atom has received, can be transferred atom by atom. From the primary ion's coming, a lot of target atoms are set in motion (collision cascade). The target atoms of the cascade situated near the surface (< 1 nm in depth) have the necessary outward directed momentum and sufficient energy to leave the target. This phenomenon is called sputtering.

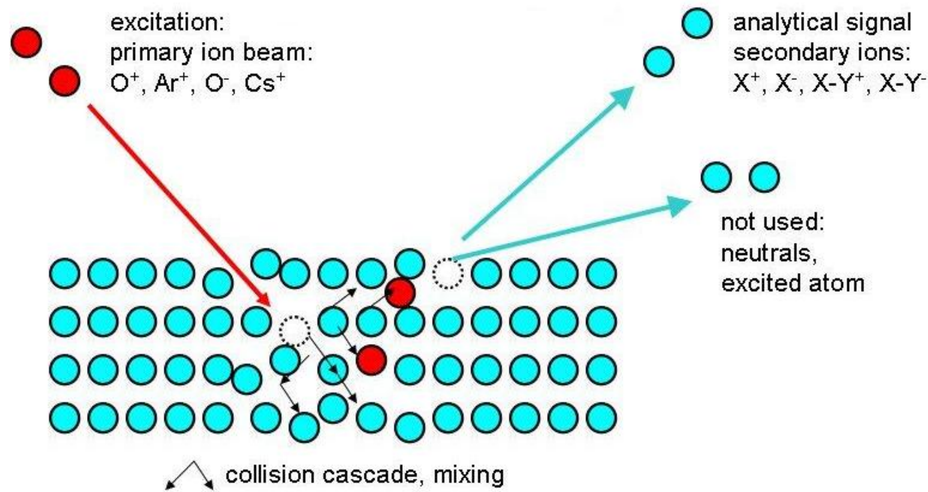

Figure 2.7: *Schematic description of SIMS analysis process.*

A small fraction (~1 %) of these particles is in a ionized state and can be subsequently accelerated by an electric field and analyzed by a mass spectrometer and then detected. The obtained mass spectrum gives information about the chemical elements present on the surface, in particular on the first atomic layers from where most of the secondary ions come.

The secondary ions yield is described by:

$$N_S^{\pm}(Z,M) = N_P \cdot Y_{tot} \cdot c(Z) \cdot a_M(Z) \cdot \alpha^{\pm}(Z) \cdot f^{\pm}(Z), \tag{2.1}$$

where $N_S^{\pm}(Z,M)$ is the detected secondary ions number, N_p the primary ions number, Y_{tot} the sputtering yield, c(Z) the concentration of the element Z, $a_M(Z)$ the abundance of the isotope M of the element Z, $\alpha^{\pm}$ ionization probability and $f^{\pm}(Z)$ the spectrometer transmittance.

The sample surface is eroded progressively by the sputter beam that scans across an area of typically 250 x 250 μm. The resulting crater has a square shape with a flat bottom in the middle. At the border of the crater, the beam (having a Gaussian shape) sputters not only material from the bottom of the crater, but also from its side walls, producing distortions of the measured profiles. The spectrometer allows to collect only sputtered ions from the center avoiding the above crater edge effects.

To calibrate the depth scale, the depth of the sputtered crater is measured by a profilometer after the SIMS analysis. Assuming a constant sputter rate, it is possible to convert the sputtering time in the sputtered depth. Finally, the concentration of the measured element as a function of the depth is obtained by comparison with calibration samples. It is necessary to use standards with the same matrix of the measured samples because the yield depends strongly on the matrix. For this work we used the CAMECA IMS-4f SIMS located in the Department of Physics of Padova. The depth resolution depends on a lot of factors, where the most important is the energy of the primary beam. An O_2^+ beam was used with the relatively low energy of 3 keV allowing a good depth resolution, that has estimated to be 6 nm FWHM (Full Width at Half Maximum). The F^+ ion was collected during sputtering and its yield was converted in concentration by comparison with an ion implanted standard. An example of SIMS F chemical profile after annealing of 90 minutes at 580 °C is reported in Fig. 2.8.

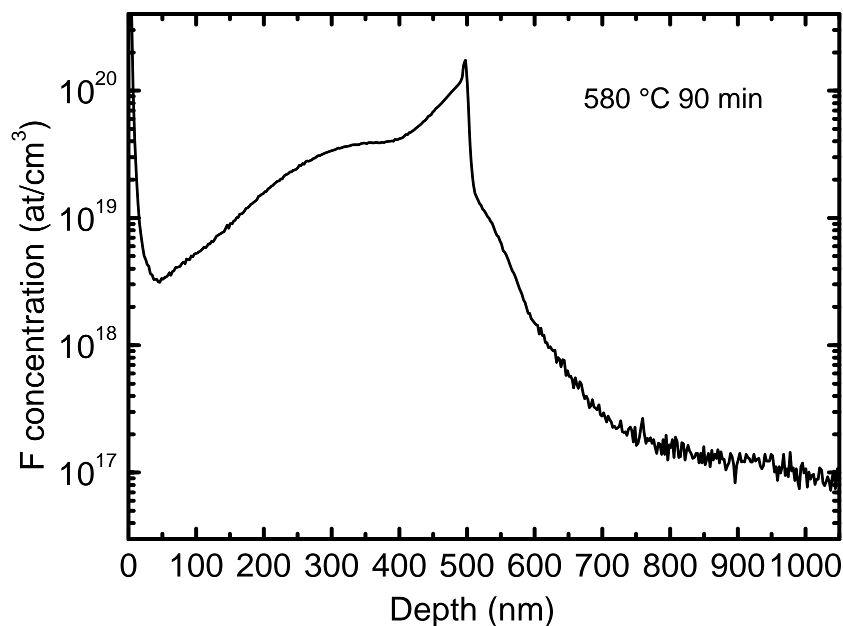

Figure 2.8: *SIMS profiles of "medium concentration" sample after annealing at 580 °C (continuous lines) for 90 minutes.*

In the first 30 nm the SIMS signal reveals high level of concentration due to an artefact of measurements (i.e. Fig. 2.8): there is a layer of the native oxide at the sample surface that increases the yield of the measured concentration. For this reason, we will not consider the first 30 nm of each SIMS profiles.

2.4.2 High Resolution X-Ray Diffraction (HRXRD)

High Resolution X-Ray Diffraction (HRXRD) is one of the most used non-destructive techniques for structural analysis of thin films. It is usually used to investigate mono-crystals, epitaxial layers and heterostructures, obtaining useful information about lattice parameters, strain, thickness and composition of the investigated materials. In this study, HRXRD technique was used to quantify the F induced strain in the crystal lattice near the a-c interface.

In order to understand the results of this technique, it is useful to remember the Bragg's law:

$$n\lambda = 2d \cdot \sin(\vartheta), \qquad (2.2)$$

where ϑ is the angle of incidence relative to the diffraction plane, d d the distance between parallel planes, n is an integer determined by the order given and λ is the wavelength of the X-rays (Fig. 2.9).

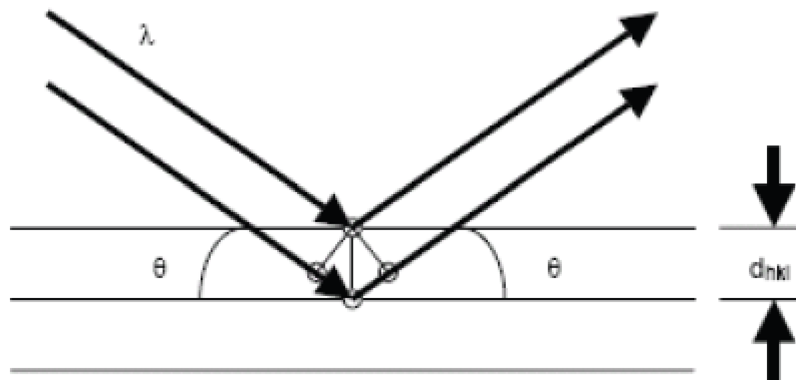

Figure 2.9: *Schematic representation of the incident and reflected X-rays.*

The Bragg's law states that when two incident X-rays with an angle ϑ reach a group of crystalline planes, characterized by Miller's indexes (hkl) and the interplanar distance d_{hkl}, they are reflected. If after their reflection the difference between rays' paths, $2d \cdot \sin(\vartheta)$, is a multiple of the wavelength, they interfere in a constructive way.

Then it is possible to acquire the distribution of diffracted X-rays' intensity as a function of the diffraction angles in a spectrum called Rocking Curve (RC). The strain of the analyzed sample is extracted from the analysis of RC.

In this work, the Philips X'PERT™ PRO MRD diffractometer of the Department of Physics of Padova University was used. A scheme of the diffractometer is shown in Fig. 2.10.

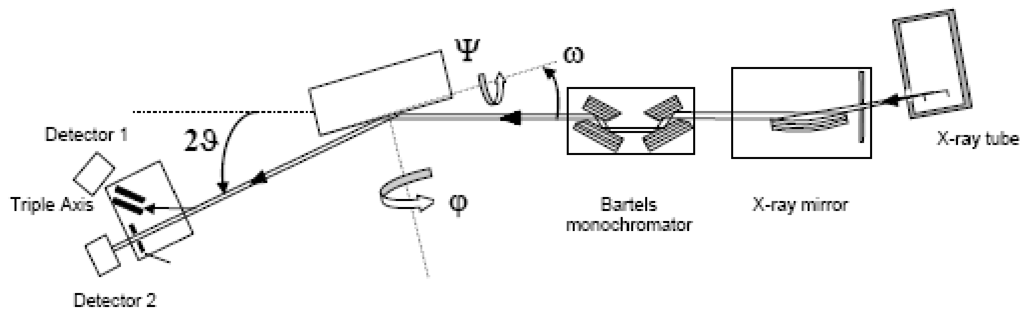

Figure 2.10: *Schematic representation of the HRXRD setup.*

A X-ray beam, produced by a Cu anode, is focused by a parabolic mirror and the Cu $K\alpha_1$ radiation is selected by a Bartels Ge (220) monochromator. By using a channel-cut Ge (220) analyzer (triple axis configuration with an angular acceptance of ~ 12 arcsec) ω–2ϑ scans (RCs) were recorded around the (004) reciprocal lattice point (ω is the angle between the incident X-Ray beam and the sample surface, while 2ϑ is the angle between the incident beam and the detector). The use of a triple axis configuration enabled us to suppress the non-coherent x-ray scattering and to improve the signal/noise ratio, so obtaining a high dynamical range of the x-ray diffracted intensity (about 6 orders of magnitude). This fact is of fundamental importance, since it allows to record very weak and subtle features of the RCs, in which detailed information about the strain status is contained. The RCs were simulated with the help of RADS MERCURY code, a commercial code based on the dynamical theory of the diffraction [Wormington]. According to this code, we can insert an arbitrary number of layers in order to simulate an experimental diffraction profile; the strain status and the thickness of every layer are the free parameters of the simulation. The simulation procedure is based on a trial and error approach and it ends when all the main features exhibited by the diffraction pattern are reproduced. The final result is a strain profile in function of the depth, with an experimental error less than 3 %.

2.4.3 X-ray Absorption Spectroscopy (XAS)

The X-ray Absorption Fine Structure (XAFS) is defined as the oscillatory trend of the X–rays absorption coefficient in the energetic range immediately subsequent to the absorption edge. These oscillations depend on different atomic structures and electronic-vibrational proprieties of the material, acting as fingerprints of their originating atomistic system. So, X-

ray absorption spectroscopy (XAS) is a technique that provides element specific structural information probing the local order of structural disordered and ordered solid.

The absorption of X-rays by matter can be explained in this simple way. A sharp increase in the absorption coefficient, known as absorption edge, occurs when the incoming photons arrive with the sufficient high energy to excite an electron from a deeper core level to a vacant excited state or to the continuum. For atoms, either in a molecule or embedded in a solid or liquid state, oscillatory variation of the absorption coefficient as a function of photon energy can be observed. X-ray absorption spectra are commonly separated into several parts according to the spectral region, as it is reported in Fig. 2.11 for example. In this case a typical X-ray absorption spectrum of Cu is reported.

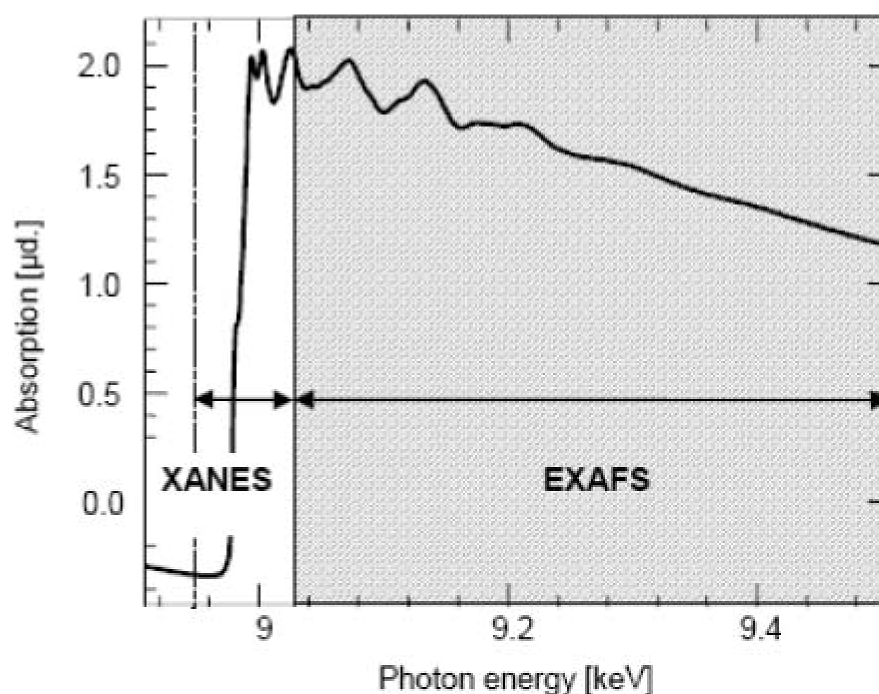

Figure 2.11: *X-ray absorption spectra of Cu K edge of a Cu/Zn0 catalyst with 70 mol-% Cu.*

It is possible to distinguish between the X-ray Absorption Near Edge Structure (XANES), contained in a region extending from before the absorption threshold E_0 (E_0 – 100 eV) to further E_0 (E_0 + 40 eV), and Extended X-ray Absorption Fine Structure, extending several hundred eV above the absorption edge and exhibiting a modulation in total absorption with the energy of the incident photon. Electron transitions and multiple-scattering events are more present in the XANES region of the spectrum, being sensitive to changes in the local density of states and the spatial arrangement of scatters around the absorber. Hence the edge region can provide information on the geometry of scatterers. Even if the XANES interpretation is

not easy and analytic, from XANES analysis a lot of information can be extracted about coordination chemistry (regular, distorted octahedral, tetrahedral), molecular orbitals (hybridization, crystal-field theory,…), band-structure and multiple scattering. It is possible to determine empirically oxidation states. From EXAFS analysis, quite complex, coordination numbers, inter-atomic distances and disorder degree can be achieved. In general XANES and EXFAS techniques allow to reconstruct the precise position and chemical type of surrounding atoms up to a radius of about 1 nm [Lamberti, DeSalvador06].

X-ray absorption measurements were performed at the ALOISA undulator beam line of the ELETTRA synchrotron radiation laboratory in Trieste, Italy. The K α fluorescence signal was recorded as a function of energy using a windowless hyperpure Ge detector. Spectra both in the near edge (XANES) and in the extended energy region (EXAFS) were recorded, with the aim of characterize the structural status of F when incorporated in crystalline Si.

Chapter 3

RESULTS AND DISCUSSION

The first part of this Chapter will be devoted to present the experimental results and their analysis and discussion. The second part will describe the model and the simulations of the experimental data.

In particular, F chemical profiles measured by SIMS will be shown first. Some quantities of physical interest will be defined and extracted from the profiles. Important insights, that will be the basis for the model development, will be obtained together with the phenomenological relationship between the F segregated at the a-c interface and the SPER rate. Then, the rate equations of the model will be shown, explaining step by step their mathematical description, based on physical considerations, of F involved processes.

Following the indications coming from the experimental results, F incorporation will be assumed as the result of F clustering that happens in a-Si and the perfect incorporation of these F cluster during the a-c interface regrowth. F diffusion will be described by a trap limited diffusion and the dynamics of the F segregation at the a-c interface by a sticking-release model.

Finally, the results of the simulations will be shown and a deepened discussion about the physical meaning of the model parameters will be done in terms of microscopical mechanisms.

3.1 EXPERIMENTAL EVIDENCES

In this first Section of this Chapter, the SIMS F chemical profiles of partially regrown or completely regrown samples will be shown, discussed and analyzed. The descriptions of the samples has been reported in Tables 2.1 and 2.2 of the Chapter 2. As outlined previously, the aim of the experimental part of this work was to characterize the evolution of F during the SPER of Si and, if possible, extract some relationships between phenomenological quantities useful to the model ideation. In order to obtain these information, we designed the annealing times in order to follow the entire F evolution from when the mobile a-c interface meets the F implant to the complete regrowth. Then, the local structure of F incorporated in c-Si after SPER will be investigated by means of XAS analyses in details. All these experimental information will constitute the basis of the model.

3.1.1 The SIMS profiles

As an example of our ability to follow the entire process of the F redistribution and incorporation during the SPER of Si, all SIMS F profiles, obtained from the samples implanted as described in Chapter 2 (Table 2.1), after partial or complete SPER at 580 °C are shown in Figs. 3.1 - 3.4. Similar profiles as a function of the annealing time were obtained at the other temperatures (650 °C and 700 °C) and their partially and completely regrown profiles were shown in Figs. 3.5 - 3.10. The a-c interface positions, valued by the peak centroids, are reported as vertical dashed lines.

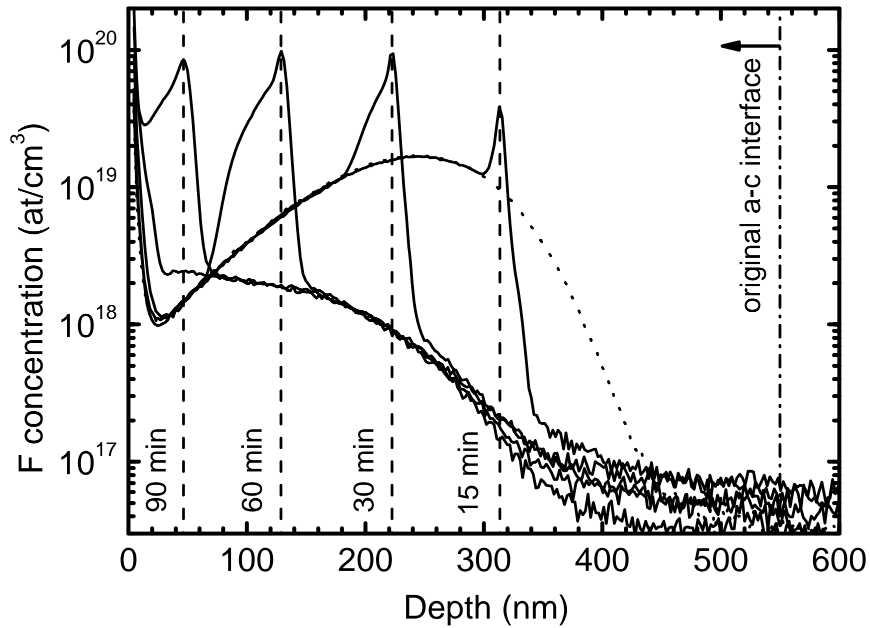

Figure 3.1: *SIMS profiles of “low concentration A” sample after implantation (dotted line) and after annealing at 580 °C (continuous lines) for different times (15, 30, 60, 90 and 120 minutes). The a-c interface positions determined as the centroid of the segregated peak are also indicated by vertical dashed lines.*

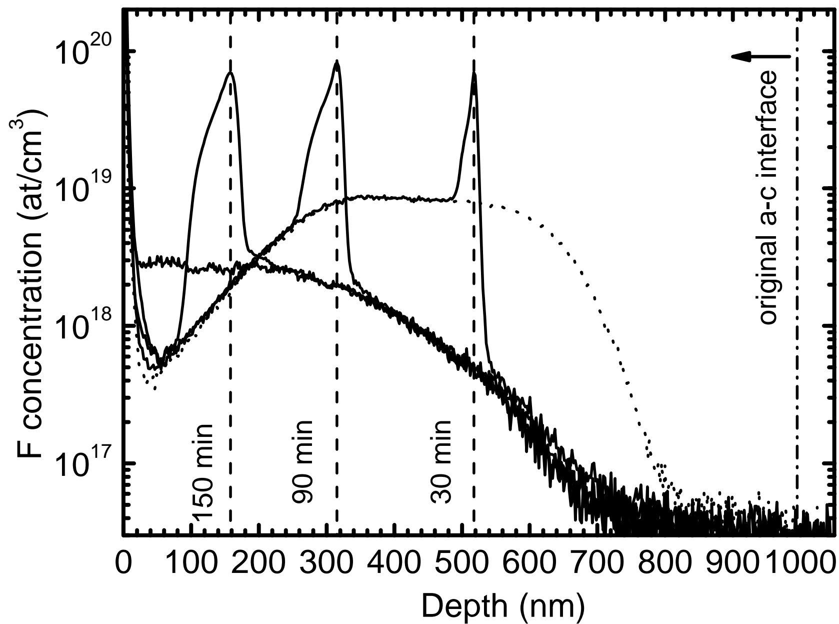

Figure 3.2: *SIMS profiles of “low concentration B” sample after implantation (dotted line) and after annealing at 580 °C (continuous lines) for different times (30, 60, 150 and 270 minutes). The a-c interface positions determined as the centroid of the segregated peak are also indicated by vertical dashed lines.*

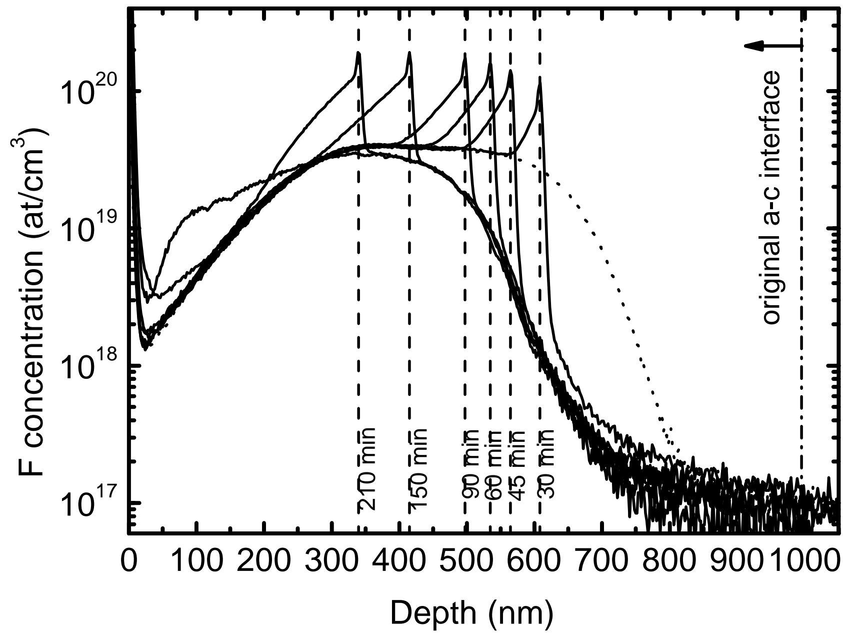

Figure 3.3: *SIMS profiles of "medium concentration" sample after implantation (dotted line) and after annealing at 580 °C (continuous lines) for different times (30, 45, 60, 90, 150, 210 and 510 minutes). The a-c interface positions determined as the centroid of the segregated peak are also indicated by vertical dashed lines.*

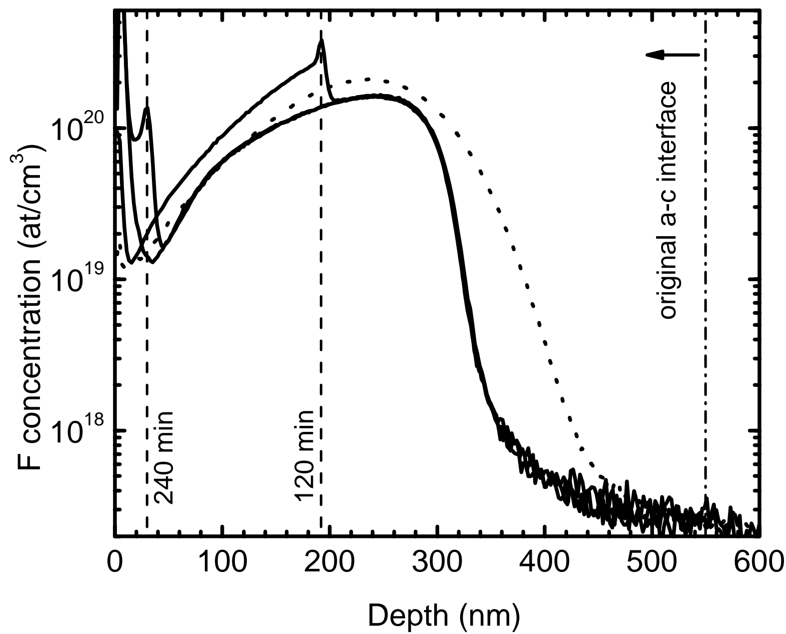

Figure 3.4: *SIMS profiles of "high concentration A" sample after implantation (dotted line) and after annealing at 580 °C (continuous lines) for different times (120, 240 and 480 minutes). The a-c interface positions determined as the centroid of the segregated peak are also indicated by vertical dashed lines.*

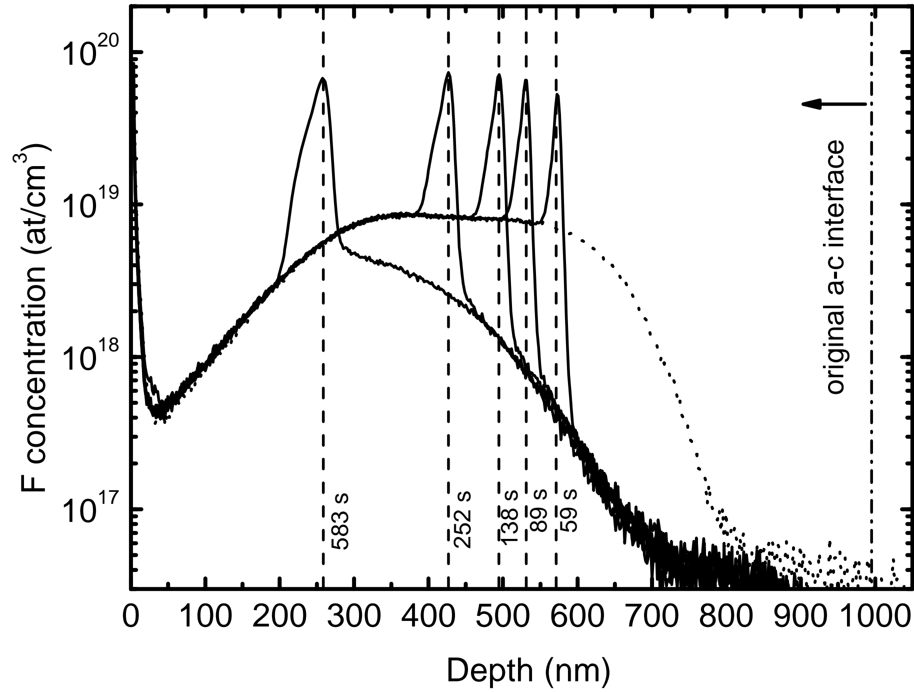

Figure 3.5: *SIMS profiles of "low concentration B" sample after implantation (dotted line) and after annealing at 650 °C (continuous lines) for different times (59, 89, 138, 252 and 583 seconds). The a-c interface positions determined as the centroid of the segregated peak are also indicated by vertical dashed lines.*

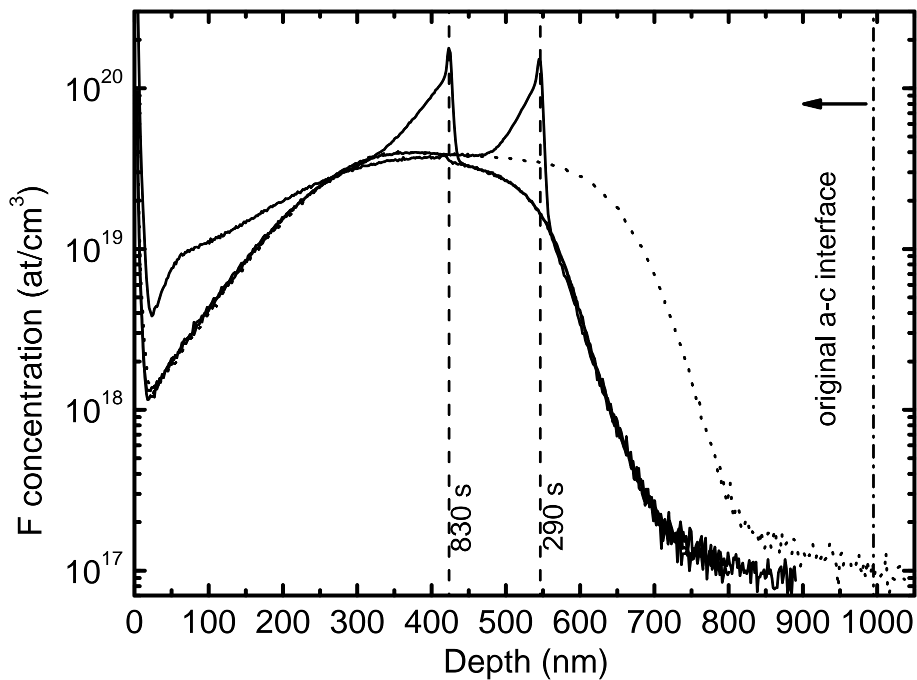

Figure 3.6: *SIMS profiles of "medium concentration" sample after implantation (dotted line) and after annealing at 650 °C (continuous lines) for different times (290, 830 and 2930 seconds). The a-c interface positions determined as the centroid of the segregated peak are also indicated by vertical dashed lines.*

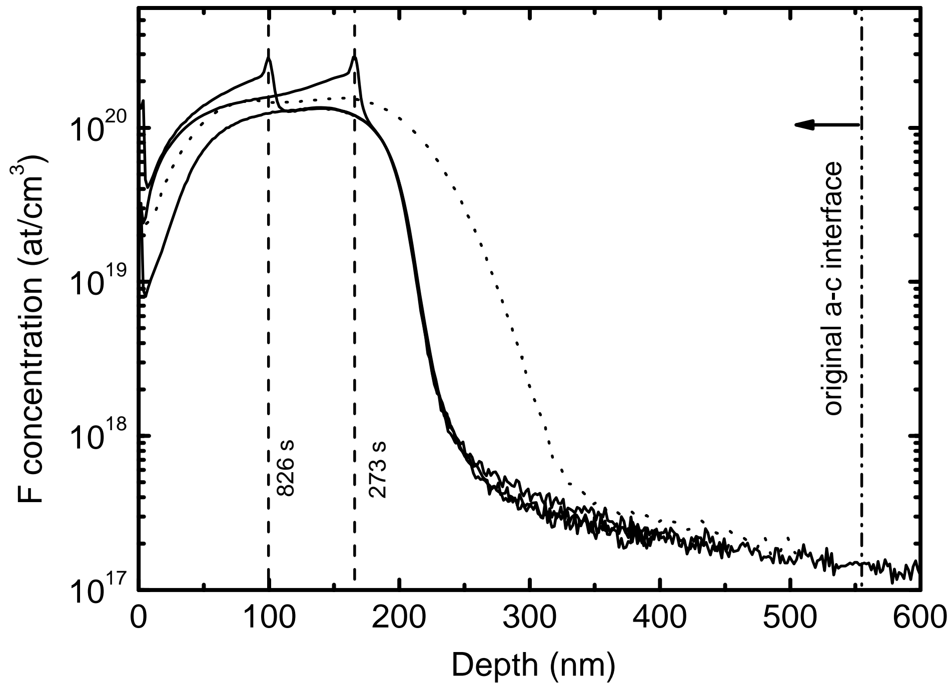

Figure 3.7: *SIMS profiles of "high concentration A" sample after implantation (dotted line) and after annealing at 650 °C (continuous lines) for different times (273, 826 and 1800 seconds). The a-c interface positions determined as the centroid of the segregated peak are also indicated by vertical dashed lines.*

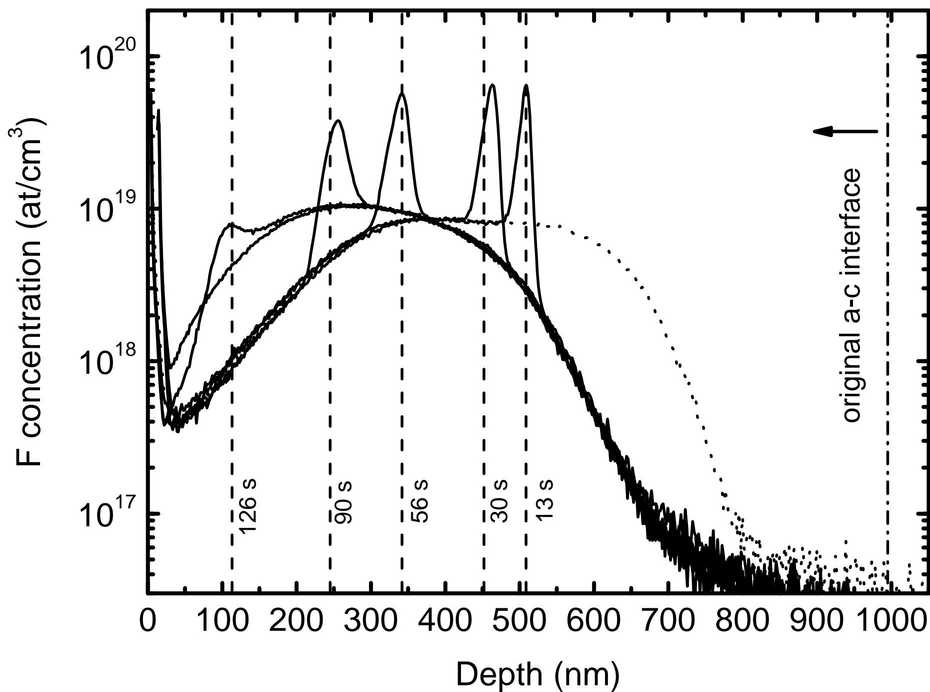

Figure 3.8: *SIMS profiles of "low concentration B" sample after implantation (dotted line) and after annealing at 700 °C (continuous lines) for different times (13, 30, 56, 90, 126 and 150 seconds). The a-c interface positions determined as the centroid of the segregated peak are also indicated by vertical dashed lines.*

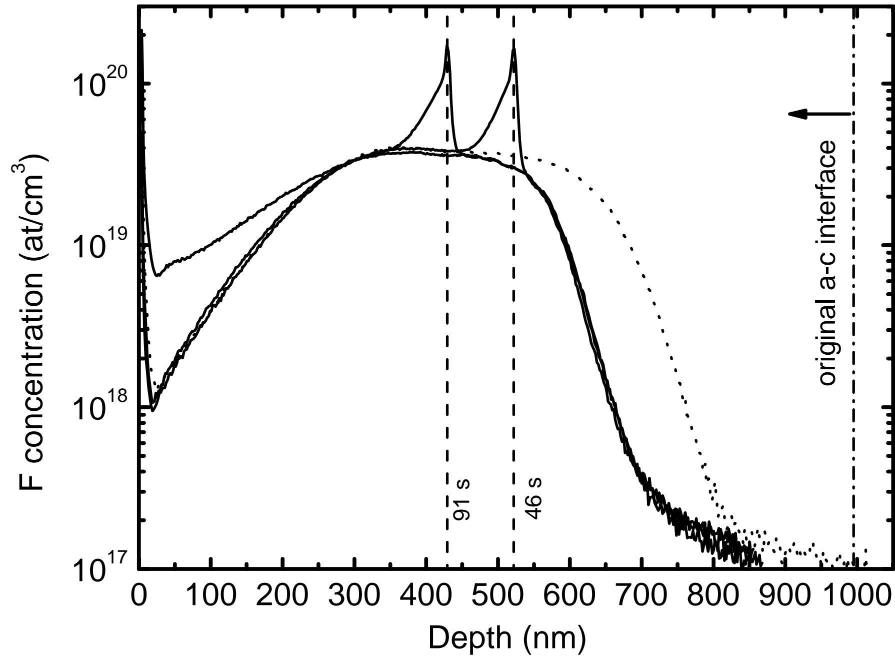

Figure 3.9: *SIMS profiles of "medium concentration" sample after implantation (dotted line) and after annealing at 700 °C (continuous lines) for different times (46, 91 and 350 seconds). The a-c interface positions determined as the centroid of the segregated peak are also indicated by vertical dashed lines.*

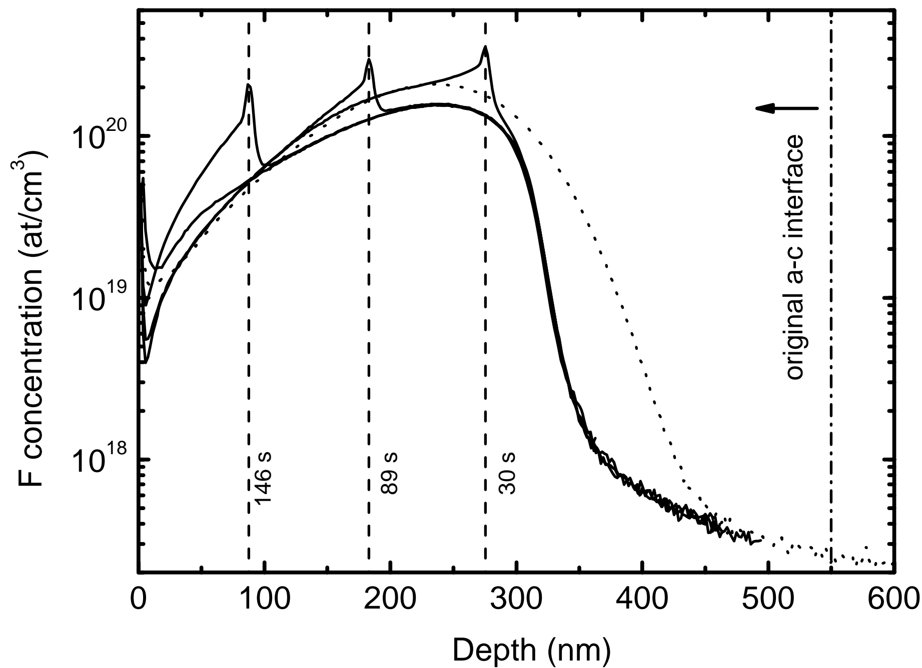

Figure 3.10: *SIMS profiles of "high concentration A" sample after implantation (dotted line) and after annealing at 700 °C (continuous lines) for different times (30, 89, 146 and 189 seconds). The a-c interface positions determined as the centroid of the segregated peak are also indicated by vertical dashed lines.*

A strong F redistribution happens during Si SPER in each data set. After F has met the a-c interface, it is always necessary more time to regrown the same quantity of a-Si, confirming the experimental evidence that F retards the SPER. As the a-c interface moves with the annealing time due to the regrowth, F segregates in a-Si splitting in two components: a diffusing tail in the residual amorphous region and a sharp peak segregated at the a-c interface. The segregated peak is usually confined in a region of ~ 20 nm, more than SIMS resolution (6 nm in this work), indicating that is not an artefact of measurement. We have not any evidences, but in literature it is reported that once SPER is completed the F in the peak evaporates from the surface [Jeng]. On the crystalline side F is incorporated at a concentration much lower, even 2 orders of magnitude less, than the F concentration at the amorphous side of the a-c interface. The F profile in c-Si does not change during SPER indicating that F incorporated does not modify its configuration, so F diffusion in c-Si is negligible. The samples with thicker amorphous layer and almost "medium concentration" of F (Figs. 3.3, 3.6 and 3.9) show a saturation value for the F incorporated concentration, confirming that we did a correct design of the experiment because we achieved our objective to follow the entire F redistribution process.

3.1.2 The analysis of a typical F segregated peak

In Fig. 3.11 a magnification of a segregation peak close to the a-c interface is shown in order to characterize better the F peak and define some phenomenological quantities.

Observing Fig. 3.11, it is evident that three different zones should be considered corresponding to the regions of a three-phase system [Lau, Orlowski]: the amorphous phase, the crystalline phase and the region of the F peak segregated at the interface (i.e. the interface layer).

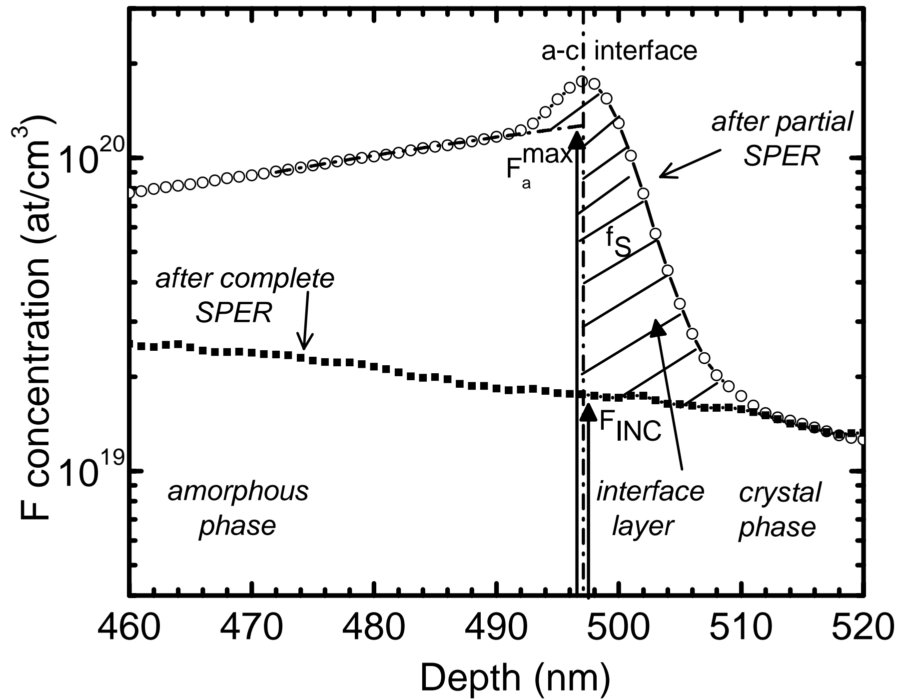

Figure 3.11: Enlargement of the fourth F peak (open circles) of Fig. 3.3 (annealing at 580 °C for 90 minutes). The arrows indicate the F concentration in a-Si at the a-c interface (F_a^{max}) and the F incorporated in c-Si concentration at the a-c interface (F_{INC}), while the F areal density of the a-c interface phase (f_S) is represented by the cross-hatched area.

In order to have a deeper and comparative analysis of the main features that appear in the F profiles, a first quantitative analysis was performed by extracting several quantities directly from the profiles by simple extrapolation/integration operations. These quantities are:

I) the a-c interface depth approximated as the peak centroid position of the F concentration profile (indicated by dash-dotted line);

II) the concentration of F in the amorphous phase at the a-c interface depth assumed as the extrapolated F concentration (F_a^{max}) from the diffusing tail in the amorphous phase;

III) the incorporated F concentration in the crystalline phase at the a-c interface depth (F_{INC}), directly extracted from the completed regrown profile considering that F in c-Si has negligible diffusion;

IV) the F areal density of the a-c interface phase (f_S) estimated by integrating the profile in the interface layer zone after subtraction of the F in amorphous and crystalline phases (represented by the cross-hatched area);

V) the regrowth velocity estimated as the incremental ratio of the a-c interface positions and annealing times.

The last four quantities were plotted in Fig. 3.12 versus time for the "medium concentration" at 580 °C in order to show how they evolve while the Si SPER goes on.

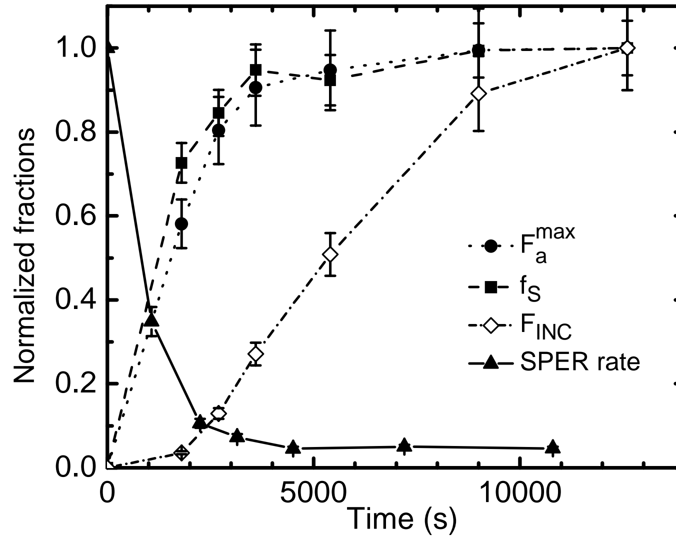

Figure 3.12: The fraction of F_a^{max}, f_S, F_{INC} and SPER rate with respect to their maximum value extracted from "medium concentration" samples annealed at 580 °C are reported versus annealing time. The lines are only guides for eyes.

We normalized each quantity in Fig. 3.12 to its maximum value: 7.0 x 10^{19} at/cm^3 for F_a^{max} (closed circles), 9.3 x 10^{13} at/cm^2 for f_S (closed squares), 3.5 x 10^{19} at/cm^3 for F_{INC} (open diamonds) and 0.456 nm/s for SPER rate (closed triangles) [Olson]. We reported the mean SPER rate extracted by derivative of the a-c interface depth as function of time and referred it to the mean time of each time interval.

As can be noted, F in amorphous (F_a^{max}) and F segregated in the peak (f_S) are very well correlated one another. We can also note that the SPER rate reaches a steady state with the same characteristic time of f_S and F_a^{max}, suggesting a strong correlation between these three quantities. Instead, F_{INC} is the only quantity that is not correlated with any other one: when the other quantities have reached the saturation value, the F incorporated in the crystal still continues growing, nearly doubling its value before reaching the maximum. We observed similar trends in all other series of data. Therefore it is impossible to assert that F incorporation is only a function of f_S and F_a^{max}. This means that a further quantity should be introduced in order to successfully model the incorporation process. This crucial point can be interpreted by considering what we actually know about F incorporation in c-Si [Section

1.7.5], i.e. that nano-bubbles filled by F nucleate in bulk a-Si before they are incorporated in c-Si [Boninelli08]. It is therefore quite natural to suppose that the hidden variable of the problem should be related to F-induced nano-bubbles nucleation in a-Si, i.e. a process that might evolve with time once diffusion and interface segregation have reached saturation. Consequently, in order to describe satisfactorily the F incorporation in c-Si, we will assume that F in the amorphous phase can be distinguished in two different states, i.e. the F free to diffuse, hereafter called F_D, and the F clustered, F_C, and we will consider the dynamics interplays between F_D and F_C. The clustered F in a-Si, F_C, will be incorporated in c-Si during SPER. Following suggestions coming from the above analysis, we have performed an experimental study focused entirely on the F clustering, that will be described in the next Section 3.1.3.

In order to investigate the correlation between f_S and the SPER rate evidenced in Fig. 3.12, we plotted the SPER rate normalized to the Si intrinsic SPER rate [Olson] versus the F areal density at the a-c interface. Figure 3.13 shows the plots related to the three SPER temperature (580 °C, 650 °C and 700 °C), using all data available at each temperature. The f_S data reported in the plots are the mean values between two areal densities of peaks consecutive in time.

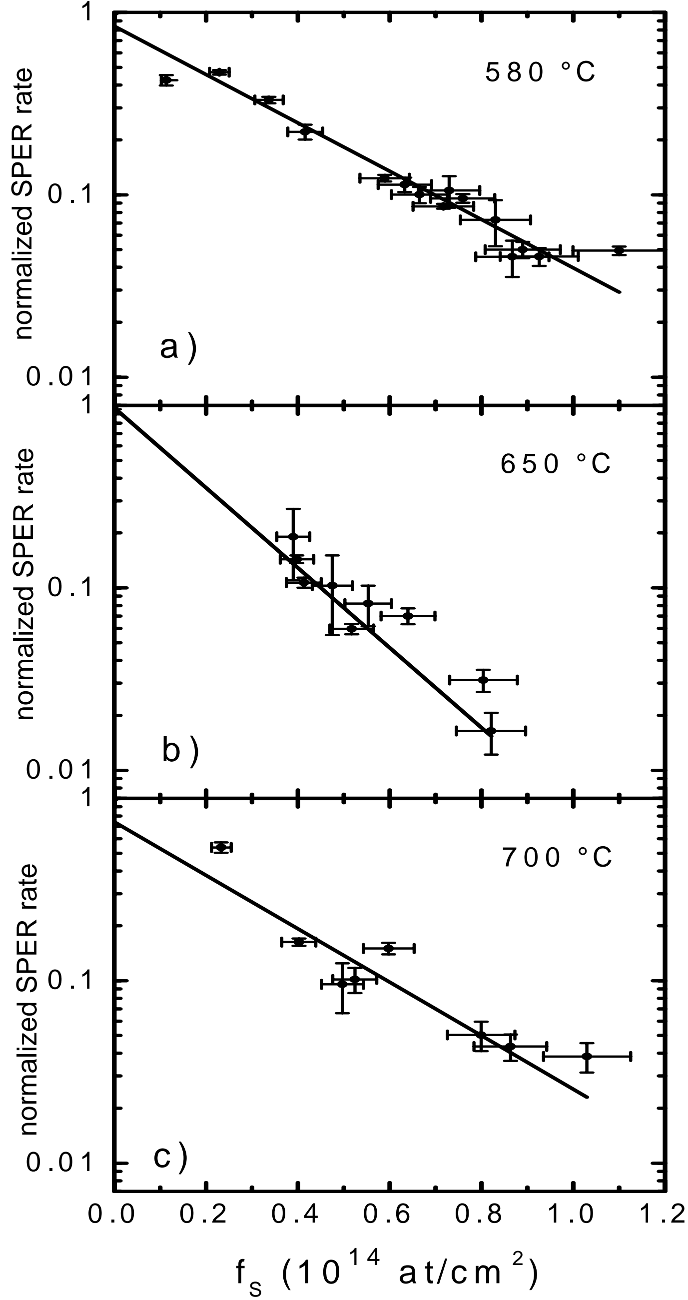

Figure 3.13: *Normalized SPER rate versus F areal density at the a-c interface for samples annealed at* **(a)** *580 °C,* **(b)** *650 °C and* **(c)** *700 °C. Continuous exponential lines are described by Eq. (3.1) and their values are reported in the Table 3.1.*

We interpolated the data in Fig. 3.13 with this exponential law:

$$\frac{v}{v_0} = A \cdot e^{-\frac{f_S}{f_S^0}}, \tag{3.1}$$

where v_0 is the SPER rate of intrinsic Si [Olson] and f_S^0 is the reduction coefficient of SPER rate due to f_S.

The fits parameters are reported in Table 3.1:

Temperature	A	f_S^0 (10^{14} at/cm^2)
580 ° C	(0.84 ± 0.02)	(0.328 ± 0.005)
650 ° C	(0.97 ± 0.05)	(0.198 ± 0.005)
700 ° C	(0.74 ± 0.07)	(0.297 ± 0.018)

Table 3.1: *Parameters obtained by normalized SPER vs. F areal density at the a-c interface (f_S).*

As v_0 we assumed the values reported by Ref. [Olson]. If the intrinsic SPER rates in our samples were exactly the same estimated by Olson *et al.*, the A parameter would be equal to 1. The values of the parameter A obtained by our fits are quite compatible with 1 even if they do not match perfectly with it. It is necessary to take into account that we referred to the nominal SPER temperatures and small discrepancies in temperature process could explain these differences. We noted also that the f_S^0 trend is not linear with temperature. The following phenomenological equation [Eq. (3.2)] will be assumed in the following for the modelling:

$$v = v_0 \cdot e^{-\frac{f_S}{f_S^0}} . \quad (3.2)$$

3.1.3 Formation of SiF_4 molecules in a-Si and their incorporation in c-Si

As shown in Section 1.7.1, F clustering is the result of the coalescence of F atoms and dangling bonds in a-Si causing the formation of F-induced nano-cavities, that are then incorporated in c-Si by the passage of the a-c interface. *Ab initio* calculations suggested that F atoms stabilizes the V clusters by saturating the internal dangling bonds of Si. However, a direct experimental determination of the local structure of F was still lacking before this thesis work.

With the aim to discover how F is redistributed in the nano-cavities, we have determined the local structure of F implanted in PAI Si by means of X-ray absorption spectroscopy. As said in Section 2.4.3, XAS technique is sensitive to the precise position and chemical type of surrounding F atoms up to a distance of about 1 nm. We used the result of XAS analysis to test theoretical hypotheses of local structures and/or to extract direct information such as interatomic distances at different coordination shells. For XAS analysis, we used one "high concentration B" sample and one "high concentration C" sample. This last

one was co-implanted with B overlapping the F implanted profile, as reported in Section 2.2 (Fig. 2.4). The two samples were annealed at 650 °C for 30 minutes (Fig. 3.14) and at 800 °C for 10 s (Fig. 3.15).

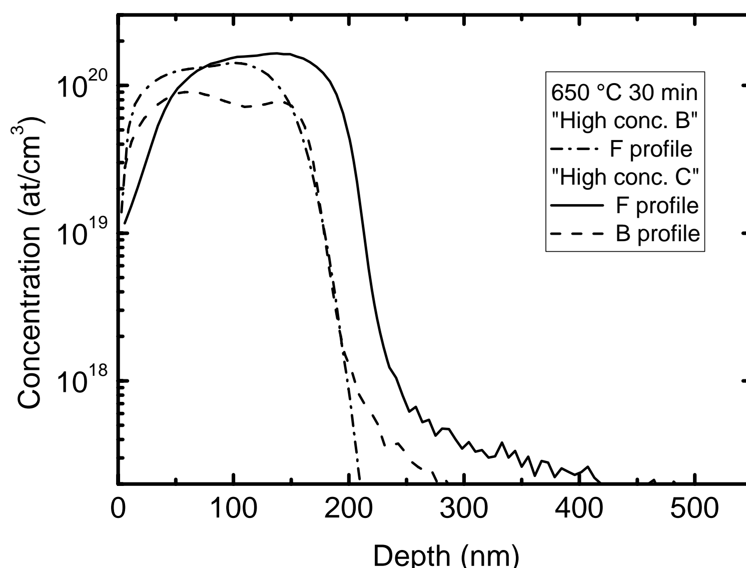

Figure 3.14: *SIMS as-implanted profiles of F and B impurities after regrowth of PAI samples at 650 °C. The continuous line refers to the F profile of the sample ("high concentration B") with F alone; dashed (dash-dotted) line is relative to the F (B) profiles of a co-implanted F and B sample [DeSalvador09].*

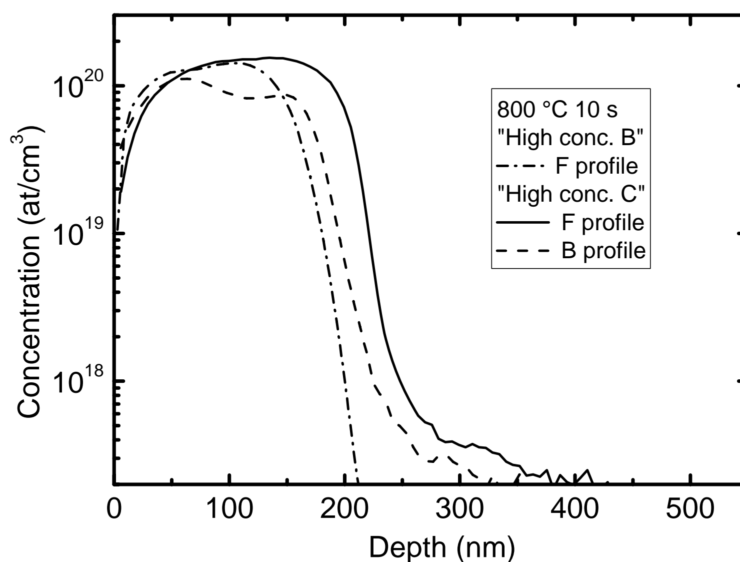

Figure 3.15: *SIMS as-implanted profiles of F and B impurities after regrowth of PAI samples at 800 °C. The continuous line refers to the F profile of the sample ("high concentration B") with F alone; dashed (dash-dotted) line is relative to the F (B) profiles of a co-implanted F and B sample [Baggio].*

We extracted from these samples their XANES and EXAFS spectra by XAS analysis. The X-ray absorption measurements were performed at the ALOISA undulator beam line of

the ELETTRA synchrotron radiation laboratory in Trieste, Italy. The used experimental setup, the acquisition system and spectra elaborations were reported in Ref. [Baggio]. In Fig. 3.16 the experimental XANES spectra for the two samples regrown at 650 °C are reported with thick lines [DeSalvador09].

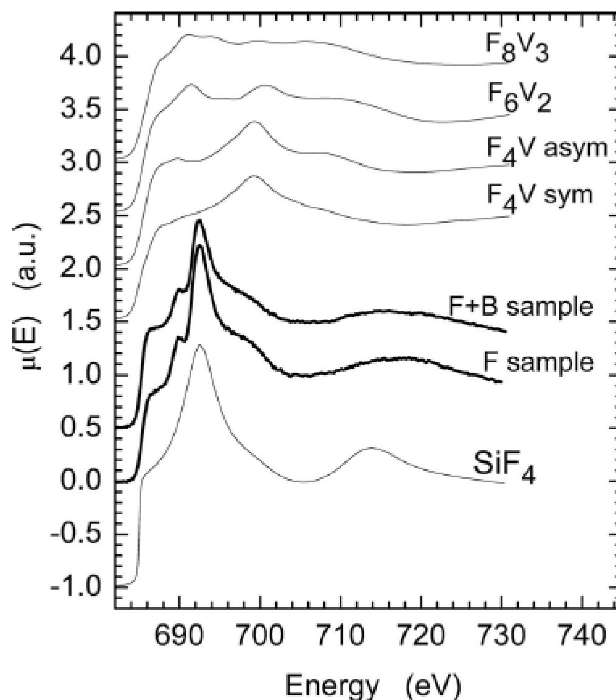

Figure 3.16: *XANES spectra. Thick lines are experimental spectra for the sample with only F implant ("high concentration B") and F + B co-implanted sample ("high concentration C") at 650 °C. Upper thin lines are simulations of spectra based on F-V theoretical clusters. F_4V is simulated in both symmetric (sym) and asymmetric (asym) structures [Lopez05]. The lower line is a simulation based on the Si_F4 molecule structure [DeSalvador09].*

The two spectra are identical each other, so the local F structure is very similar in presence of B or not, with the result to exclude the formation of B - F complexes, as already demonstrated by our group in the past [Impellizzeri07]. We obtained similar spectra (not shown) for samples regrown at 800 °C, suggesting that the direct interaction of B with F does not occur at any temperature.

With the aim to discover the atomistic structure of F, the spectra were analyzed in-depth by my research group using *ab initio* calculations. *Ab initio* simulations of the XANES lineshape were performed in the full multiple scattering frame-work and muffin-tin approximation using the FEFF code [FEFF]. The reliability of the simulations was validated by comparing the simulated and experimental CaF_2 spectrum in the fluorite structure at the F *K*-edge (not shown) [Baggio]. All the experimental features were successfully reproduced by

the simulation as far as the energy positions and, to a lesser extent, the relative intensities are concerned.

In a first attempt of reproducing the XANES spectra on our sample, we used as input for the spectral simulations the coordinates of *V*-F clusters proposed by Lopez *et al.* [Lopez05] on the basis of *ab initio* structural simulations, i.e., the F_4V cluster, both in symmetric and asymmetric configurations, the F_6V_2, and the F_8V_3 clusters. The clusters are extended by adding Si atoms on diamond lattice sites so as to obtain 500 atom spherical clusters. Final simulations were obtained as the weighted sum of individual ones for all the nonequivalent F sites in each cluster, the weight being equal to the site symmetry degeneration. Figure 3.16 shows the results of the calculations (upper thin lines). It is evident how none of the simulations can reproduce the experimental features. Besides, as the structural complexity of the clusters increases the spectral features of the simulated spectra become less pronounced (compare the simulation for the simple F_4V cluster to that for the more complex F_8V_3 one). If bigger clusters with analogous structures (for instance cavities with inner dangling bonds saturated with F) were to be considered, the main spectral features of the spectra would not be reproduced. In order to consider simplified F structures, some simulations that consider F interstitial sites and partially saturated F-*V* clusters (F_3V, F_2V and F*V*) were tried, even in this case without any success. The above analysis demonstrates that most F atoms are found neither in the sites predicted by the theoretical calculations reported so far, nor in bigger F-*V* clusters.

More insights on the local configuration of F incorporated in PAI Si can be obtained by analysis of the EXAFS spectra reported (Fig. 3.17) In view of the limited signal-to-noise ratio (a consequence of the high dilution of F), the raw EXAFS oscillations were fitted with a single F–Si contribution in the *k*-range 3–8.5 $Å^{-1}$, using the FEFFIT [FEFF] code and *ab initio* phase and amplitude functions [Ankudinov].

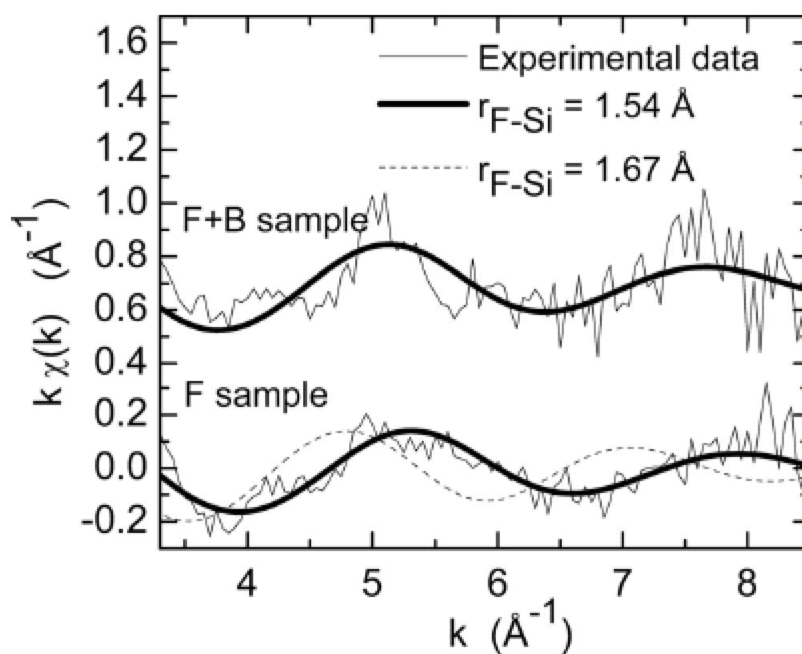

Figure 3.17: *Thin lines are the experimental EXAFS spectra for the pure F sample and the F+B coimplanted sample. Solid lines are first coordination shell fit of the data with F-Si distance R_{F-Si} = (1.54 ± 0.02) Å in agreement with the Si-F distance in the SiF_4 molecule. The dashed line is a simulation with R_{F-Si} = 1.67 Å (typical distance in F-V clusters), which clearly is unable to reproduce the spectra [DeSalvador09].*

A F–Si distance of (1.54 ± 0.02) Å was found for both spectra and also for the samples annealed at higher temperature (not shown). This distance is smaller than the theoretical F–Si distance (about 1.67 Å) in clustering involving F and V. The common structure in all F-V clusters considers this characteristic distance of the F–Si bond when the Si atom is bound to other three Si atoms. Other theoretical interstitial configurations exhibit even longer F–Si distances. The dashed line in Fig. 3.17 shows a simulation with a F–Si distance of 1.67 Å. It is clear that notwithstanding the significant noise in the data, the discrepancy between experiment and theory is well above the noise. The very short F–Si distance found from our data is instead characteristic of the SiF_4 molecule (1.56 Å) [Masao], which exhibits the most polar and therefore strongest and shortest bond obtainable between Si and F atoms [Stillinger]. Thus, we performed a simulation of the XANES spectra based on the structure of the SiF_4 molecule (Fig. 3.16): this simulation is the only one that reproduces the main features of the experimental spectra.

The clear conclusion that can be drawn from the above results is that the great majority of F atoms are incorporated in Si in the form of SiF_4 molecules. Lopez *et al.* [Lopez05] correctly noted that the most stable bond between Si and F is that found in SiF_4 molecules, but ruled out the molecule as the final state for F in *c*-Si in view of supposed kinetic limitations.

Actually, the present study demonstrates that the system finds a pathway to reach and accommodate this very stable gaseous phase in the crystalline Si matrix.

3.2 THE RATE EQUATIONS MODEL

A parallel and simultaneous quantitative description of all the four phenomena evidenced above (i.e. the F retardation effect on SPER, F diffusion and clustering in a-Si and F segregation) is fundamental to model the F redistribution during SPER. In fact, these phenomena happen simultaneously and strongly influence one another. We formulated physical models for each process, and then we coupled the rate equations of all the processes in an overall model. After, for each annealing temperature, we fitted the whole data set with our model simultaneously with a single set of physical parameters.

In the following description each physical phenomenon involving F will be treated and described separately assuming that the others were already satisfactorily modelled. In this way, we will able to discuss separately the physical origin of each phenomenon and present the tests made with the model in order to validate or discard the assumptions made. The model presented here is the most successful in term of chi-square minimization while keeping the number of free parameters as low as possible, i.e. a correction to the model was accepted if it had significantly improved the simulations features or decreased the number of free parameters.

3.2.1 F clustering in a-Si

In order to model correctly F clustering in a-Si is fundamental to consider all experimental observations presented in literature and discovered by us (see Section 3.1.3). With all information available is possible to make a comprehensive picture that describes the F incorporation in c-Si very well. It is known that SiF_4 molecules form in the amorphous phase as nuclear magnetic resonance measurements demonstrated [Kumeda]. From Boninelli *et al.*'s studies [Boninelli06, Boninelli08] (Section 1.7.1), we learned that also nano-bubbles form in the amorphous phase when F is present. Consequently it is reasonable to affirm that nano-bubbles formation is induced to accommodate SiF_4 molecules in the amorphous matrix. Lastly the SiF_4-filled nano-bubbles are transferred from the amorphous bulk to the crystal phase by the passage of the a-c interface, as described in Section 1.7.1 (Fig. 1.30)

[Boninelli08]. This is very probably the way by which the molecules are incorporated in the crystal, where our measurements clearly detect their presence (Section 3.1.3). This picture is well compatible with all experimental results and it will the base of the modellization of the F clustering mechanism in a-Si and incorporation one in c-Si.

In our model it is assumed that F clusters form in a-Si but they might also dissolve before the arrival of the incoming a-c interface. During the a-c interface motion we assumed a perfect incorporation of the F clusters in our model. Moreover, we assumed that the F diffusion in c-Si is negligible, as suggested by the experimental data (Figs. 3.1 - 3.10). We modelled the F clustering and incorporation through the following equations:

$$\frac{\partial[F_C]}{\partial t} = 4\pi\delta[N_0]D_{FD}[F_D] - \eta[F_C] \quad \text{for } x \leq R, \tag{3.3}$$

$$\frac{\partial[F_C]}{\partial t} = 0 \quad \text{for } x > R, \tag{3.4}$$

$$[F_{INC}] = [F_C] \quad \text{for } x \geq R. \tag{3.5}$$

In the above equations, as well as hereafter in this thesis, square brackets represent concentrations, that are also a function of the depth x. The a-c interface moves with time and we define R its position . We have considered in Eq. (3.3) the clustering rate proportional to a capture radius δ, to the clusters concentration ($[N_0]$), to the F diffusivity (D_{FD}) in a-Si and to the concentration of diffusing F ($[F_D]$). $[F_C]$ can decrease with time due to the dissolution term that is the product of $[F_C]$ and the dissolution rate η.

Besides all the above assumptions (Section. 3.1.3), we have considered that the capture radius δ may grow with the clustered F content due to the growth of the cluster size, increasing the clustering probability. We have simply assumed that all F clusters have the shape of spherical nano-bubbles (assumption supported by TEM measurements [Boninelli06, Boninelli08]), so the average volume of the cluster, V_{cl}, will be equal to

$$V_{cl} \approx \frac{4}{3}\pi \cdot \delta^3, \tag{3.6}$$

and these clusters are filled with a certain volume density of F, ρ (assumption supported by the XANES results reported in Section 3.1.3). Assuming that all F_C is contained in the clusters, it is obviously that

$$F_C = V_{cl} \cdot \rho \cdot [N_0]. \tag{3.7}$$

From the Eqs. (3.6) and (3.7), we have deduced the capture radius δ as

$$\delta \approx \left(\frac{3}{4\pi\rho} \frac{[F_C]}{[N_0]} \right)^{1/3} , \tag{3.8}$$

Finally, we have considered the possible existence of an initial capture radius, not depending on F content, necessary to start the growth of the clusters with the first F trapping, and we have assumed that is equal to a_0 (the first nearest neighbour distance in Si, 0.235 nm) in first approximation. So the capture radius δ was defined as:

$$\delta = a_0 + \left(\frac{3}{4\pi\rho} \frac{[F_C]}{[N_0]} \right)^{1/3} . \tag{3.9}$$

In the present form the model has 3 physical parameters to describe the clustering phenomenon: the clustering nucleation density $[N_0]$, the volume density of F in the cavities (ρ) and a dissolution rate η. These can be considered as a minimal set of parameters to describe the clustering probability, the growth of F capturing with cluster size and the possible re-emission of F from the clusters. Of course the model is simplified since we have assumed a constant amount of nucleation sites, a single possible density of F in the bubble during growth and a single release rate, and we did not considered any F clusters size distribution.

In Fig. 3.18 we compare the simulation results of "low concentration B" and "medium concentration" samples annealed at 580 °C using our best model, described above, with the simulations obtained by assuming that clustering does not occur and that the diffusing F in a-Si incorporates into c-Si by a first order kinetic model with a finite probability (1%) of F incorporation in c-Si at this temperature as suggested by Zographos *et al.* [Zographos], as reported in Sec. 1.7.5. Only assuming F clustering is possible to fit simultaneously and correctly the highest levels of F incorporation in "low concentration B" [Fig. 3.18 (a)] and "medium concentration" [Fig. 3.18 (b)], while this is not possible by assuming a classic first order segregation.

Fitting attempts of the experimental data with the above model have demonstrated that these parameters are sufficient to describe the main features of the phenomenon producing satisfactory simulation results of the F incorporation in c-Si, as shown in Fig. 3.18 (dash-dotted lines).

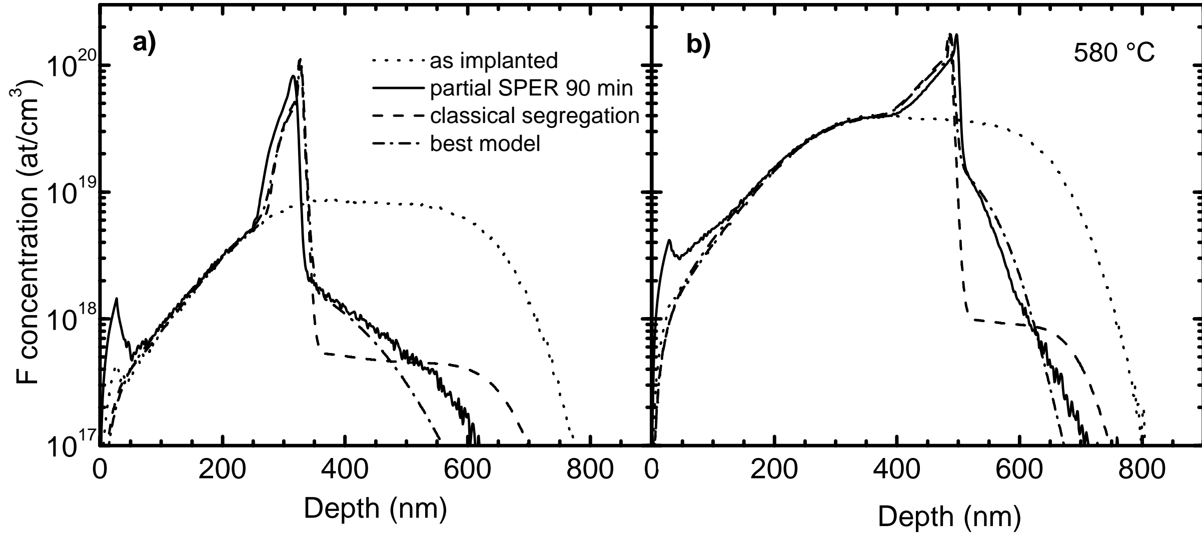

Figure 3.18: *F SIMS profiles for* **(a)** *"low concentration B"* **(b)** *and "medium concentration" samples just after implantation (dotted lines), and after SPER at 580 °C for 90 min (continuous line). Simulations using a classic segregation [Zographos] (dashed line) or our model based on the incorporation of clustered F (dash-dotted line) are reported for comparison.*

Trying to fit the whole set of data, it was evident that a strong correlation between ρ and η parameters exists, hampering the convergence of both of them. Therefore, we decided to make a further assumption by fixing ρ to a reasonable value. We assumed that SiF_4 molecules are close packed [we considered a face-centred cubic (FCC) lattice as a limit case] with the distance from centres equal to 0.6 nm, being equal twice the sum of Si-F distance and F covalent radius. Considering that there are 4 sites for each lattice cell, 4 F atoms in each site, and the taken up volume by a single tetrahedral molecule as a cubic volume where the late of the cube is obtained by multiplying the centres distance by $\sqrt{2}$, ρ is equal to

$$\rho = \frac{4 \cdot 4}{\left(0.6nm \cdot \sqrt{2}\right)^3} = 26.2 \frac{at}{nm^3}, \tag{3.10}$$

Any other attempt to reduce the number of the parameters, such as for example by considering a constant capture radius, produced a significant worsening of the fitting quality. On the other side, any attempt to include additional incorporation mechanisms such as incorporation of mobile F in c-Si from the amorphous phase or incorporation of F directly from the interface layer, or considering partial incorporation of clustered F did not give any appreciable improvement to the simulations producing at the same time an increase of the number of parameters, and therefore we omitted the above processes in the model.

3.2.2 F diffusion in a-Si

As can be noted in Figs. 3.1-3.10, the F diffusion in a-Si is not constant and it is much more pronounced close to the a-c interface where the F concentration is high and it is quite minimum at lower concentration close to the surface (this can be understood noting that the profiles far from the a-c interface do not change in time before its arrival). This fact is quantitatively demonstrated in Fig. 3.19.

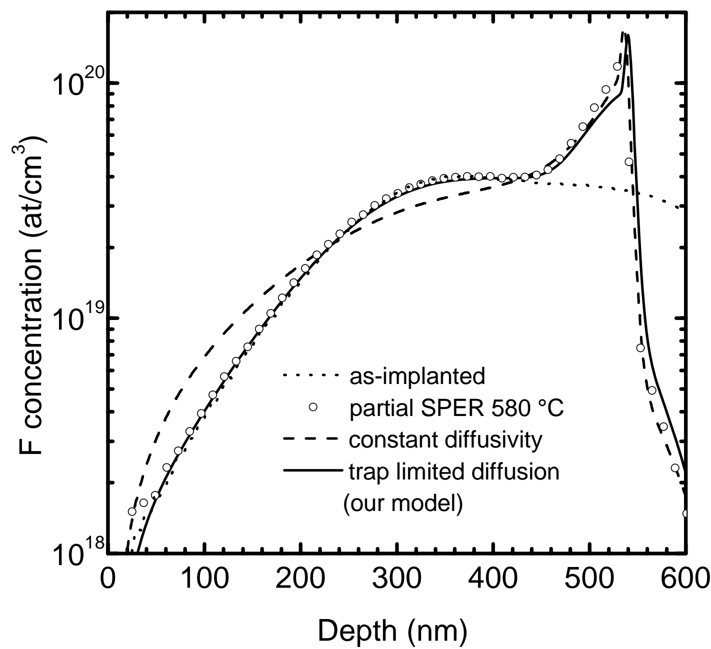

Figure 3.19: *F SIMS profiles of "medium concentration" sample just after implantation (dotted line) and after annealing at 580 °C for 60 min (open circles). Simulations using constant diffusivity (dashed line) or our model based on a trap limited diffusion (continuous line) are reported as comparison.*

The dashed line tries to reproduce the experimental data (open circles) by a constant diffusion coefficient, but it fails overestimating the F quantity able to diffuse in the a-Si layer and it is not reproducing the correct shape of the peak. The above considerations suggest that diffusion may be concentration dependent (it increases by increasing the concentration) or position dependent (it increases closer to the interface).

In Fig. 3.20 we can see that a pure concentration dependent diffusion may be ruled out.

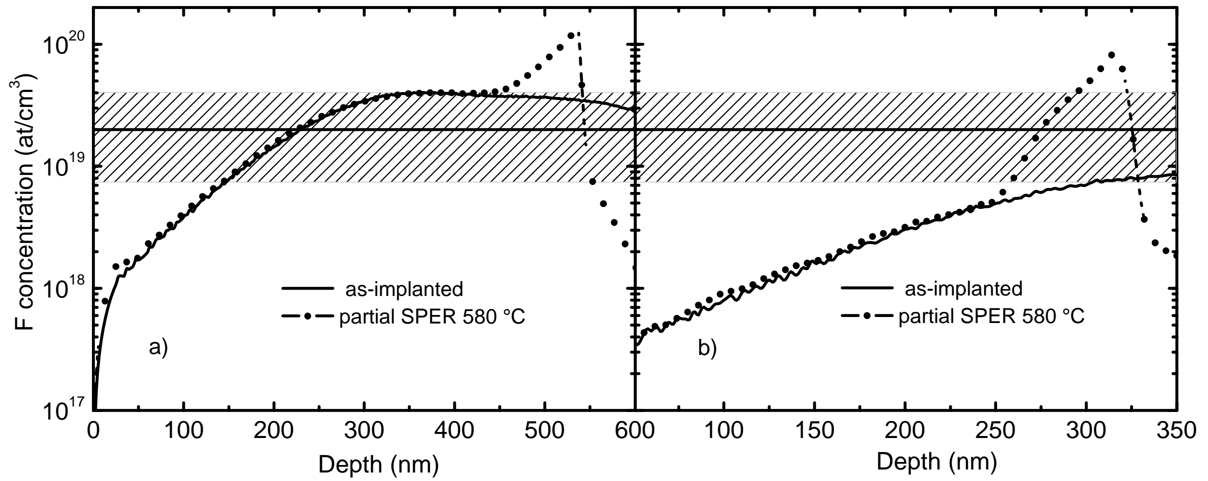

Figure 3.20: **(a)** *F SIMS profiles of "medium concentration" sample just after implantation (continuous line) and after annealing at 580 °C for 45 min (closed circles).* **(b)** *F SIMS profiles of "low concentration B" sample just after implantation (continuous line) and after annealing at 580 °C for 90 min (closed circles).*

As a matter of fact, looking at the two chemical profiles at the same concentration level of 2 x 10^{19} at/cm^3 (the thick continuous line in the middle of the grey layer), diffusion can be observed in one sample [Fig. 3.20 (b)] but not in the other one [Fig. 3.20 (a)] that was treated at the same temperature (580 °C in this case) but with a higher implant dose. We confirmed this qualitative idea by performing several simulations (not shown) with different functional dependences of F diffusivity against F concentration and no satisfactory agreement was reached contemporaneously for all the samples.

Thus our starting point is the reasonable consideration that there are a lot of defects in amorphous Si [Pantelides, van den Hoven, Urli, Roorda, Coffa and Bernstein06] that can interact with the mobile F that undergoes a trap-limited diffusion. F interacts with bulk defects, for example dangling bonds, that act as trap for F mobile atoms, creating complexes and reducing the concentration of F able to migrate. The trapping reaction is described by:

$$[F_I]+[T]\leftrightarrow[FT], \tag{3.11}$$

where F_I represents the mobile F atoms in a-Si, T the traps and FT the non diffusive complex. We have also introduced the parameter k regulating the equilibrium reaction according to the mass action law:

$$\frac{[F_I][T]}{[FT]}=k \ . \tag{3.12}$$

Therefore, the F diffusing state in a-Si (F_D) is split in two parts: the F mobile (F_I) and F temporarily bonded to a trap (FT). The conservation of the total number of traps and diffusive fluorine gives the relations:

$$[F_D] = [F_I] + [FT], \tag{3.13}$$

$$[T]_0 = [T] + [FT], \tag{3.14}$$

where $[T]_0$ is the total amount of traps before the interaction with F.
Thus the diffusivity can be written as:

$$D_{FD} = D_{FI} \frac{[F_I]}{[F_D]}. \tag{3.15}$$

The F_D diffusivity (D_{FD}) is proportional to the F_I diffusivity (D_{FI}) multiplied by the fraction of moving F, i.e. $[F_I]/[F_D]$. This last ratio can be expressed as a function of $[F_D]$, $[T]_0$ and k by solving the system given by Eqs. (3.12-14).
Extracting [T] from Eq. (3.14) and inserting it in Eq. (3.12):

$$k = \frac{[F_I]([T]_0 - [FT])}{[FT]}. \tag{3.16}$$

Thus,

$$k \cdot [FT] = [F_I]([T]_0 - [FT]) \Rightarrow [FT] = \frac{[F_I]\cdot[T]_0}{k + [F_I]}. \tag{3.17}$$

Inserting [FT] as formulated by Eq. (3.17) in Eq. (3.13), Eq. (3.18) is obtained:

$$[F_I]\cdot\left\{1 + \frac{[T]_0}{k + [F_I]}\right\} = [F_D] \Rightarrow [F_I]^2 + (k + [T]_0 - [F_D])\cdot[F_I] - [F_D]\cdot k = 0 \tag{3.18}$$

Solving this second grad equation, we have found that the ratio $[F_I]/[F_D]$ can be expressed as a function of $[F_D]$, $[T]_0$ and k in this way:

$$\frac{[F_I]}{[F_D]} = \frac{(-k - [T]_0 + [F_D]) + \sqrt{(k + [T]_0 - [F_D])^2 + 4[F_D]\cdot k}}{2[F_D]}. \tag{3.19}$$

The diffusivity is regulated by the equilibrium of reaction described by Eq. (3.11) that determines how much F is free at equilibrium through Eqs. (3.15) and (3.19). Such equilibrium depends on the concentration of traps that are present in the sample. As an example, we calculated that at low F concentration, the diffusivity is obtained when $[F_A] \rightarrow 0$ solving the limit of (3.15):

$$\lim_{[F_A]\to 0} D_{FD} = \lim_{[F_A]\to 0} D_{FI} \frac{[F_I]}{[F_D]} \overset{H}{=}$$

$$= \lim_{[F_A]\to 0} \frac{1}{2} + \frac{\{4k - 2(k + [T]_0 - [F_D])\}}{4\{(k + [T]_0 - [F_D])^2 + 4[F_D]\cdot k\}^{1/2}} = \tag{3.20}$$

$$= \frac{1}{2} + \frac{2(k - [T]_0)}{4(k + [T]_0)} = \frac{k}{k + [T]_0}$$

On the contrary, calculating the limit of (3.15) when $F_D >> T_0$, the diffusivity reaches a maximum value D_{FI}:

$$\lim_{[F_D]>>[T]_0} D_{FD} = \lim_{[F_D]>>[T]_0} D_{FI} \frac{[F_I]}{[F_D]} =$$

$$= \lim_{[F_D]>>[T]_0} D_{FI} \frac{(-k - [T]_0 + [F_D]) + \sqrt{(k + [T]_0 - [F_D])^2 + 4[F_D]\cdot k}}{2[F_D]} = \tag{3.21}$$

$$= D_{FI} \frac{(-k + [F_D]) + \sqrt{(k + -[F_D])^2 + 4[F_D]\cdot k}}{2[F_D]} = D_{FI}$$

In order to calculate D_{FD} as a function of the depth with the aim to account for the observed increase of the F diffusivity close to the a-c interface, at each temperature we have assumed that $[T]_0$ is a function of the position throughout the amorphous layer. In order to describe the increase of diffusivity close to the a-c interface we propose that $[T]_0$ is constant (equal to $[T]_{bulk}$) except in the proximity of the a-c interface, that is considered as a perfect sink for traps, where traps concentration decays exponentially (Fig. 3.21), through the following equation:

$$[T]_0(x) = [T]_{bulk}\left(1 - e^{\frac{x-R}{\mu}}\right), \tag{3.22}$$

where μ is the traps capture-length at the a-c interface and R represents the a-c interface position.

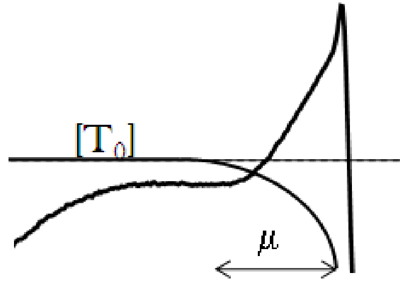

Figure 3.21: *Schematic representation of the trap concentration profile near the a-c interface.*

The above model for diffusion has 4 parameters (D_{FI}, k, $[T]_{bulk}$, μ) and is implemented with the boundary conditions that the sample surface is a perfect sink for mobile F as expressed by:

$$[F_D(0)] = 0\,, \tag{3.23}$$

while the advancing interface perfectly rejects the diffusive F.

We have already shown in Fig. 3.19 that all the features of the diffusion are reproduced well by the above model. The absence of the diffusion far from the interface is due to that fact that the F concentration is well below the trap concentration, while close to the interface diffusion occurs thanks to the trap depletion. When the F concentration is higher than the trap concentration, all the traps are saturated so the F diffusion can occur also far from the a-c interface.

3.2.3 F segregation at the a–c interface

In this paragraph we present the mathematical implementation of the model needed to simulate the areal density of F segregated at the a-c interface, f_S. Thanks to the relation of this quantity with the regrowth velocity [see Eq. (3.2)], a good prediction of f_S with time is crucial.

In our model the F segregation at the a-c interface is well reproduced by assuming a flux of F (f_{S_in}) coming from the amorphous phase during SPER:

$$f_{S_in} = \alpha \cdot v\,[F_D(R)]\,. \tag{3.24}$$

This flux is equal to the areal density of F that is interested by regrowth per unit time $v[F_D(R)]$ multiplied by a proportionality factor α that represents the fraction of such areal density that is trapped into the interface phase (α can be thought as a segregation factor at the

a-c interface). It is also necessary to consider a second term that describes the releasing flux of F from the interface phase to the amorphous bulk, f_{S_out}:

$$f_{S_out} = \beta \cdot f_S \,, \tag{3.25}$$

that is assumed to be simply proportional to the F amount into the interface phase, f_S, being β a proportionality constant representing the dissolution rate of f_S.

Other terms were considered without success such as the possible release of F toward the crystalline phase and the possible reduction of F trapping at the interface region by approaching a saturation dose. The first term might be a possible channel of incorporation and the second one might be reasonably due to the finite availability of sites for the phase in a 2D system. Both terms did not significantly improve the simulation of the data and so were neglected. From a microscopical point of view, this would suggest that F can incorporate only through F clustering, as discussed deeply in Section 3.1.3, and F at the a-c interface reaches its equilibrium alone and the a-c interface is never saturated but it could receive more F atoms. Thus, F segregation is described by a creation and a dissolution term through the following equation:

$$\frac{\partial f_S}{\partial t} = \alpha \cdot v \cdot \left[F_D\left(R\right)\right] - \beta \cdot f_S \,. \tag{3.26}$$

The quality of the prediction of the evolution of f_S during SPER is assessed in Figs. 3.22-3.25, where the F areal density, f_S, is plotted versus the time. At each temperature, dashed lines (simulation) and open triangles (experimental) are used for "low concentration A and B" samples, continuous lines (simulation) and closed circles symbols (experimental) for "medium concentration", dotted lines (simulation) and semi-closed squares (experimental) for "high concentration A or B". It is clear from the figures that the simulation data allow to account for the variation of f_S with time very well. The only data that are not simulated correctly are those relative to first partial SPER annealings of "high concentration A and B" samples where the model underestimates the experimental points. The reason could be attributed to more initial F segregation due to the elevate quantity of F atoms moved by the a-c interface that could receive all them. Then this phenomenon reaches its equilibrium at lower value of F dose. During the formation of the segregated peak the segregation coefficient might change its value to a higher transient one. On the whole, we can model the f_S evolution with the same analytical expression in the entire temperatures range.

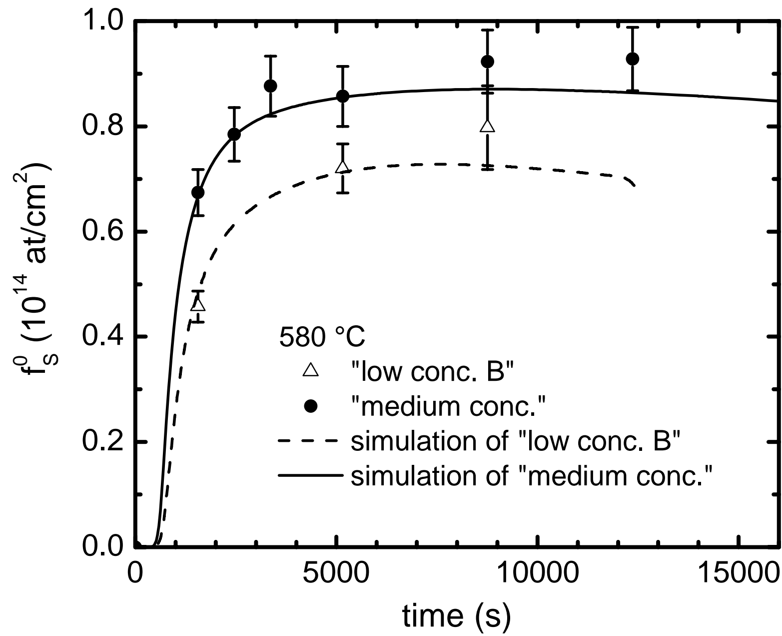

Figure 3.22: *F areal density at the a-c interface, f_S, of "low concentration B" (open triangles) and "medium concentration" (closed circles) for the temperatures of 580 °C versus the SPER time. Simulations are reported for comparison (dashed and continuous lines).*

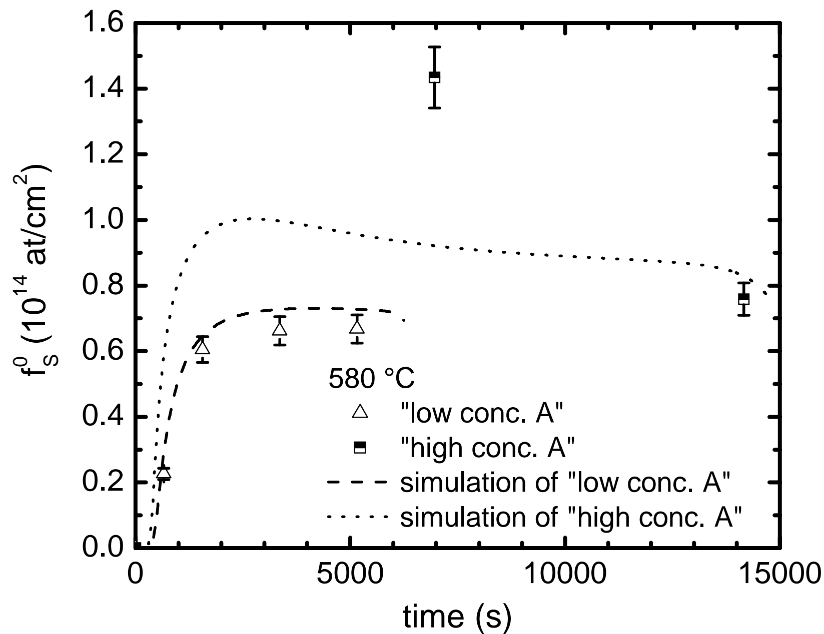

Figure 3.23: *F areal density at the a-c interface, f_S, of "low concentration A" (open triangles) and "high concentration A" (semi-closed squares) for the temperatures of 580 °C versus the SPER time. Simulations are reported for comparison (dashed and dotted lines).*

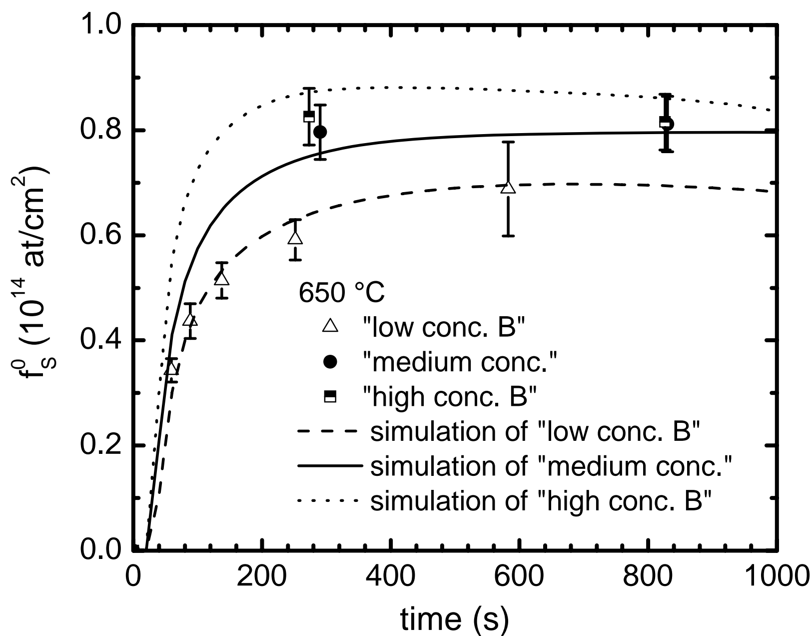

Figure 3.24: *F areal density at the a-c interface, f_S, of "low concentration B" (open triangles), "medium concentration" (closed circles) and "high concentration B" (semi-closed squares) for the temperatures of 650 °C versus the SPER time. Simulations are reported for comparison (dashed, continuous and dotted lines).*

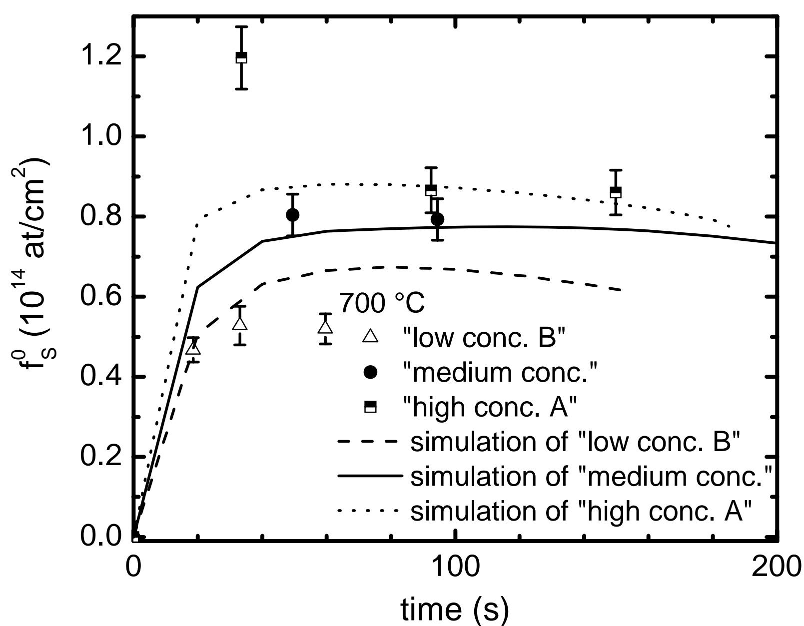

Figure 3.25: *F areal density at the a-c interface, f_S, of "low concentration B" (open triangles), "medium concentration" (closed circles) and "high concentration B" (semi-closed squares) for the temperatures of 700 °C versus the SPER time. Simulations are reported for comparison (dashed, continuous and dotted lines).*

In Figs. 3.26-3.28 we show how the above model allows also a fine prediction of the a-c interface positions through Eq. (3.2). At each temperature, dashed lines (simulation) and open or closed triangles (experimental) are used for "low concentration A and B" samples, continuous lines (simulation) and closed circles (experimental) for "medium concentration", dotted lines (simulation) and semi-closed squares (experimental) for "high concentration A or B". The model is able to reproduce the interface positions well within an average error of ~ 15 nm with a single value of f_S^0 coefficient for each temperature.

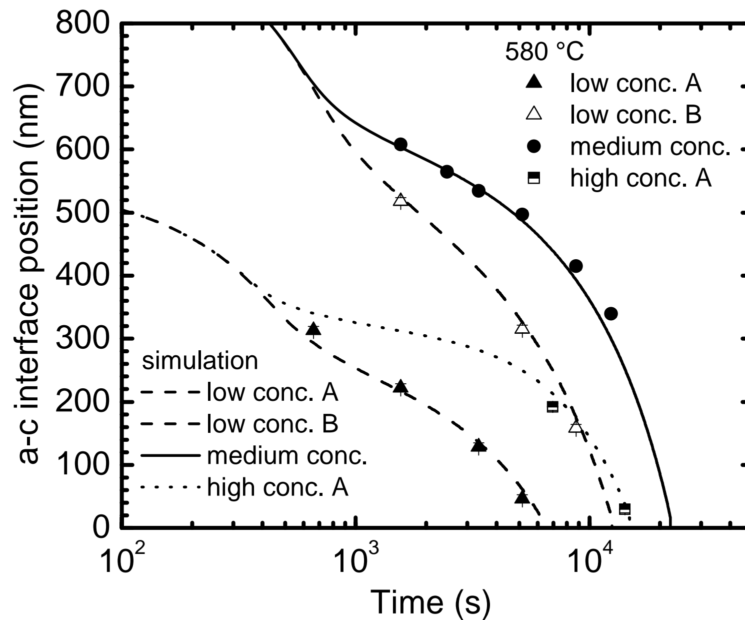

Figure 3.26: *The position of the a-c interface R of "low concentration A" (closed triangles), "low concentration B" (open triangle), "medium concentration e" (closed circles) and "high concentration A" (semi-closed squares) versus time at 580 °C. The simulations are described by Eq. (3.2). The errors are less than the width of the dots.*

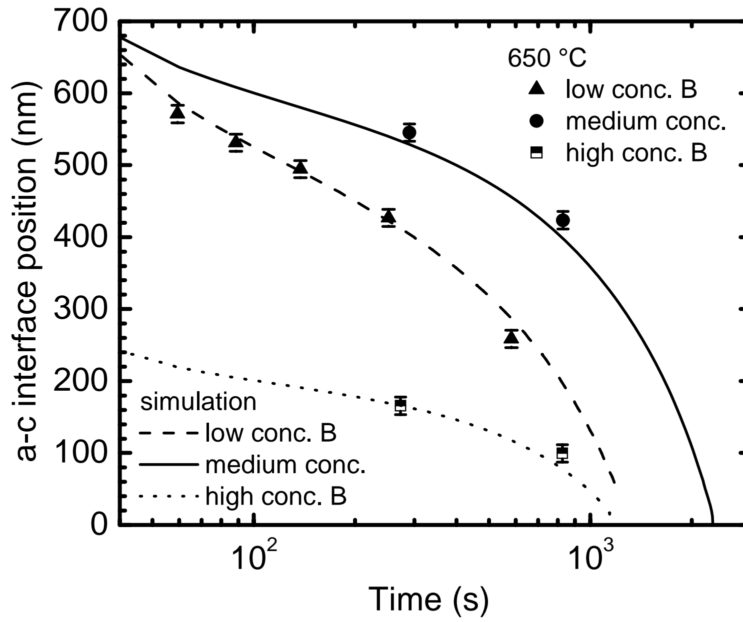

Figure 3.27: *The position of the a-c interface R of "low concentration B" (open triangles), "medium concentration" (closed circles) and "high concentration B" (semi-closed squares) versus time at 650 °C. The simulations are described by Eq. (3.2).*

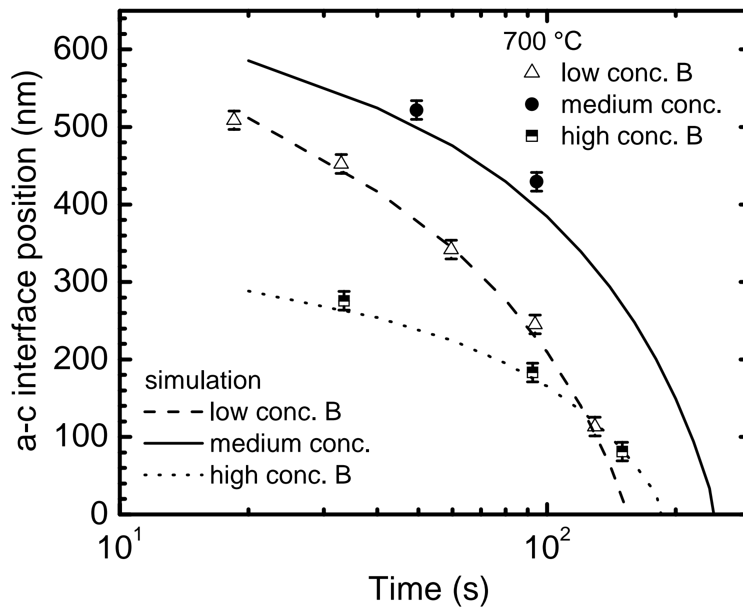

Figure 3.28: *The position of the a-c interface R of "low concentration B" (open triangles), "medium concentration" (closed circles) and "high concentration A" (semi-closed squares) versus time at 700 °C. The simulations are described by Eq. (3.2).*

In analogy with the proposed formula we tried to add some other retardation effects by including exponential factors depending on the clustered or/and diffusive F at the a-c interface

without any significant improvement of the fits. These factors have therefore been omitted in the final version of the model.

3.2.4 The complete model

As previously discussed, the F retardation effect on the SPER rate, F clustering and diffusion in a-Si occur simultaneously and influence each other. All the equations introduced previously (Sections 3.2.1, 3.2.2 and 3.2.3) are coupled in an overall model based on rate equations and algebraic ones able to fit all data sets at each SPER temperature:

$$\frac{\partial[F_D]}{\partial t} = \frac{\partial}{\partial x} D_{FD} \frac{\partial[F_D]}{\partial x} - 4\pi[N_0]\cdot\left(a_0 + \left(\frac{3}{4\pi\rho}\frac{[F_C]}{[N_0]}\right)^{1/3}\right) D_{FD}[F_D] + \eta[F_C] \quad \text{for } x \le R, \quad (3.27)$$

$$\frac{\partial[F_C]}{\partial t} = 4\pi[N_0]\cdot\left(a_0 + \left(\frac{3}{4\pi\rho}\frac{[F_C]}{[N_0]}\right)^{1/3}\right) D_{FD}[F_D] - \eta[F_C] \quad \text{for } x \le R \quad (3.28)$$

$$\frac{\partial f_S}{\partial t} = \alpha \cdot v[F_D(R)] - \beta \cdot f_S, \quad \text{for } x \le R, \quad (3.29)$$

$$\frac{\partial[F_C]}{\partial t} = 0 \quad \text{for } x > R, \quad (3.30)$$

$$[F_{INC}] = [F_C] \quad \text{for } x \ge R, \quad (3.31)$$

$$D_{FD}\frac{\partial[F_D]}{\partial x} = (1-\alpha)\cdot v[F_D(R)] + \beta\cdot f_S \quad \text{for } x = R, \quad (3.32)$$

$$[F_D] = 0 \quad \text{for } x = 0, \quad (3.33)$$

$$v = v_0 e^{-\frac{f_S}{f_S^0}}, \quad (3.34)$$

$$D_{FD} = D_{FI}\frac{[F_I]}{[F_D]}, \quad (3.35)$$

$$\frac{[F_I][T]}{[FT]} = k, \quad (3.36)$$

$$[F_D] = [F_I] + [FT], \quad (3.37)$$

$$[T]_0(x) = [T]_{bulk}\left(1 - e^{\frac{x-R}{\mu}}\right), \quad (3.38)$$

The boundary conditions at the time t = 0 are:

$$\begin{cases} [F_D](x,0) = F \text{ as implanted profile} & (3.39) \\ [F_C](x,0) = 0 & (3.40) \\ f_S(0) = 0 & (3.41) \\ [F_{inc}] = 0 & (3.42) \end{cases}$$

The variables considered by the model are reported and described in Table 3.2:

Variable	Definition
F_D	the diffusing F in a-Si
F_C	the clustered F in a-Si
FT	the trapped F in a-Si
F_I	the mobile F in a-Si
f_S	the F areal density at the a-c interface
F_{INC}	the F incorporated in c-Si

Table 3.2: *Variables considered by the model.*

The first five equations [Eq. (3.27-3.31)] describe what happens in a-Si and the related incorporation of F in c-Si, in particular the third one describes the F exchanges at the a-c interface. The boundary conditions are represented by the sixth [Eq. (3.32)] and the seventh [Eq. (3.33)] equations. The Eq. (3.34) represents the phenomenological expression of the SPER regrowth rate. The last four equations [Eq. (3.35-3.38)] describe the trap limited diffusion.

The main free, temperature dependent, parameters of the model are reported and described in Table 3.3 (see Sections 3.2.1, 3.2.2 and 3.2.3 for the descriptions of the parameters). We assumed the intrinsic SPER rate, v_0, as a free parameter in order to consider an eventual discrepancy in the annealing temperature with respect to the nominal one.

Parameter	Definition
N_0	clusters concentration
η	cluster dissolution rate
α	segregation factor
β	dissolution rate of f_S
f_S^0	reduction coefficient of v due to f_S
v_0	SPER rate of intrinsic Si
D_{FI}	F_A diffusion in absence of traps
$[T]_{bulk}$	initial concentration of traps
μ	traps capture length of the a-c interface
k	equilibrium constant for F_I-T reaction

Table 3.3: *Parameters of the model.*

3.2.5 The C++ Code

The above system of differential and algebraic equations was solved with an algorithm implemented in an *ad hoc* created ANSI-C CODE. The code was developed autonomously by our group. The code solved the system by a finite difference implementation. The diffusion equations [Eqs.(3.27) and (3.32)] were resolved with a semi-implicit algorithm in the $[F_D]$ variable, while the clustering [Eq. (3.28)] and segregation [Eq. (3.29)] equations (that evolve slowly) were resolved by explicit methods. The space step was kept fixed and equal to 1 nm everywhere except in a 4 nm region near the a-c interface, where it was 0.02 nm. At each iteration the regrowth proceed of 0.02 nm. Therefore the time step results to be inversely proportional to the regrowth velocity ($\Delta t = 0.02/v$). Therefore the space step close to the interface regulate the time step evolution.

The numerical stability and accuracy of the solution was evaluated as a function of the time and space at different temperatures and an overall accuracy better than 0.1% was estimated.

The inputs of the code were all as-implanted F profiles annealed at the same temperature, the times and temperatures of the annealings, the experimental a-c interface positions and F areal density at the a-c interface of each partial regrown profile. Before to simulate the profiles, we excluded the SIMS artefact, present at the sample surface, and we subtracted a

SIMS background signals from them. All SIMS profiles at the same temperature are simulated simultaneously and the model parameters were optimized by a global χ^2.

Due to the reproducibility of the thermal processes, we do not expect an agreement between experimental and simulated a-c interface position better than 10 nm. This unavoidable discrepancy strongly dominate the χ^2 calculation. In other words we realized that the greater component of the χ^2 calculation is due to the interface inaccuracy and therefore a very reduced sensitivity to the clustering, and diffusion parameter is provided by a standard χ^2 definition. Moreover the quality of the model in reproducing the F doses segregated at the interface (that is a crucial parameter due to its correlation with the regrowth rate) is very poorly quantified by a standard χ^2 calculation since the information on that dose is enclosed in few data point at the a-c interface.

Due to the above reasons we decided to define the χ^2 in an unusual way. We calculated the χ^2 comparing point by point the simulation (F_{sim}) and the experimental data (F_{exp}) far from the a-c interface (about 5 nm away), excluding also the first 30 nm that are affected by a SIMS artefact:

$$\chi^2{}_{spectrum} = \frac{\sum_{\forall x - \{ac\}} \frac{\left(F_{sim} - F_{\exp}\right)^2}{\sigma^2}}{N_{po\operatorname{int}s}} \quad (3.43)$$

where {ac} refers to the points of the a-c interface, σ is the error and N_{points} is the number of points considered for the comparison.

Then we evaluated separately the χ^2 due to the interface and dose agreement as:

$$\chi^2{}_{\operatorname{int}erface} = \frac{\left[\frac{\left(R_{th} - R_{\exp}\right)^2}{\sigma_R^2} + \frac{\left(f_{S\,th} - f_{S\exp}\right)^2}{\sigma_{f_S}^2}\right]}{2} \quad (3.44)$$

We obtained an overall figure of merit by a weighted sum of the two above χ^2:

$$\chi^2 = \frac{\left(5 \cdot \chi^2{}_{spctrum} + 2 \cdot \chi^2{}_{\operatorname{int}erface}\right)}{7} \quad (3.45)$$

The weight (unfortunately largely arbitrary) is obtained by considering that, while the interface gives us two hints of information (position and dose), the remaining part of a typical spectrum gives us about 5 hints of information (the close to the surface shape, the diffusion

tail shape, the shape of the zone between the previous two, the incorporation level and the position where the incorporation grows-up).

At a fixed temperature the code, starting from the as implanting profile, simulates the time evolution of all the F components. When time reaches the characteristic time of an experimental profile, χ^2 for that profile is calculated according to (3.45). The procedure is repeated for each experimental time and for each kind of sample at a given temperature. At the end the average χ^2 over all the data of a given temperature is obtained and optimized (hereafter we will refer to it as the "cumulative χ^2") in order to obtain the parameters for that temperature.

We verified or confuted our hypotheses and assumptions checking when the quality of the simulations were improving and/or the cumulative χ^2 was reducing. An unambiguous method to optimize the cumulative χ^2 does not exist because this system of equations is greatly complex and there are a lot of parameters.

We developed a reproducible and reasonable optimization strategy that it is described in the following. First, we optimized all parameters at the same temperature simultaneously. Since the parameters of the F diffusion and incorporation are more sensitive to a perfect correspondence between the experimental and theoretical a-c interface position, we calculated the time corrections necessary to modify the annealing times to match the a-c interface positions with their predictions. Then, we optimized the parameters considering the time corrections and keeping fixed the parameters of the F retardation effect on the SPER rate (f_S^0, v_0 and α). Finally, starting from the obtained minimum of the cumulative χ^2, we optimized the parameters again using as inputs the original annealing times and keeping fixed the parameters of the F diffusion. Finally, we verified the mathematical stability of the obtained results making some perturbations of the minimum of χ^2 for each parameter. The simulations profiles were modified after the complete χ^2 minimization process by including the F segregated at the a-c interface with the SIMS resolution. In Fig. 3.29 an example of a cross-section of χ^2 vs. a model parameter, i.e. f_S^0, is reported as an example. We obtained similar plots for all parameters.

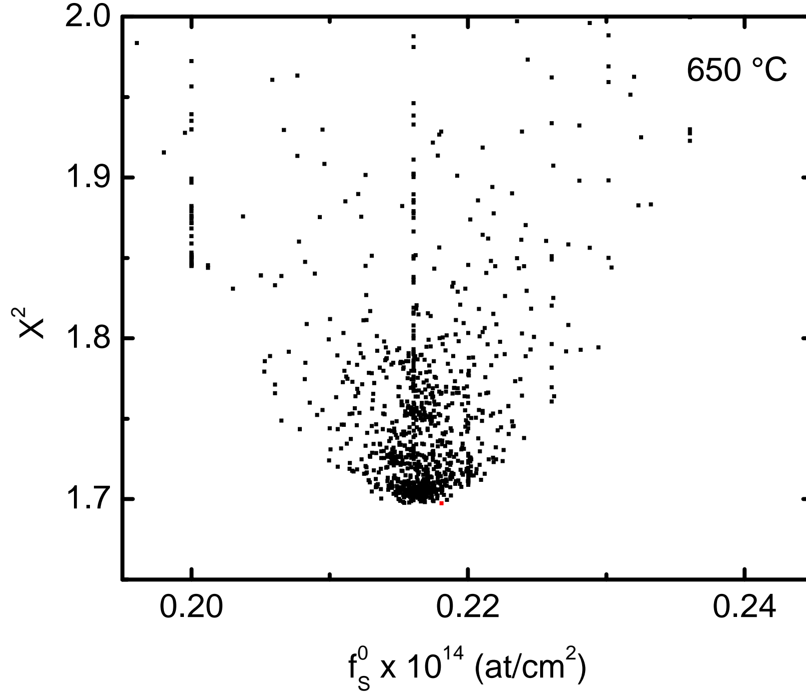

Figure 3.29: *An example of a cross-sectional of χ^2 vs. a model parameter (in this case f_S^0 at 650 °C).*

The errors of the parameters were estimated as the difference between the parameter value at the minimum of χ^2 and the one at $\chi^2 + \Delta\chi^2$; in this work we considered $\chi^2 + \Delta\chi^2$ as

$$X^2 + \Delta X^2 = X^2 \left(1 + \frac{1}{N_{\inf} \cdot N_{prof} - N_{par}} \right) \tag{3.46}$$

where N_{inf}, N_{prof} and N_{par} are the number of information derivable from each profile, the number of the profiles considered at each temperature and the number of the model parameters, respectively.

3.2.6 The simulations results

Figures 3.30-3.39 show all the best profiles (continuous black lines) compared to the SIMS profiles obtained at 580 °C, 650 °C and 700 °C. The SIMS as-implanted profiles, used as input by the code, are represented by dashed lines and the profiles partially or completely regrown are represented by colored continuous lines. The annealing times are reported in the captions of the relative Figures.

580 °C

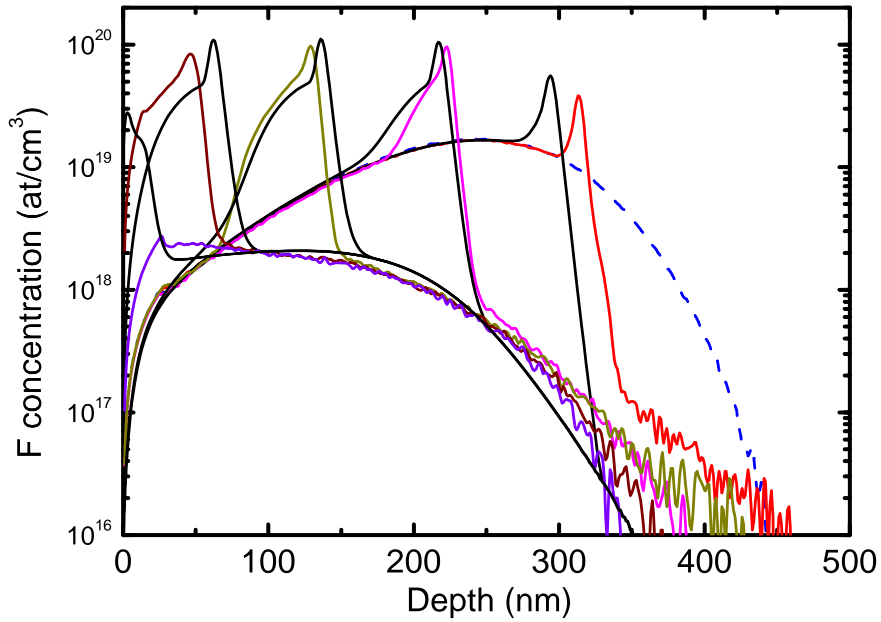

Figure 3.30: *F SIMS profiles just after implantation (blue dotted lines), during and after SPER at 580 °C (colored continuous lines) and best fit results (black continuous lines) for "low concentration A" sample; annealing times: 15, 30, 60 and 90 minutes.*

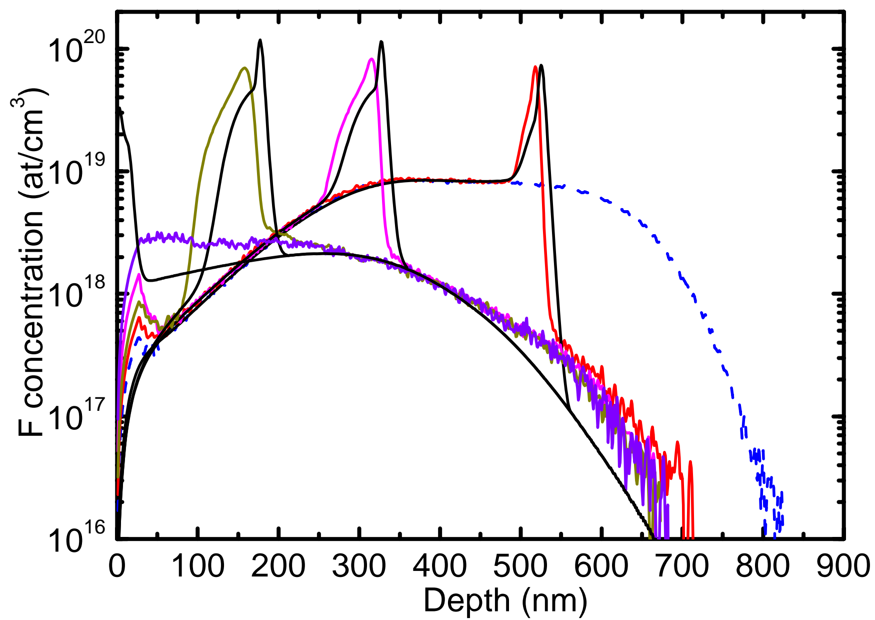

Figure 3.31: *F SIMS profiles just after implantation (blue dotted lines), during and after SPER at 580 °C (colored continuous lines) and best fit results (black continuous lines) for "low concentration B" sample; annealing times:30, 60 and 90 minutes.*

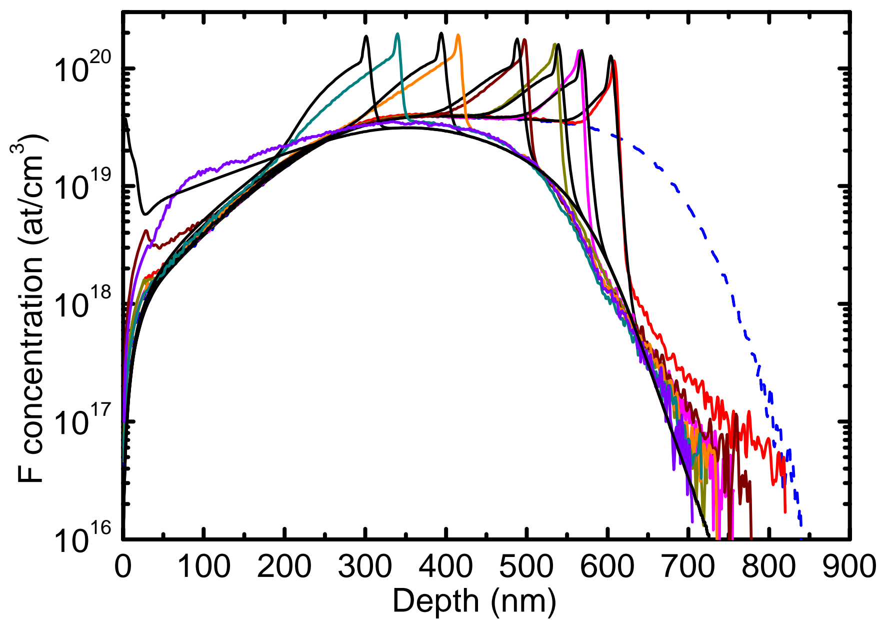

Figure 3.32: *F SIMS profiles just after implantation (blue dotted lines), during and after SPER at 580 °C (colored continuous lines) and best fit results (black continuous lines) for "medium concentration" sample; annealing times: 30, 45, 60, 90, 150, 210 and 510 minutes.*

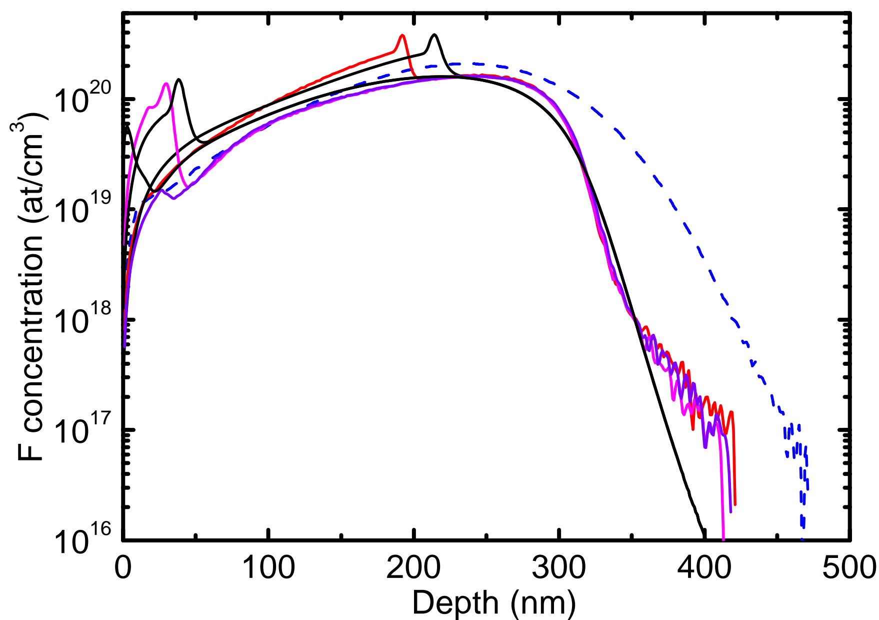

Figure 3.33: *F SIMS profiles just after implantation (blue dotted lines), during and after SPER at 580 °C (colored continuous lines) and best fit results (black continuous lines) for "high concentration A" sample; annealing times: 120, 240 and 480 minutes.*

650 °C

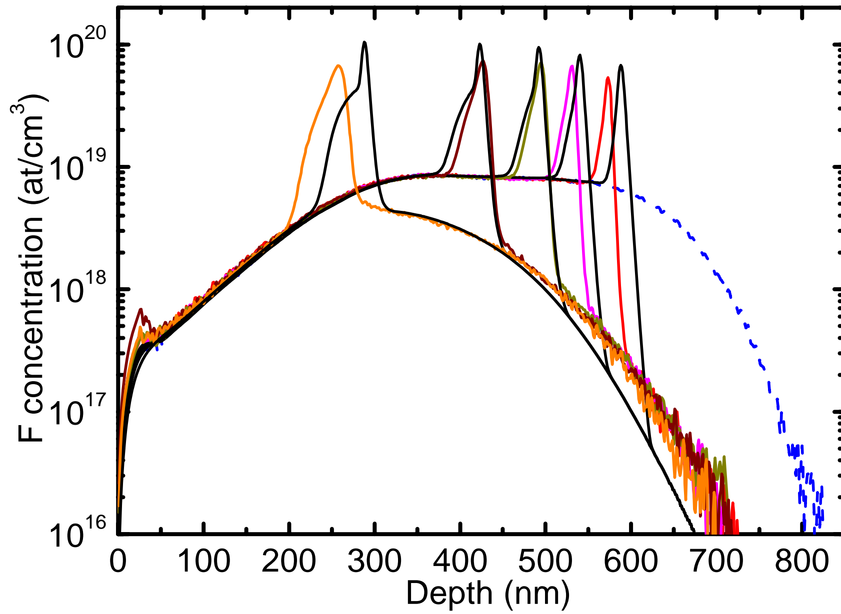

Figure 3.34: *F SIMS profiles just after implantation (blue dotted lines), during and after SPER at 650 °C (colored continuous lines) and best fit results (black continuous lines) for "low concentration B" sample; annealing times: 59, 89, 138, 252, 583 and 1183 s.*

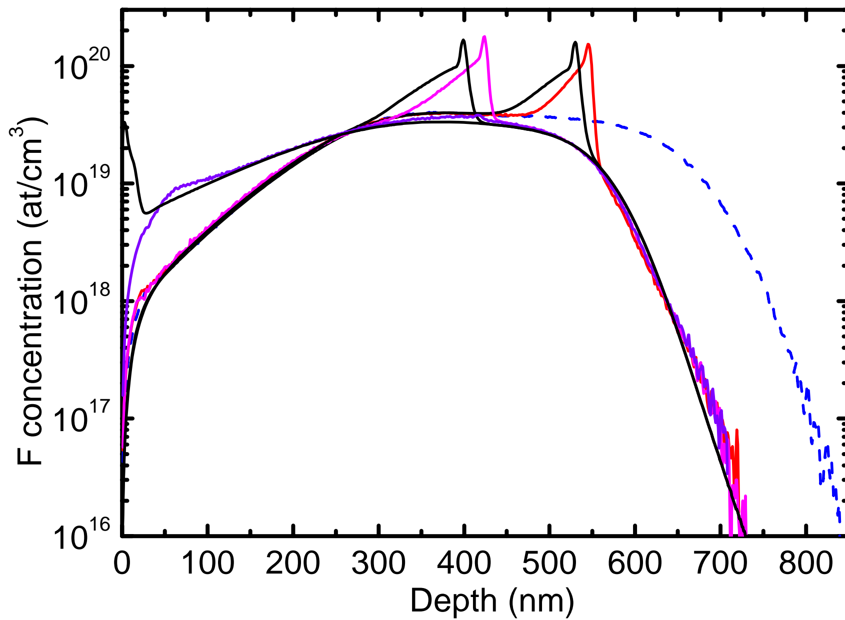

Figure 3.35: *F SIMS profiles just after implantation (blue dotted lines), during and after SPER at 650 °C (colored continuous lines) and best fit results (black continuous lines) for "medium concentration" sample; annealing times: 290, 830 and 2930 s.*

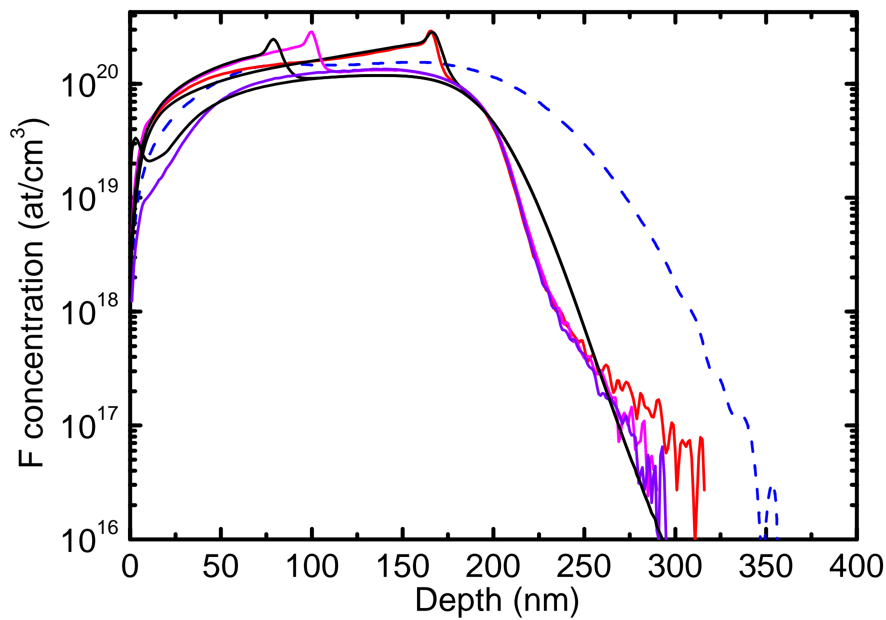

Figure 3.36: *F SIMS profiles just after implantation (blue dotted lines), during and after SPER at 650 °C (colored continuous lines) and best fit results (black continuous lines) for "high concentration B" sample; annealing times: 273, 826 and 1800 s.*

700 °C

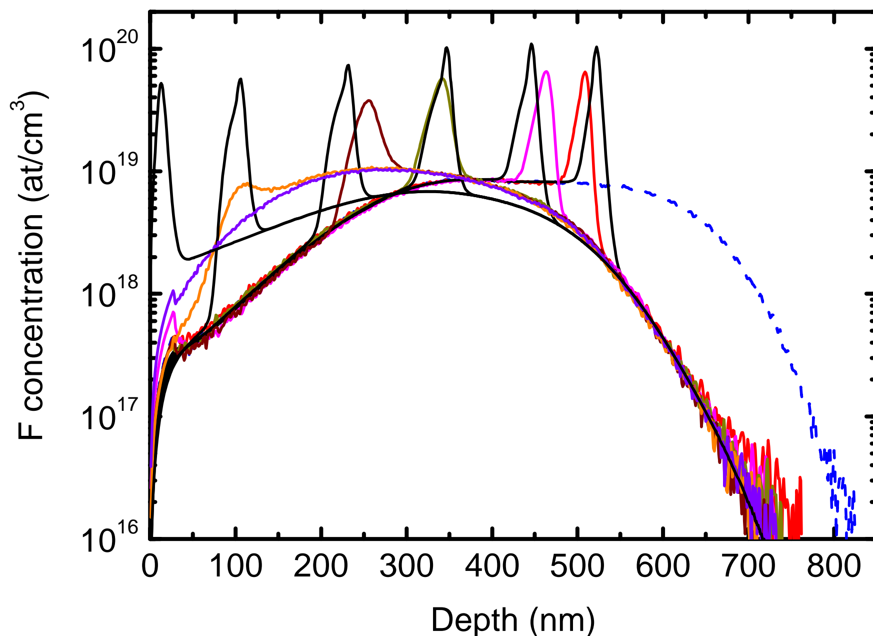

Figure 3.40: *F SIMS profiles just after implantation (blue dotted lines), during and after SPER at 700 °C (colored continuous lines) and best fit results (black continuous lines) for "low concentration B" sample; annealing times: 15, 30, 56, 90, 126 and 150 s.*

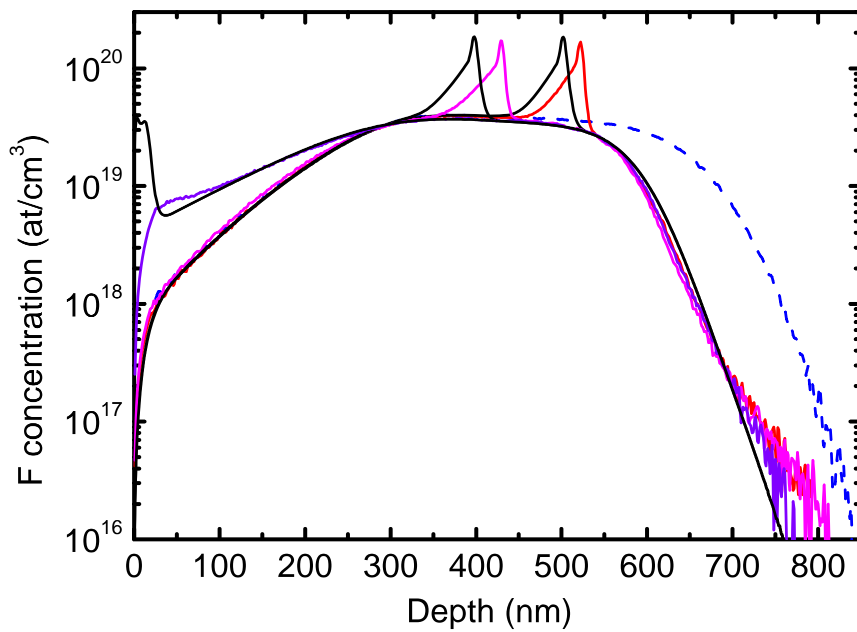

Figure 3.38: *F SIMS profiles just after implantation (blue dotted lines), during and after SPER at 700 °C (colored continuous lines) and best fit results (black continuous lines) for "medium concentration" sample; annealing times: 46, 91 and 350 s.*

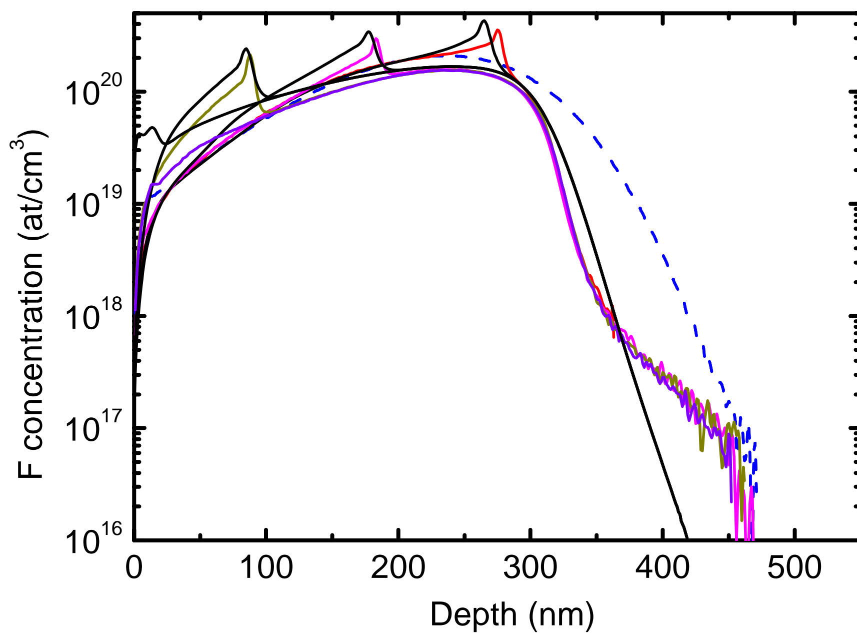

Figure 3.39: *F SIMS profiles just after implantation (blue dotted lines), during and after SPER at 700 °C (colored continuous lines) and best fit results (black continuous lines) for "high concentration A" sample; annealing times: 30, 89 and 146 s.*

All simulated profiles agree very well with the experimental data (Figs. 3.30-3.39) at all temperatures. The sharp F peak segregated at the a-c interface and the diffusing tail in the amorphous bulk are correctly described. The F areal density at the a-c interface is predicted well (see also Figs. 3.22-3.25) and also the a-c interface positions are predicted with an average accuracy of 15 nm (as already discussed in Section 3.2.3, see also Figs. 3.26-3.29). This last prediction is remarkable after considering that it is possible to justify this variability by assuming an error on the process temperatures of 3-4 °C, that is only close to the precision of the temperature of the annealing processes. The simulations reproduce well the F incorporation profiles supporting the fact that it has been necessary and correct to assign to the F clustering in a-Si the role of the phenomenom that describes the hidden variable discussed in Fig. 3.12.

For the first time the F redistribution during Si SPER was reproduced by a mathematical model based on physical observations in a wide range of concentrations and temperatures starting from the as-implanted profile with this high level of details. Before now, the attempts to simulate this system were limited to: reproduce two F profiles after complete regrowth of the same implant [Zographos], or reproduce, with limited success, the features of 4 partial regrown profiles of a single implant, and obtained at a single temperature [Zhang].

Looking at the details of the comparison between SIMS and simulation profiles, the simulations of the F incorporated profiles are not perfectly reproducing the experimental profiles as they slightly underestimate the incorporation. In samples implanted at high concentration the F incorporated is slightly overestimate. Considering the improvement made with respect to the state of the art, the above discrepancy is of minor importance, and it is probably a consequence of the simplified model considered for F clustering.

3.3 DISCUSSION AND INTEPRETATION OF THE RESULTS

The parameters relative to the best fits are reported in Table 3.4 for each of the three annealing temperatures and are discussed in the following.

	580 °C	650 °C	700 °C
D_{FI} (cm^2/s)	$(1.4 \pm 0.2) \times 10^{-14}$	$(1.2 \pm 0.2) \times 10^{-13}$	$(5.5 \pm 0.4) \times 10^{-13}$
T_{bulk} (at/cm^3)	$(6.7 \pm 1.0) \times 10^{19}$	$(8.7 \pm 2.0) \times 10^{19}$	$(1.4 \pm 0.3) \times 10^{20}$
μ (nm)	(84 ± 24)	(141 ± 30)	(169 ± 52)
k (at/cm^3)	$(7.3 \pm 0.5) \times 10^{18}$	$(3.1 \pm 0.5) \times 10^{18}$	$(4.2 \pm 1.6) \times 10^{18}$
α	$(1.3 \pm 0.2) \times 10^{-1}$	$(4.3 \pm 1.0) \times 10^{-2}$	$(3.1 \pm 0.4) \times 10^{-2}$
β (s^{-1})	$(3.6 \pm 0.5) \times 10^{-4}$	$(8.9 \pm 0.5) \times 10^{-4}$	$(9.5 \pm 0.9) \times 10^{-3}$
f_S^0 (at/cm^2)	$(3.0 \pm 0.1) \times 10^{13}$	$(2.2 \pm 0.1) \times 10^{13}$	$(2.5 \pm 0.1) \times 10^{13}$
N_0 (at/cm^3)	$(2.2 \pm 0.1) \times 10^{15}$	$(8.6 \pm 0.9) \times 10^{15}$	$(4.1 \pm 0.2) \times 10^{16}$
η (s^{-1})	$(2.5 \pm 1.8) \times 10^{-5}$	$(4.8 \pm 1.3) \times 10^{-3}$	$(8.4 \pm 0.8) \times 10^{-2}$

Table 3.4: *Table of the model parameters, obtained by the X^2 optimization process.*

3.3.1 The parameters relative to the F diffusion in a-Si

Concerning the diffusion mechanism of F, we reported the diffusivity of mobile F, D_{FI}, in an Arrhenius plot (Fig. 3.40) in order to have an indication of the associated activation energies.

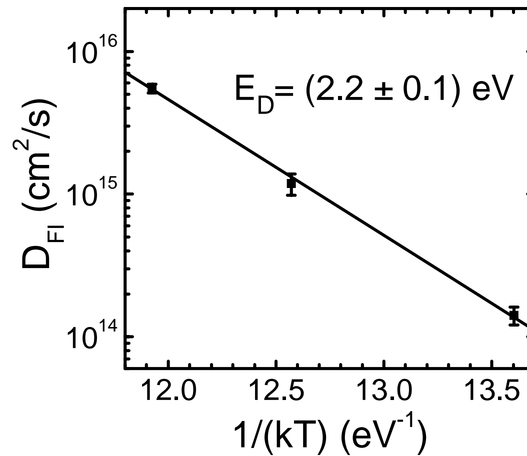

Figure 3.40: *Arrhenius plot of the F the interstitial diffusivity D_{FI}.*

We obtained that the D_{FI} varies with temperature with a pre-factor of 0.13 x 10^{14} cm^2/s and an activation energy of (2.2 ± 0.1) eV (Fig. 3.43). Both of them are very similar to the F diffusion coefficient reported by Nash *et al*. [Nash]: ~0.1 x 10^{14} cm^2/s and (2.2 ± 0.1) eV, respectively. The fact that the values found for the mobile F diffusivity D_{FI} coincides with the F diffusion coefficient measured by Nash *et al*., despite they studied a similar F concentration regime than ours, can be understood within the framework of the present model by considering that the a-Si used in Ref. [Nash] has been produced by deposition, that is a considerably different method with respect to the one used for our samples. Their material might therefore contains a low level of traps for mobile F having no significant influence on the F diffusion.

The other diffusion-related parameters ($[T]_{bulk}$ and μ) do not strongly depend on temperature [Figs. 3.41 and 3.42].

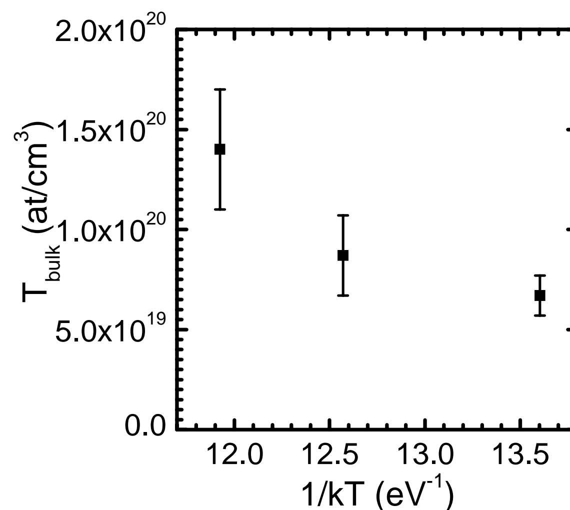

Figure 3.41: *Arrhenius plot of the background trap density, $[T]_{bulk}$.*

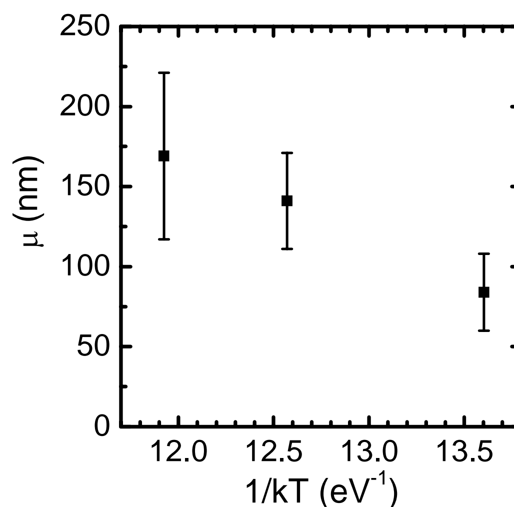

Figure 3.42: *Arrhenius plot of the traps capture length of the a-c interface, μ.*

The background trap density is ~ 10^{20} at/cm^3, suggesting that these traps might be amorphous bulk defects, whose density is known to be at most 1% at. [Coffa, Bernstein]. The traps capture length of the a-c interface is relatively constant and equal to ~ 150 nm. The relatively constant trends (compared to the two orders of magnitude of variation observed for D_{FI}) of $[T]_{bulk}$ and μ suggested that these parameters depend on the intrinsic properties of the amorphous phase. In fact all amorphous silicon substrates used in this work were created with the same process (ion implantation of Si ions) and implanted with F at the fixed temperature of 77 K, avoiding the variability due to the creation process. The capture length could represent the balance between defects diffusion in a-Si, the defects trapping by the a-c interface and the SPER process. A capture length constant could indicate that the efficacy of the trapping is constant and infinite, and defects diffusion and SPER increase with increasing temperature at the same way.

The equilibrium constant for trapping reaction (k) is ~ 5 x 10^{18} at/cm^3 almost independent of temperature. When F concentration is more less than traps concentration, the trapping reaction [Eq. (3.12)] is heavily unbalanced in the formation of FT complexes. Instead, when the F concentration exceeds the trap concentration, the traps are easily saturated so F atoms can diffuse for a long distance causing the extended diffusive tails observed in our simulations.

3.3.2 The parameters relative to the F segregation at the a-c interface

As outlined above, the F segregation at the interface phase has a central role within the whole phenomenon. We found that by increasing the temperature the segregation factor α decreases, while the releasing factor β increases by more than an order of magnitude (Fig. 3.43).

We estimated activation energies of α and β to be respectively (-0.8 ± 0.1) eV and (2.0 ± 1.1) eV. The negative value found for E_α indicates that the barrier seen by an F atom close to the a-c interface for 'jumping' into the interface phase is lower by (0.8 ± 0.1) eV than the barrier for diffusing back towards the amorphous phase. The positive value found for E_β indicates instead that there is a barrier of (2.0 ± 1.1) eV for the release of the F atoms from the interface phase toward the amorphous phase, which is in agreement with the calculated binding energy of F to a dangling bond that is ~2 eV [Fiorentini06, Diebel06].

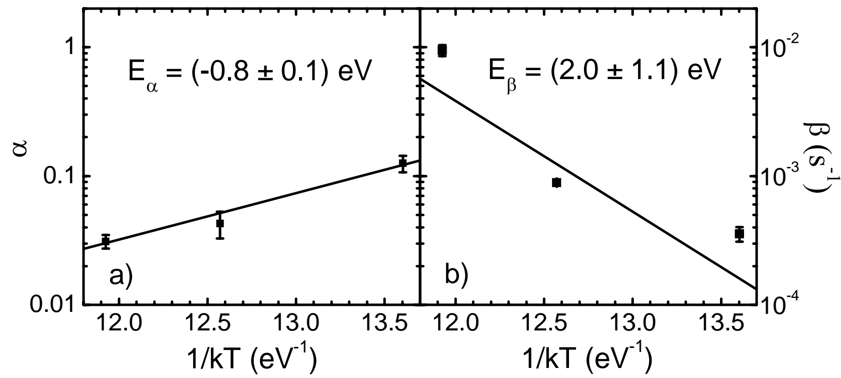

Figure 3.43: **(a)** *Arrhenius plot of the segregation factor, α.;***(b)** *Arrhenius plot of the releasing factor, β.*

These values, together with the energy barrier discussed above for the F interstitial diffusivity, allow to draw the energy scheme reported in Fig. 3.44 describing the F diffusion in a-Si and its exchange between the amorphous phase and interface layer. We reported in Fig. 3.44 also an energetic barrier to represent the transition of the F atom from a-Si to c-Si. Since we did not improve the simulations considering a direct incorporation channel for F in our model, we estimated that this energetic barrier would be high.

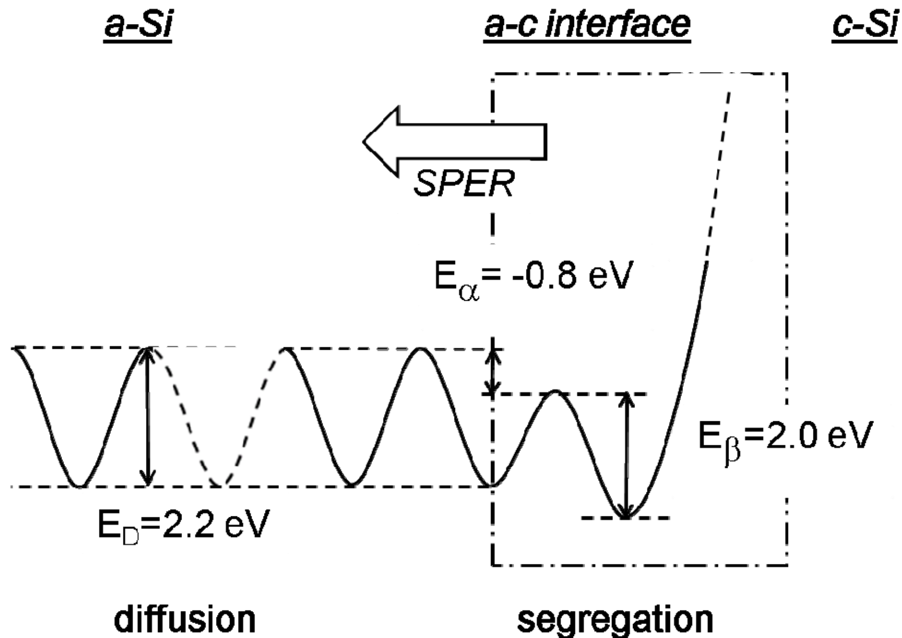

Figure 3.44: *Energy scheme for the F evolution in pre-amorphized Si during SPER close to the a-c interface. The involved mechanisms are represented by their energy barriers: E_D for the F diffusion in a-Si, E_α for the F segregation at the a-c interface phase and E_β for the release of F release from the a-c interface phase to bulk a-Si.*

3.3.3 The parameters relative to the F retardation effect on the SPER rate

The segregation mechanism governs also the retardation effect of F on the SPER rate, through the exponential law [Eq. (3.2)] that can be obtained directly from the experimental data (Fig. 3.13). Consistently, the model allows to predict accurately the position of the a-c assuming the above exponential dependence. The values of v_0 used in the simulations are in agreement with literature values [Olson], assuming an error on the process temperatures of 3-4 °C eventually. We kept f_S^0 as a free parameter because we wanted to test our hypothesis about SPER rate in presence of F and to be more sensible to its real values. In Table 3.5 we show the comparison between the parameters f_S^0 directly deduced by the experimental data (Fig. 3.13) and the values extracted by the model simulation optimization.

Temperature	Experimental f_S^0 (at/cm^2)	Simulated f_S^0 (at/cm^2)
580 °C	$(3.3 \pm 0.1) \times 10^{13}$	$(3.0 \pm 0.1) \times 10^{13}$
650 °C	$(2.0 \pm 0.1) \times 10^{13}$	$(2.2 \pm 0.1) \times 10^{13}$
700 °C	$(3.0 \pm 0.1) \times 10^{13}$	$(2.5 \pm 0.1) \times 10^{13}$

Table 3.5: *Comparison between experimental and simulated values of f_S^0.*

The obtained f_S^0 best fit parameters are very close to the values extracted directly by the experimental data. The set extracted by the simulations does not follow a linear trend with temperature, confirming our experimental observations (see Table 3.1).

The above exponential dependence is remarkable and allows the interpretation described as follows.

There are experimental evidences reported in literature [Rudawski08, Aziz] that the SPER rate v has an exponential dependence on the stress state, σ_{ij}, through the relation

$$v = v_0 \exp\left(\frac{\Delta V_{ij}^{*} \sigma_{ij}}{kT}\right), \qquad (3.47)$$

where v_0 is the stress-free velocity, kT has the usual meaning, *i* and *j* refer to axes in the coordinate frame of Ref. [Aziz], and ΔV_{ij}^{*} represents the activation volume tensor. If we make the hypothesis that the segregated F produces a local stress (and consequently a strain) at the

a-c interface, and that this stress is reasonably proportional to the amount of segregated F through the relation

$$\sigma_{ij} = p_{ij} f_S, \tag{3.48}$$

where p_{ij} is a tensor of forces, we simply obtain:

$$v = v_0 \exp\left(\frac{\Delta V_{ij}^* p_{ij}}{kT} f_S \right). \tag{3.49}$$

The last equation is analytically identical to Eq. (3.2) that was

$$v = v_0 \exp\left(-\frac{f_S}{f_S^0} \right) \tag{3.50}$$

allowing an interpretation of the exponential retardation of the SPER rate in terms of stress related retardation induced by the F in the interface layer. Moreover, by comparing the Eq. (3.49) to Eq. (3.50) we get:

$$\frac{f_S^0}{kT} = -\frac{1}{\Delta V_{ij}^* p_{ij}} . \tag{3.51}$$

As a consequence, the parameter f_S^0 divided by kT should be constant as a function of the temperature. This is what indeed happens as evidenced in Table 3.6, supporting the validity of the above interpretation.

	580 °C	650 °C	700 °C
$\frac{f_S^0}{kT}$ (eV^{-1} cm^{-2})	$(4.1 \pm 0.5) \times 10^{14}$	$(2.7 \pm 0.5) \times 10^{14}$	$(3.0 \pm 0.5) \times 10^{14}$

Table 3.6: *Values* $\frac{f_S^0}{kT}$ *are reported.*

The values at the three temperatures are compatible within 2 σ considering their errors, that were calculated considering the errors of f_S^0 (reported in Table 3.2) and an error of 3 °C for the temperature.

Further considerations can be made about the tensor p_{ij}. The epitaxial constraint imposes that the strain due to F builds up along the direction perpendicular to the a-c interface, and the value of ΔV along this direction reported in literature is negative [Rudawski08]. Therefore, according to Eq. (3.51), the tensor p_{ij} along the same direction has

to be positive, i.e. in order to explain the observed SPER rate reduction F should induce a dilatation of the crystal Si lattice perpendicular to the a-c interface. In order to verify the above conclusion we measured the strain profiles near the a-c interface of an intrinsic Si sample and a F implanted “high concentration B” partially regrown. In Fig. 3.45 their perpendicular strain profiles near the a-c interface are shown in the first 10 nm of the depth axis. The strain of the EOR region are also reported (more than 300 nm).

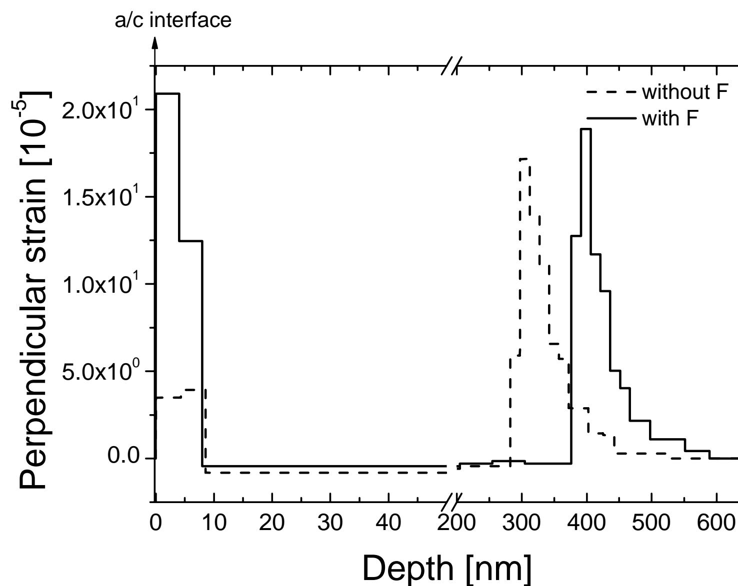

Figure 3.45: *Strain profiles near the a-c interface in Si sample with o without F implanted. For the sake of clarity the a-c interfaces of both samples were aligned after partial SPER.*

In presence of F the perpendicular strain occurs and it is quite substantial respect to the one of the intrinsic sample. Strain depth profiling by high resolution x-ray diffraction measurements of selected samples have confirmed that in presence of F there is a dilatation of the lattice parameter close to the a-c interface along a direction perpendicular to it. This is a further confirmation of the above interpretation of a stress related SPER reduction induced by F.

3.3.4 The parameters relative to the F clustering in a-Si

Our model simulates well the F incorporation (Figs. 3.30 - 3.39). This fact affirms that also the F clustering is modelled satisfactorily enough to account quantitatively for the F incorporation. In the following a comparison with TEM measurements is performed in order to check the model predictivity. In the Fig. 1.30 of the first Chapter we reported a SIMS partially regrown profile at 700 °C for 25 s. In this profile F-induced nano-bubbles were

observed by TEM measurements [Boninelli08]. The average distance between bubbles could be estimated ~ 30 nm, observing the plan view images reported in Ref. [Boninelli08]. The main radius of the bubbles was estimated by authors to be ~ 1.5 nm in the sample region with the high F concentration. In a previous work of the same authors [Boninelli06], we remind that they found a diameter distribution of the bubbles density (Fig. 1.29 of the Chapter 1). By crossing SIMS and TEM measurements, the authors also stated that such bubbles are cavities enriched with F and they assumed that their samples contain bubbles with a diameter lower than 0.5 nm, even if they the are not sensitive to observe them by TEM. Estimating the F quantity in each type of clusters, the great amount of F atoms should be contained in the little cavities.

In order to realize a direct comparison between the radius of the clusters and their reciprocal distance measured by TEM measurements and valued by our model, we tried to simulate the F profiles shown in Fig. 1.30 (red line) of the Ref. [Boninelli08]. The result is shown in Fig. 3.46. We reported also the completely regrown profile and its simulation as references. The simulations are represented by black lines.

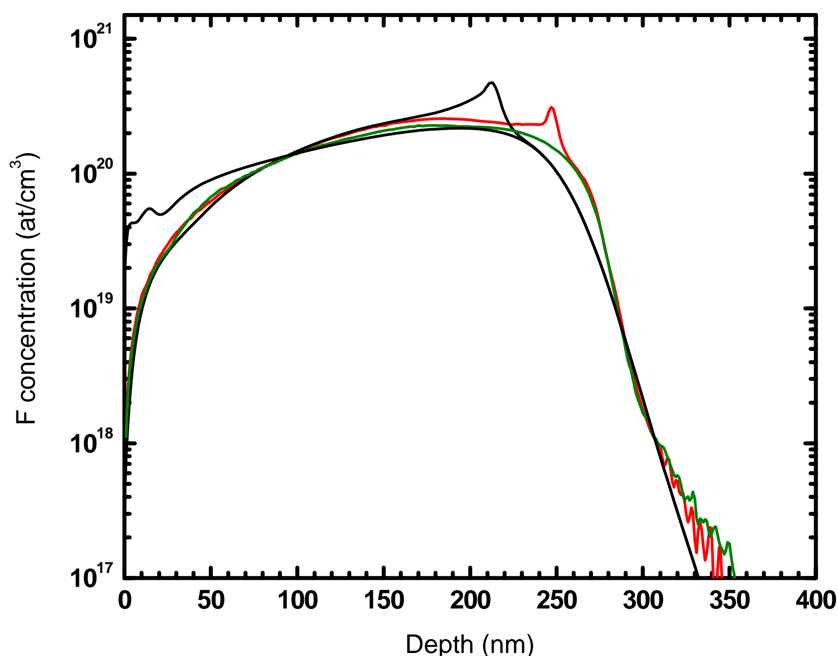

Figure 3.46: *F SIMS profiles after a partial SPER at 700 °C for 25 s (red line) and after a complete SPER at 700 °C(green line). The data are taken from Ref. [Boninelli08]. Our simulations are represented by black lines.*

Initially we tried to simulate Boninelli *et al.*'s F profiles using the parameters optimized with our model at 700 °C. We observed that our simulations were underestimating the F diffusion in a-Si with these parameters. So, we increased the F diffusivity parameter with the aim to fit better the F profiles, assuming a higher temperature of the annealing than the nominal one as a consequence. Considering also that the Rapid Thermal Processor used in Ref. [Boninelli08] is different from ours, it could be correct to assume a discrepancy in the temperature. So, we simulated Boninelli *et al.*'s profiles using the parameters extrapolated at 715 °C. The F incorporation profiles are reproduced well and with the same degree of accuracy obtained in our samples annealed at 700 °C.

Using the model parameters is possible to predict the average distance between clusters, d_{cl}, in the a-Si bulk by Eq. (3.52):

$$d_{cl} = \left(\frac{1}{[N_0]} \right)^{1/3}, \tag{3.52}$$

and the greatest radius in correspondence of the maximum peak of F clustered, δ_{max}, for each sample, using Eq. (3.53):

$$\delta_{\max} = a_0 + \left(\frac{3}{4\pi\rho} \frac{[F_C^{\max}]}{[N_0]} \right)^{1/3}, \tag{3.53}$$

We remind that our model considers only one class of clusters with the same radius for simplicity.

In Table 3.7 we compare the values of d_{cl} and the cluster radius, δ, measured by TEM and obtained by model parameters.

	TEM	Model
d_{cl}	~ 30 nm	25.6 nm
δ	~ 1.5 nm (average value)	3.4 nm (maximum value)

Table 3.7: *The average distance in a-Si and the cluster radius of the F profile annealed at 700 °C for 25 s as estimated by TEM measurement [Boninelli08] and by our model.*

While the values of the average distance between clusters are very similar, the values of the cluster radius have the same order of magnitude even if a factor of 2.2 exists between them. These results confirm the goodness of the clustering model since the values extracted by the

model are close to TEM values at least in the order of magnitude. This is the first time that a predictive model of the F clustering in a-Si is able to do that. Because of its simplicity, the model is not able to predict correctly the TEM observation in details, because it predicts that F is contained in big clusters and this forecast is in conflict with the picture obtained by TEM analysis, in which the most part of F atoms are contained in small clusters. Our model foresees an excessive clusters growth since, having assuming only a class of clusters, the model prefers to accommodate all F atoms in few big clusters instead of in many small ones. This limit could be overcome assuming a class of small clusters additionally in the model but this would be beyond the sensitivity of the experimental procedure used in this work.

Deepening more the physical analysis of the clustering parameters, it could be interesting to observe how our model predicts the clusters evolution with the temperature. In Tables 3.8 and 3.9 the values of d_{cl} and δ_{max} extracted by the model parameters at each temperature and in each sample reported.

Temperature	d_{cl} (nm)
580 °C	77
650 °C	49
700 °C	29

Table 3.8: *The average distance in a-Si are reported by each sample as estimated by our model.*

Temperature	Name sample	δ_{max} (nm)
580 °C	Low dose A	2.2
580 °C	Low dose B	2.3
580 °C	Medium dose	5.3
580 °C	High dose A	9.0
650 °C	Low dose B	1.9
650 °C	Medium dose	3.6
650 °C	High dose B	6.2
700 °C	Low dose B	1.4
700 °C	Medium dose	2.2
700 °C	High dose A	3.6

Table 3.9: *The maximus radius of the greatest clusters in a-Si are reported by each sample as estimated by our model.*

Analyzing the values reported in Tables 3.8 and 3.9, we observe that the average distance between clusters in a-Si diminishes with temperature, while the maximum radius increases with F clustered concentration obviously, but it diminishes with temperature at fixed F concentration. We performed TEM analysis on the "medium concentration" sample partially annealed for 290 s at 650°C without observing any clusters. We remind that in the same sample the signal of SiF_4 molecule was observed by XAS analysis (Section 3.1.3), confirming the F is contained in bubbles in this sample. Unfortunately, this TEM result supports the idea that our clustering model is again perfectible because it fails also to predict the clusters evolution with the temperature. So, a more complex description of clustering than the one adopted would be necessary to match itself perfectly with all experimental observations, even if it is undeniable that our interpretation of the F clustering in a-Si represents an important and fundamental progress with respect to the state of the art. In the next future our efforts will be used to improve the microscopical aspects of the clustering model.

Due to the above considerations, we did not any other discussion on the values found for $[N_0]$.

Different considerations might hold concerning the cluster dissolution process. In fact, the cluster dissolution probability η changes with temperature with an activation energy of (4.7 ± 0.2) eV (Fig. 3.47).

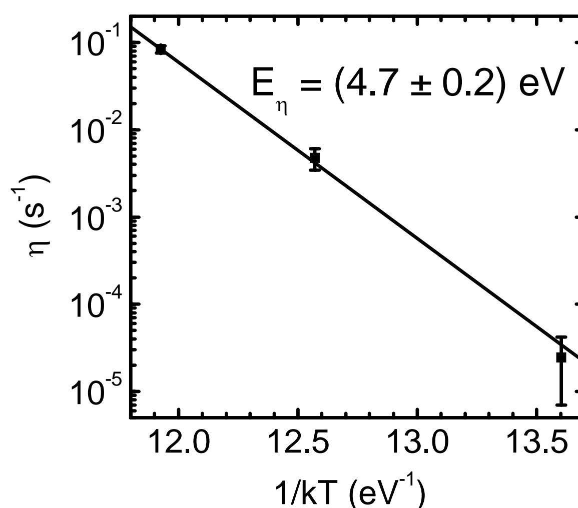

Figure 3.47: *Arrhenius plot for the cluster dissolution probability η.*

This considerably high value is remarkable and is not too far from the Si-F bond energy of 5.73 eV [Lide]. This suggests that, even if the real cluster evolution is certainly much more complex than one considered by the present model, the dissolution process is governed by a

single simple phenomenon, satisfactorily described by the model, that presumably is the destruction of the Si-F bond in the SiF_4 molecules.

Conclusion

In this thesis the evolution and incorporation of F implanted in a-Si during SPER were investigated and modeled showing that they occur through different complex and correlated phenomena.

We started our research from an intense and accurate experimental analysis with the aim to investigate and characterize the entire F redistribution during Si SPER. We designed various samples characterized by two different amorphous depth and implanted with F in a wide range of concentration. The samples were annealed at three temperatures (580C °C, 650 °C and 700 °C) with the aim to induce partial or complete regrowth of the amorphous layers. The F chemical profiles in concentration of all samples were analyzed by SIMS measurements. In order to understand better the element specific structural of the F incorporated in crystalline, a specific X-ray absorption spectroscopy analysis was performed.

We demonstrated that F segregates in amorphous Si during SPER by splitting in three states: a diffusive state and a clustered one in a-Si, and an interface segregated state evidenced by the presence of a F accumulation peak at the amorphous-crystal interface. We discovered that the reduction of the SPER rate in the presence of F is governed only by the F areal density at the a-c interface following a simple exponential decay. We have shown experimentally that a positive strain perpendicular to the a-c interface is present and it is induced by F, and such strain is responsible for the above SPER rate reduction by slowing the migration of the ledges responsible for the regrowth. In particular our description of the F retardation effect on the SPER is compatible with the more actual and accepted SPER model proposed in literature. The dynamics of the areal density of F segregated at the a-c interface can be well described by a sticking-release model and the analysis of the related parameters allowed to fix the energy scheme of F close to the interface. This dynamics together with the exponential relation mentioned above allows to predict well the SPER velocity. Different models describing the F diffusion in the amorphous phase were tried, such as constant diffusion, concentration dependent diffusion etc.. The most satisfactory and reasonable model assumes that F diffusion in a-Si is described by a trap-limited mechanism: the defects in amorphous bulk act as traps for F interstitials and only the non-trapped fraction of F can

diffuse. The clustering of F in the amorphous phase was described by considering all experimental observations presented in literature and discovered by our XAS analysis. This last one demonstrated that F is incorporated in c-Si in the form of SiF_4 molecules. The comprehensive picture, proposed by us, affirms that the SiF_4 molecules form already in a-Si and they are induced to accommodate in the amorphous matrix by the formation of nano-bubbles. The SiF_4-filled nano-bubbles are transferred from the amorphous bulk to the crystal phase by the passage of the a-c interface, as confirmed by recent TEM and our XAS observations. These bubbles are then able to intercept in c-Si the Is flux from the EOR defects towards the sample surface during post SPER annealings, acting as sink for the Is, avoiding B TED and the B clusters formation.

We described all these physical processes for the first time in a single overall model able to simulate the evolution of F chemical profiles in a wide range of concentrations and annealing temperatures. The quality of the simulations obtained using our model confirmed the experimental evidences and the above considerations. This model is an important and significant progress of the state of the art because it has deepened the knowledge of the microscopical mechanisms of the impurity diffusion in a-Si and the SPER. It demonstrated how it is necessary to consider F clustering in a-Si in the description of F incorporation in c-Si, even if our clustering model is again improvable because it does not describe all experimental microscopical observations in details. However, the model developed in this thesis is a very powerful tool to predict in details the F redistribution and incorporation during SPER of pre-amorphized Si. It could be used to determine the initial conditions of the F-V clusters evolution in c-Si during post-SPER annealings, giving more information about F structure and distribution in c-Si. Our work might improve the use of F implants in the point defect engineering if our model will be implement in the common industrial processes for the fabrication of advanced USJs.

Our modeling approach could be useful also in other similar systems in which redistribution of impurities during phase transition of the substrate occurs (e.g. H in Si or F in Ge during SPER), in particular in the understanding of the microscopical retardation effects of inactive impurities on the Si SPER.

Currently, we are trying to model and simulate the H redistribution during Si SPER in a new recent collaboration with B. C. Johnson of the University of Melbourne (Australia). More details will be given in the Appendix of this thesis.

Appendix

H SEGREGATION AND REDISTRIBUTION DURING SPER OF PRE-AMORPHIZED SILICON

In the last years, a great interest is developed about the effects of non doping impurities on the SPER rate, such as F, as we have discussed previously (Section 3.3), with the aim to consider them in the design and fabrication of the future USJs. Beyond F, H is another non-doping impurity that has been studied a lot. H is often present as impurity in the silicon matrix or is introduced whenever there is water vapor in the ambient or a surface oxide. So, it is very important to understand and model correctly the behavior of H during Si SPER with the aim to improve the control on H infiltration.

Recently, following discussions I had at the past E-MRS 2009 spring meeting, I have promoted a collaboration between our research group and the group of B. C. Johnson from School of Physics of the University of Melbourne (Australia) is starting with the goal to create a model able to predict the evolution of the chemical profile of H during Si SPER from the as-implanted one. The strategy consists in reproducing the experimental and theoretical approach used by us in the study of F redistribution and incorporation during Si SPER, reported extensively in this thesis, transferring it to the “H-system”.

A. 1 The experimental SIMS profiles

As a first step, we tried to model and simulate a single set of data presented by Roth *et al.* [Roth92] in which H diffused in a buried amorphous Si (a-Si) layer from the sample surface at 606 °C.

Amorphous Si films up to 5 μm thick were realized by ion implantation of Si into float-zone Si (100) wafers. Samples were annealed in air at temperature of 606 °C. The SPER rate was determined as a function of interface depth by time-resolved reflectivity measurements at 6328 Å. Secondary ion mass spectrometry with Cs primary ion beam was used to determine the distribution of H in samples partially SPER regrown.

In Fig. A.1, the measured SIMS profiles published in Ref. [Roth92] are shown.

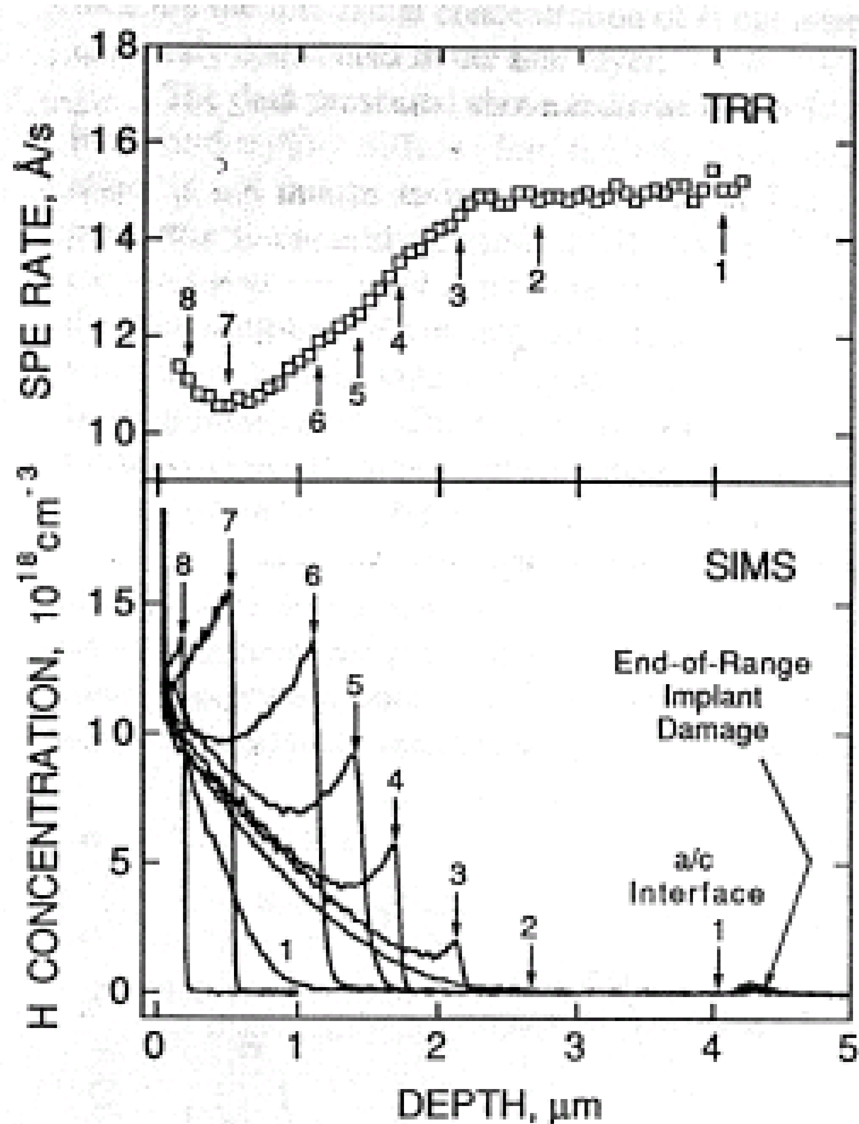

Figure A.1: **(a)** *upper panel: SPER rate as a function of the a-c interface depth for a 4.2 µm thick a-Si layer annealed in air at 606 °C;* **(b)** *lower panel: H SIMS profiles measured after annealing in air for times corresponding to the numbered arrows shown in the upper panel [Roth92].*

During thermal annealings H diffuses from the sample surface into the layer. It is evident in Fig. A.1 that H segregates strongly in the amorphous phase once H meets the amorphous-crystal (a-c) interface (from the peak number 3 forward). The H segregated peak increases while the a-c interface advances without showing any saturation effect in this sample. The H profile in c-Si is almost absent because H diffuses very fast in c-Si and its diffusion profiles fall quickly below the SIMS detection limit. Part of the H diffusion in c-Si is and is captured by EOR defects (see the hump at ~ 4.3 µm).

Before to explain our hypothesis about the H behavior and propose our model, it is useful to remind what it is known about H in a-Si in literature.

A.2 REVIEW ON THE H BEHAVIOR IN A-SI

A.2.1 H diffusion in a-Si

Roth *et al.* [Roth93] obtained evidences that H diffusion in a-Si is thermally activated and for low H concentrations (< 2 x 10^{19} at/cm^3) in the range from 450 °C to 700 °C is described by:

$$D = D_0 \cdot \exp(-E_a / kT) \tag{A.1}$$

with a pre-exponential factor D_0 = 2.2 x 10^4 cm^2/s and an activation energy E_a = 2.7 eV.
They proposed that the observed transport of H occurs through a process of bond switching, mediated by the presence of mobile dangling bonds.

A.2.2 H effect on the SPER rate

Unifying the results obtained about the H effect on the SPER rate at low H concentration [Roth93] and high concentration [Johnson09], a linear reduction of the velocity until ~ 50% of the intrinsic value exists in the H concentration range up to [H] ~ 3 x 10^{19} at/cm^3 (Fig. A.2). Above H concentration of 3 x 10^{19} at/cm^3, the SPER rate has a weak dependence on H concentration and continues to decrease to 20% of the intrinsic value until the H concentration of 2.3 x 10^{20} at/cm^3.

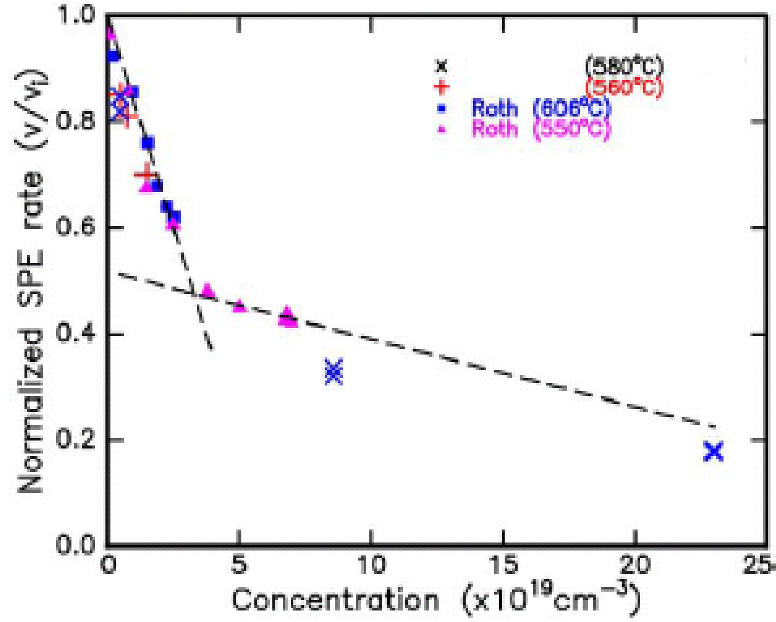

Figure A.2: *The dependence of the SPER rate on the H concentration determined from [OlsonHB] and [Johnson09].*

The parameters of the linear fits are:

for 0 < [H] < 3 x 10^{19} at/cm^3
$$\frac{v}{v_0} = -1.65 \cdot 10^{-20} \frac{at}{cm^3} \cdot [H] + 1 \qquad \text{(A.2)}$$

for 3 x 10^{19} at/cm^3 < [H]
$$\frac{v}{v_0} = -1.28 \cdot 10^{-21} \frac{at}{cm^3} \cdot [H] + 0.518 \qquad \text{(A.3)}$$

The more accepted model of the H effect on the SPER affirms that H retards SPER through the passivation of dangling bonds at the a-c interface thus reducing the number of crystallization sites available [OlsonHB, Oberlin]. The presence of H reduces only the pre-exponential factor of the SPER rate and not the SPER activation energy [Johnson09, *and references therein*].

A.2.3 H segregation at the a-c interface

As shown in Fig. A.1, H segregates in the amorphous side of the a-c interface. Actually, the segregation coefficient has not been determined for H in a-Si. Recently Johnson *et al.* [Johnson09] has suggested that H has a temperature dependent segregation coefficient k of less than one.

A.3 THE MODEL OF THE "H SYSTEM"

With the aim to simulate the data reported in Fig. A.1, first we determined the SPER annealing times as the integral over depth of the inverse of the velocity reported in Fig. A.1 (above panel) using numerical method.

Then we developed an appropriate model considering the above experimental evidences and using a reduced version of the C++ code employed for our study of the "F-system".

The considered quantities are:

- H(x,t) = H: the H concentration in a-Si;
- h = the H total dose injected in the crystal = H · Δx, where Δx would be a fixed value of some nanometers.

The complete model is:

At the sample surface: $$H(0,t) = H_0 \quad \text{(A.4)}$$

In the a-Si bulk: $$\frac{\partial H}{\partial t} = \frac{\partial}{\partial x} D_H \frac{\partial H}{\partial x} \quad \text{(A.5)}$$

At the a/c interface: $$D_H \frac{\partial H}{\partial x} = (1-\alpha) \cdot v \cdot H \quad \text{(A.6)}$$

$$\frac{\partial h}{\partial t} = \alpha \cdot v \cdot H \quad \text{(A.7)}$$

$$v = v_0 \left(1 - v_{lin} H^{a/c}\right) \quad \text{(A.8)}$$

Eq. (A.4) describes the source of the H at the surface, as shown in Fig. A.1 (lower panel), and we fixed H_0 at 1.15 x 10^{19} at/cm^3 for all simulations. The H diffusion in a-Si is described by Eq. (A.5) and we are able to consider a constant diffusion as well as a trap limited diffusion, changing only the D_H definition in the code. Differently from F, H segregates at the a-c interface but no segregated peak appears. In this case we hypothesized that h is equal to the dose injected in crystal and some part of it is captured by EOR defects (Fig. A.1). The H segregation at the a-c interface and the H dose injected in c-Si are described by Eq. (A.6) and Eq. (A.7). In this way we do not have to describe H diffusion in c-Si and introduce other equations and parameters, but we can deduce α correctly. The SPER rate is regulated by Eq.

(A.8) and it is based on the experimentally observations. Since the maximum H concentration achieved in the profiles of Fig. A.1 does not exceed 3 x 10^{19} at/cm^3, we considered the phenomenological relationship between SPER rate and H concentration at the a-c interface ($H^{a/c}$) in the low concentration regime. The model parameters are:

- H_0 = H(0,t) = fixed at 1.15 x 10^{19} at./cm^3 from the observation of Fig. A.1;
- α = injection coefficient;
- v_0 = intrinsic SPER rate;
- v_{lin} = linear reduction factor of SPER rate;
- D_H = the H diffusion coefficient.

In this preliminary study, we compared a constant diffusion, suggested by Roth *et al.* [Roth92, Roth93], with a trap limited diffusion. Considering that H passivates dangling bonds, we supposed that also H diffusion in a-Si could be influenced by a reaction between H and traps of the amorphous bulk, similar to what happens for F (Chapter 3.2.1 of this thesis):

$$[H_I]+[T]\leftrightarrow[HT] \tag{A.9}$$

These defects could be easily dangling bonds. In the case of the trap limited diffusion, it is necessary to consider in the model also the Eqs. (A.10 – A.13), discussed in details in Section 3.2.1 of this thesis and still valid changing F with H:

$$[T]_0(x)=[T]_{bulk}\left(1-e^{\frac{x-R}{\mu}}\right), \tag{A.10}$$

$$\frac{[H][T]}{[HT]}=k\ , \tag{A.11}$$

$$D_{HD}=D_{HI}\frac{[H_I]}{[H_D]}, \tag{A.12}$$

$$[H_D]=[H_I]+[HT]. \tag{A.13}$$

In this case D_{HI}, k, $[T]_{bulk}$ and μ will be also considered as parameters of the model.

A.4 SIMULATIONS RESULTS

As we did for the "F system", we optimized our model parameters obtaining finally the best fit profiles shown in Fig. A.3 in the case of a constant diffusion.

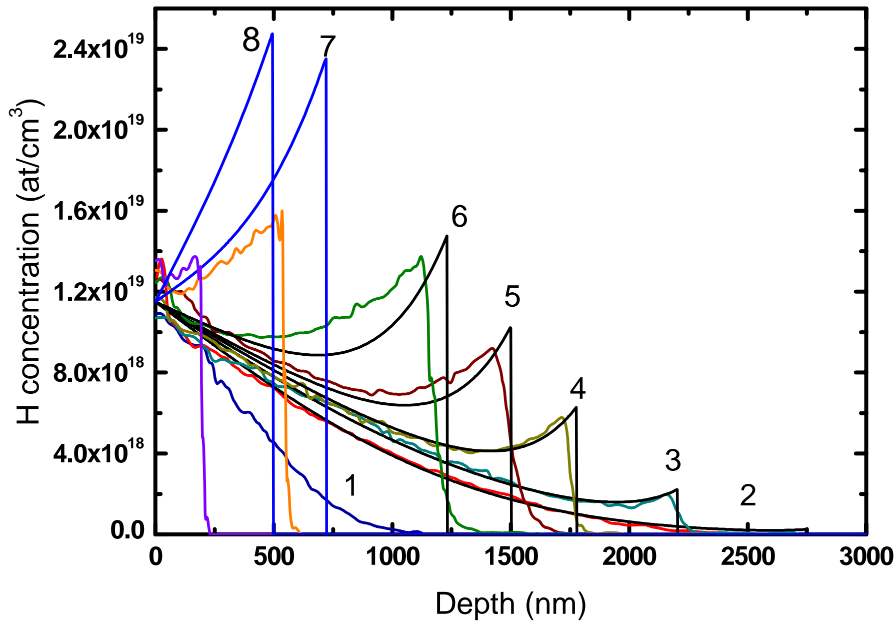

Figure A.3: *Our simulations (black and blue lines) compared to Roth's data (coloured lines) [Roth92] considering a constant diffusion.*

As the starting profile we considered the profile 1 of the Fig. A.1. We noted during different initial attempts of simulations that it is impossible to simulate correctly and simultaneously all partially regrown profiles with these assumptions. So we decided to divide the profiles in two groups: the first group is constituted by the profiles 2, 3, 4, 5 and 6 of Fig. A.1 and the second one by the profiles 7 and 8 of Fig. A.1. Optimizing only the last two profiles we found higher values of D_H and α with respect to the parameters values obtained considering all profiles or only the first group. This fact suggests that both D_H and α have to grow at higher concentrations. The change of α could be related to a change of H chemical state with time or concentration happening at concentration above the H solubility (~ 10^{19} at/cm^3) or may depend on the H_2 molecule formation. In this initial stage of the work, we preferred to exclude the last two profiles from the optimization and we focused our attention to the first six SIMS profiles in order to model correctly the low concentration regime before to study the high concentration one.

In Fig. A.3 the simulations, obtained optimizing model parameters considering only the first set of profiles, are shown. The profiles of the first group are represented by black lines, while the simulations of profiles 7 and 8 by blue lines. The profiles 2, 3 and 4 are reproduced very well, while we are underestimating the H diffusion in the amorphous bulk

(see simulations of the profiles 5 and 6). Considering a injection factor different from 0 it was possible to reduce the H concentration at the a-c interface with respect to simulations with α = 0 (not shown), even if the H diffusion is not again simulated correctly in the profiles 5 and 6. In conclusion, constant diffusion model does not succeed to simulate forward the profile 4.

The values of the parameters obtained are:

- D_H = 468.3 nm^2/s - α = 0.12
- v_0 = 1.48 nm/s - v_{lin} = 19.8 nm^4/s

The value of D_H has the same order of magnitude of Roth's value (~ 720 nm^2/s). The value of v_0 is included between the value estimated by Olson and Roth [Olson] (pre-factor of 3.1 x 10^{15} nm^2/s, E = 2.68 eV: v_0(606°C) = 1.34 nm/s) and the one estimated by Roth *et al.* [Roth90] (pre-factor of 4.64 x 10^{15} nm^2/s, E = 2.7 eV: v_0(606°C) = 1.54 nm/s). From the ratio between v_{lin} and v_0 we found 13.4 nm^3, a value that is lower than the experimental value of 16.5 nm^3 (Section A.2.2).

As we said in Section A.3, we tried to simulate Roth's data considering also a trap limited diffusion. The results of the best fits are shown in Fig. A.4.

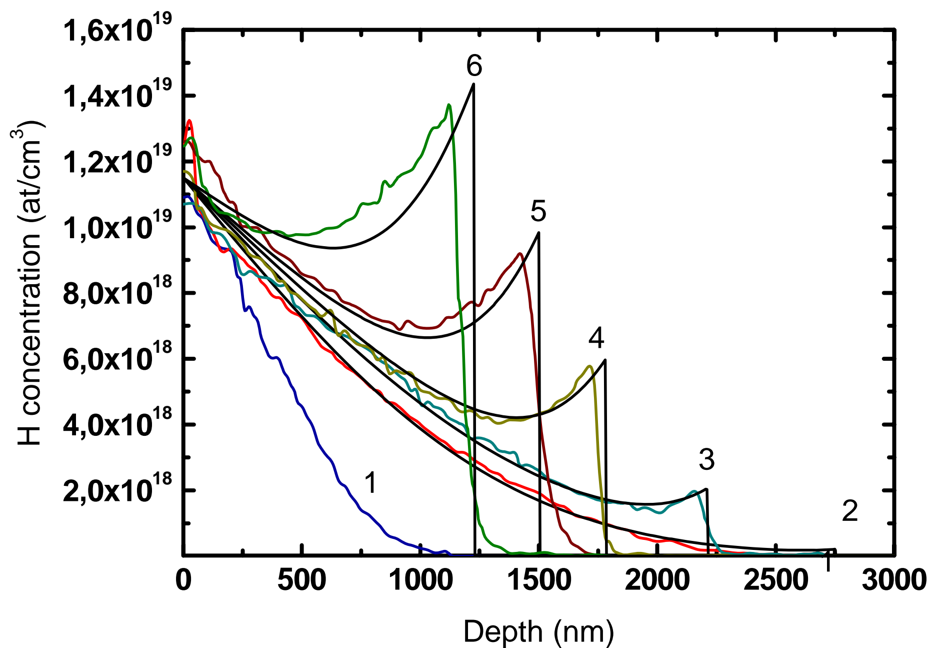

Figure A.4: *Our simulations (black lines) compared to Roth's data (coloured lines) [Roth92] considering a trap limited diffusion.*

Also in this case we are not able to simulate all profiles simultaneously, obtaining simulations of the profiles 7 and 8 with a bad level of accuracy, similar to these shown in Fig. A.3. For this reason we restricted our attention to the first group of profiles excluding the profiles 7 and

8 from the optimization and not reporting them in Fig. A.4. The simulations reproduce the experimental data very well. This model is able to predict the correct shape of diffusion both the profiles 2, 3 and 4 (as the constant diffusion model) and the profiles 5 and 6. The a-c interface positions are predicted with an average error of 23 nm.

The values of the parameters obtained are:

- $D = 526.3\ nm^2/s$ - $T_{bulk} = 8.0 \times 10^{18}\ at/cm^3$
- $k = 0.042$ - $\mu = 396\ nm$
- $\alpha = 0.064$
- $v_0 = 1.45\ nm/s$ - $v_{lin} = 23.1\ nm^4/s$

Also in this case the value of the diffusivity of the H free to move in a-Si has the same order of magnitude of Roth's value and the value of v_0 is compatible with previous esteems. From the ratio between v_{lin} and v_0 we found 15.9 nm^3, a value that is very compatible to the experimental value (16.5 nm^3). Observing the value of T_{bulk}, it is interesting to note that it is much higher than the peaks of the profiles 2, 3 and 4, whereas it is lower than the peaks of the profiles 5 and 6. This observation explains and confirms that something different happens in the profiles 5 and 6 compared with the other profiles supporting our hypothesis of a trap limited diffusion. It is interesting to compare H with F: both of them seems to undergo a trap limited diffusion and they retard the SPER rate, even if the different ways. In order to deepen this aspect of the diffusion problem, in Fig. A.5 we reported the simulation of the profile 6 shifted with a simple translation on depth, correcting slightly the annealing times to make easier a comparison with the experimental profile. The shift is reasonable within the error in the annealing times estimation. The simulation of the profile 2 is shown as reference.

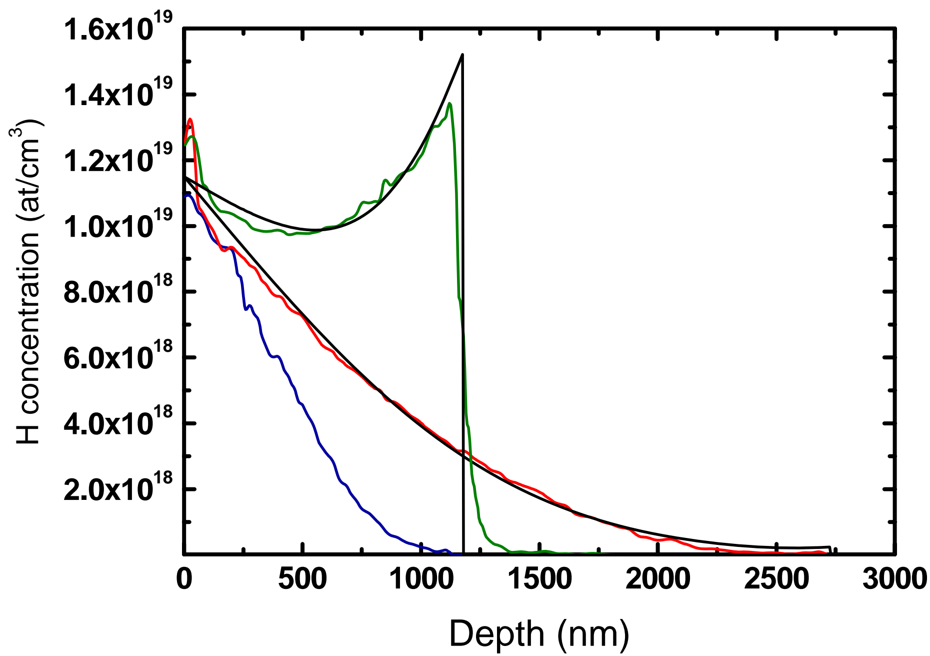

Figure A.5: *Simulations (black lines) of the profiles 2 and 6 compared to Roth's data (coloured lines) [Roth92] considering a trap limited diffusion and making a translation in depth on the profile 6.*

Introducing an arbitrary SIMS resolution on the peak of the profiles is possible to predict H concentration at the a-c interface correctly (Fig. A.6).

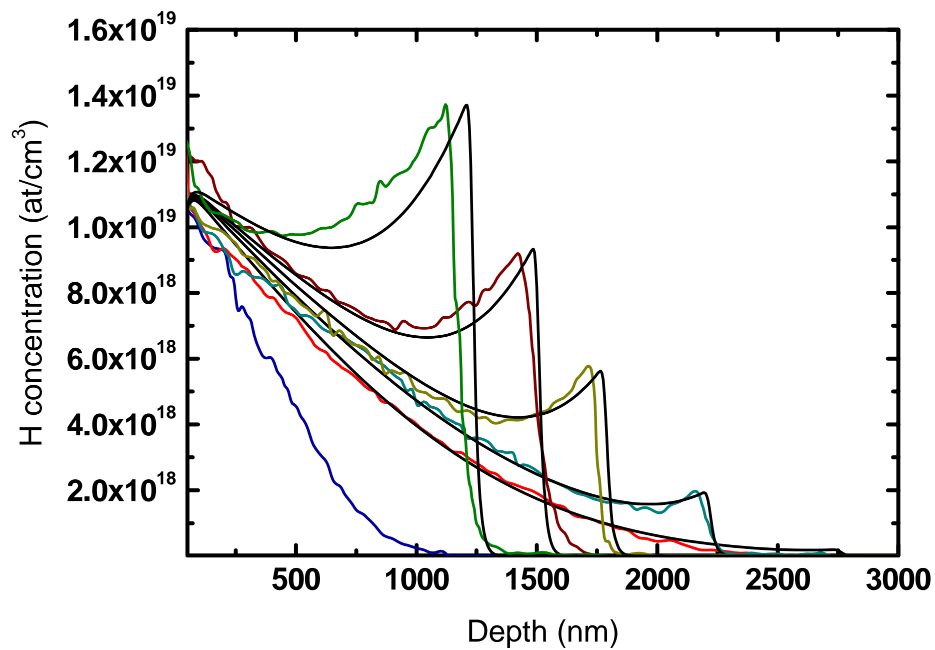

Figure A.6: *Our simulations (black lines) compared to Roth's data (coloured lines) [Roth92] considering a trap limited diffusion and a SIMS resolution.*

The trap limited diffusion seems to model correctly the H diffusion in the low concentration regime better than the constant diffusion. The correspondence between the peaks of the experimental profiles and their simulations is satisfactory.

A.5 CONCLUSION AND FUTURE WORK

In conclusion, we think that the trap limited diffusion model describes better the first six profiles of Roth *et al.*'s data than the constant diffusion model that underestimates the diffusion in a-Si in the profiles 4 and 5. Now we are able to model very well the low concentrations regime of the H-system, even if we simulated H chemical profiles only at one temperature. In the profiles 7 and 8 of Fig. A.1 something different happens and we are not able to model it. It would be necessary to study deeply the literature about high concentration of H in a-Si and design an ad hoc experiment to characterize H redistribution during Si SPER in a wide range of H concentration and SPER temperatures, as we did for the "F-system". We approached the "H-system" finding the above preliminary results in a relatively short time only thanks to the experimental and theoretical approach already developed to study the F redistribution during Si SPER.

References

[Abdulmalik] D. A. Abdulmalik, P. G. Coleman, H. A. W. El Mubarek and P. Ashburn, J. Appl. Phys. **102,** 013530 (2007).

[Ankudinov] A. L. Ankudinov, B. Ravel, J. J. Rehr, and S. D. Conradson, Phys. Rev. B. **58**, 7565 (1998).

[Aziz] M. J. Aziz, P. C. Sabin and G.-Q. Lu, Phys. Rev. B **44**, 9812 (1991).

[Baggio] N. Baggio, Thesis *"Analisi dell'intorno atomico del fluoro incorporato in silicio cristallino"* (2007).

[Bernstein98] N. Bernstein, M. J. Aziz and E. Kaxiras, Phys. Rev. B **58**, 4579 (1998).

[Bernstein00] N. Bernstein, M. J. Aziz and E. Kaxiras, Phys. Rev. B **61**, 6696 (2000).

[Bernstein06] N. Bernstein, J. L. Feldman, and M. Fornari, Phys. Rev. B **74**, 205202 (2006).

[Bonafos] C. Bonafos, D. Mathiot and A. Claverie, J. Appl. Phys. **83**, 3008 (1998).

[Boninelli06] S. Boninelli, A. Claverie, G. Impellizzeri, S. Mirabella, F. Priolo, E.Napolitani and F. Cristiano, Appl. Phys. Lett. **89**, 171916 (2006).

[Boninelli08] S. Boninelli, G. Impellizzeri, S. Mirabella, F. Priolo, E. Napolitani, N. Cherkashin and F. Cristiano, Appl. Phys. Lett. **93**, 061906 (2008).

[Bracht95] H. Bracht, N. A. Stolwij and H. Mehrer, Phys. Rev. B **52**, 16542 (1995).

[Bracht00] H. Bracht, Mater. Res. Soc. Bull. **25**, 22 (2000).

[Bracht07] H. Bracht, Phys. Rev. B, **75**, 035210 (2007); H. Bracht, H. H. Silvestri, I. D. Sharp and E. E. Haller, Phys. Rev. B, **75**, 035211 (2007).

[Bruno07] E. Bruno, S. Mirabella, F. Priolo, E. Napolitani, C. Bongiorno and V. Raineri, J. Appl. Phys. **101**, 0235115 (2007).

[Bruno07b] E. Bruno, S. Mirabella, E. Napolitani, F. Giannazzo, V.Raineri and F. Priolo, Nucl. Instrum. Methods B **257**, 181 (2007).

[Chao] H. S. Chao, P. B. Griffin, J. D. Plummer and C. S. Rafferty, Appl. Phys. Lett. **69**, 2113 (1996).

[Chu] H. Chu, J.J. Yang and L.J. Chen, Nucl. Instrum. Methods B **74**, 138 (1993).

[Claverie] A. Claverie, B. Colombeau, B. De Maudit, C. Bonafos, X. Hebres, G. Ben Assayag and F. Cristiano, Appl. Phys. A **76**, 1025 (2003).

[Coffa] S. Coffa, F. Priolo, and A. Battaglia, Phys. Rev. Lett. **70**, 3756 (1993).

[Cowern90] N. E. B. Cowern, K. T. F. Janssen, G. F. A. Van del Walle, D. J. Gravesteijn, Phys. Rev. Lett. **65**, 2434 (1990).

[Cowern91] N. E. B. Cowern, G. F. A. Van der Walle, D. J. Gravesteijn, C. J. Vriezema, Phys. Rev. Lett. **67**, 212 (1991).

[Cowern99] N. E. B. Cowern, G. Mannino, P. A. Stolk, M. J. J. Theunissen, Mater. Res. Soc. Symp. Proc. **568**, 79 (1999).

[Cowern99b] N. E. B. Cowern, G. Mannino, P. A. Stolk, F. Roozeboom, H. G. A. Huizing, J. G. M. van Berkum, F. Cristiano, A. Claverie and M. Jaraiz, Phys. Rev. Lett. **82**, 4460 (1999).

[Cowern00] N. E. B. Cowern and C. Rafferty, Mater. Res. Soc. Bull. **25**, 39 (2000).

[Cowern05] N. E. B. Cowern, B. Colombeau, J. Benson, A. J. Smith, W. Lerch, S. Paul, T. Graf, F. Cristiano, X. Hebras and D. Bolze, Appl. Phys. Lett. **86**, 101905 (2005).

[Cristiano] F. Cristiano, N. Cherkashin, P. Calvo, Y. Lamrani, X. Hebras, A. Claverie and W. Lerch, S. Paul, Mater. Sci. Eng. B **114–115**, 174 (2004).

[Csepregi75] L. Csepregi, J. W. Mayer and T. W. Sigmon, Phys. Lett. A **54**, 157 (1975).

[Csepregi77] L. Csepregi, E. F. Kennedy, T. J. Gallagher, J. W. Mayer and T. W. Sigmon, J. Appl. Phys. **48**, 4234 (1977).

[Custer] J. S. Custer, M. O. Thompson, D. C. Jacobson, J. M. Poate, S. Roorda, W. C. Sinke and F. Spaepen, Appl. Phys. Lett. **64**, 43 (1994).

[D’Angelo] D. D’Angelo, L. Romano, I. Crupi, E. Carria, V. Privitera and M. G. Grimaldi, Appl. Phys. Lett. **93**, 231901 (2008).

[DeSalvador05] D. De Salvador, E. Napolitani, G. Bisognin, A. Carnera, E. Bruno, S. Mirabella, G. Impellizzeri and F. Priolo, Appl. Phys. Lett. **87**, 221902 (2005).

[DeSalvador06] D. De Salvador, E. Napolitani, S. Mirabella, G. Bisognin, G. Impellizzeri, A. Carnera, F. Priolo, Phys. Rev. Lett. **97**, 255902 (2006).

[DeSalvador06b] D. De Salvador, G. Bisognin, M. Di Marino, E. Napolitani, A. Carnera, H. Graoui, M. A. Foad, F. Boscherini and S. Mirabella, Appl. Phys. Lett. **89**, 241901 (2006).

[DeSalvador09] D. De Salvador, G. Bisognin, E. Napolitani, **M. Mastromatteo**, N. Baggio, A. Carnera, F. Boscherini, G. Impellizzeri, S. Boninelli, F. Priolo, and F. Cristiano, Appl. Phys. Lett. **95**, 101908 (2009).

[Di Marino] M. Di Marino, E. Napolitani, **M. Mastromatteo**, G. Bisognin, D. De Salvador, A. Carnera, S. Mirabella, G. Impellizzeri, F. Priolo H. Graoui and M. A. Foad, Nucl. Instrum. Methods Phys. Res. B **253**, 46 (2006).

[Diebel04] M. Diebel and S.T. Dunham, Phys. Rev, Lett. **93**, 245901 (2004).

[Diebel06] M. Diebel and S.T. Dunham , Phys. Rev. Lett. **96**, 039602 (2006).

[Downey] D. F. Downey, J. W. Chow, E. Ishida and K. S. Jones, Appl. Phys. Lett. **73**, 1263 (1998).

[Eaglesham94] D. J. Eaglesham, P. A. Stolk, H. –J. Gossmann and J. M. Poate, Appl. Phys. Lett. **65**, 2305 (1994).

[Eaglesham95] D. J. Eaglesham, P. A. Stolk, H. –J. Gossmann, T. E. Haynes and J. M. Poate, Nucl. Instrum. Methods B **106**, 191 (1995).

[Edelman] L. A. Edelman, S. Jin, K. S. Jones, R. G. Elliman and L. M. Rubin, Appl. Phys. Lettt. **93**, 072107 (2008).

[El Mubarek03] H. A. W. El Mubarek and P. Ashburn, Appl. Phys. Lett. **83**, 4134 (2003).

[El Mubarek04] H. A. W. El Mubarek, J. M. Bonar, G. D. Dilliway, P. Ashburn, M. Karunaratne, A. F. Willoughby, Y. Wang, P. L. F. Hemment, R. Price, J. Zhang and P. Ward, J. Appl. Phys. **96**, 4114 (2004).

[Fahey] P. M. Fahey, P. B. Griffin and J. D. Plummer, Rev. Mod. Phys. **61**, 289 (1989).

[FEFF] B. Ravel and M. Newville, J. Synchrotron Radiat. **12**, 537 (2005).

[Fiorentini] V. Fiorentini and G.M. Lopez, Phys. Rev. Lett. **96**, 039601 (2006).

[Fuse] G. Fuse, T. Hirao, K. Inoue, S. Takayanagi and Y. Yaegashi, J. Appl. Phys. **53**, 3650 (1982).

[Giles91] M. D. Giles, J. Electrochem. Soc. **138**, 1160 (1991).

[Gösele] U. Gösele, P. Laveant, R. Scholz, N. Engler and P. Werner, Mater. Res. Soc. Symp. Proc., **610**, B7.1 (2000).

[Ho] C. P. Ho, J. D. Plummer, S. E. Hansen, and R. Dutton, IEEE Electron Devices **ED-30**, 1438 (1983).

[Hu] S. M. Hu, Mater. Sci. Eng. Rep. **R13**, 105 (1994).

[Impellizzeri04] G. Impellizzeri, J. H. R. dos Santos, S. Mirabella, F. Priolo, E. Napolitani and A. Carnera, Appl. Phys. Lett. **84**, 1862 (2004).

[Impellizzeri05] G. Impellizzeri, J. H. R. dos Santos, S. Mirabella, E. Napolitani, A. Carnera and F. Priolo, Nucl. Instrum. Methods B **230**, 220 (2005).

[Impellizzeri06] G. Impellizzeri, S. Mirabella, E. Bruno, F. Priolo, E. Napolitani and A. Carnera, J. Vac. Sci. Technol. B **24**, 433 (2006).

[Impellizzeri06b] G. Impellizzeri, S. Mirabella, F. Priolo, E. Napolitani and A. Carnera, Nucl. Instrum. Methods B **253**, 94 (2006).

[Impellizzeri06c] G. Impellizzeri, S. Mirabella, L. Romano, E. Napolitani, A. Carnera and F. Priolo, Nucl. Instrum. Methods B **242**, 614 (2006).

[Impellizzeri07] G. Impellizzeri, S. Mirabella, A. M. Piro, M. G. Grimaldi, F. Priolo, F. Giannazzo, V. Raineri, E. Napolitani, and A. Carnera, Appl. Phys. Lett. **91**, 132101 (2007).

[ITRS] The International Technology Roadmap for Semiconductors, 2007, www.itrs.net.

[Jacques] J. M. Jacques, L. S. Robertson, K. S. Jones, M. E. Law, M. Rendon and J. Bennett, Appl. Phys. Lett. **82**, 3469 (2003).

[Jeng] S. –P. Jeng, T. –P. Ma, R. Cantieri, M. Anderle and G. W. Rubloff, Appl. Phys. Lett. **61**, 1310 (1992).

[Jin] J. Y. Jin, J. Liu, U. Jeong, S. Metha and K. Jones, J. Vac. Sci. Tecnol. B **20**, 422 (2002).

[Johnson04] B. C. Johnson and J. C. McCallum, J. Appl. Phys. **95**, 4427 (2004).

[Johnson07] B. C. Johnson and J. C. McCallum, Phys. Rev. B **76**, 045216 (2007).

[Johnson09] B. C. Johnson, P. Caradonna, D. J. Pyke, J. C. McCallum and P. Gortmaker, Thin Solid Films, *corrected proof,* doi:10.1016/j.tsf.2009.09.145 (2009).

[Jones] K.S. Jones, L. H: Zhang, V. Krishnamoorthy, M. Law, D. S. Simmons, P. Chi., L. Rubin and R. G. Elliman Appl. Phys. Lett. **68**, 2672 (1996).

[Kennedy] E. F. Kennedy, L. Csepregi, J. W. Mayer and T. W. Sigmon, J. Appl. Phys. **48**, 4241 (1977).

[Kham05] M. N. Kham, H. A. W. El Mubarek, J. M. Bonar and P. Ashburn, Appl. Phys. Lett. **87**, 011902 (2005).

[Kham07] M. N. Kham, I. Matko, B. Chenevier and P. Ashburn, J. Appl. Phys. **102**, 113718 (2007).

[Kilpeläinen09] S. Kilpeläinen, K. Kuitunen, F. Tuomisto, J. Slotte, E. Bruno, S. Mirabella and F. Priolo, Semic. Sci. Tech. **24**, 015005 (2009).

[Kilpeläinen09b] S. Kilpeläinen, K. Kuitunen, J. Slotte, F. Tuomisto, E. Bruno, S. Mirabella and F. Priolo, Mater. Sci. Eng. B **159**, 164 (2009).

[Kumeda] M. Kumeda, Y. Takahashi and T. Shimizu, Phys. Rev. B **36**, 2713 (1987).

[Lamberti] *Characterization of Semiconductor Heterostructures and Nanostructures*, edited by C. Lamberti (Elsevier, New York, 2008).

[Lau] F. Lau, L. Mader, C. Mazure, Ch. Werner and M. Orlowski, Appl. Phys. A **49**, 671 (1989).

[Lerch] W. Lerch, S. Paul, J. Niess, S. McCoy, T. Selinger, J. Gelpey, F. Cristiano, F. Severac, M. Gavelle, S. Boninelli, P. Pichler and D. Bolze, Mater. Sci. Eng. B **124**, 24 (2005).

[Lide] *Handbook of Chemistry and Physics*, 71st ed. edited by D. R. Lide (CRC Press, Boston, 1990), pp. 9-86–9-89.

[Lopez05] G. M. Lopez, V. Fiorentini, G. Impellizzeri, S. Mirabella and E. Napolitani, Phys. Rev. B **72**, 045219 (2005).

[Lopez06] G. M. Lopez and V. Fiorentini, Appl. Phys. Lett. **89**, 092113 (2006).

[Lu90] G. Q. Lu, E. Nygren, M. J. Aziz and D. Turnbull, Appl. Phys. Lett. **56**, 137 (1990).

[Lu91] G. Q. Lu, E. Nygren and M. J. Aziz, J. Appl. Phys. **70**, 5323 (1991).

[Mannino] G. Mannino, N.E.B. Cowern, F. Roozeboom and, J.G.M. van Berkum, Appl. Phys. Lett. **76**, 855 (2000).

[Masao] A. Masao and W. N. Lipscomb, Acta Crystallogr. **7**, 597 (1954).

[Mastromatteo] M. Mastromatteo, thesis, *"Studio della realizzazione di giunzioni elettriche ultrasottili in silicio per dispositive CMOS avanzati"* (2006).

[MBE] M. A. Herman and H. Sitter, in *Molecular Beam Epitaxy, Fundamentals and Current Status* (Springer, Berlin, 1996).

[Michel] A. E. Michel, W. Rausch, P. A. Ronsheim and R. H. Kasti, Appl. Phys. Lett. **50**, 416 (1987).

[Mirabella02] S. Mirabella, A Coati, D. De Salvador, E. Napoletani, A. Mattoni, G. Bisognin, M. Berti, A. Carnera, A. V. Drigo, S. Scalese, S. Pulvirenti, A. Terrasi and F. Priolo, Phys. Rew. B, **65**, 045209 (2002).

[Mirabella03] S. Mirabella, E. Bruno, F. Priolo, D. De Salvador, E. Napolitani, A. V. Drigo and A. Carnera, Appl. Phys. Lett. **83**, 680 (2003).

[Mirabella05] S. Mirabella, G. Impellizzeri, E. Bruno, L. Romano, M. G. Grimaldi, F. Priolo, E. Napolitani and A. Carnera, Appl. Phys. Lett. **86**, 121905 (2005).

[Mirabella06] S. Mirabella, E. Bruno, F. Priolo, F. Giannazzo, C. Bongiorno, V. Raineri, E. Napolitani and A. Carnera, Appl. Phys. Lett. **88**, 191910 (2006).

[Mokhberi] A. Mokhberi, R. Kasnavi, P. B. Griffin and J. D. Plummer, Appl. Phys. Lett. **80**, 3530 (2002).

[Moroz] V. Moroz, Y. S. Oh, D. Pramanik, H. Graoui and M. A. Foad, *Appl. Phys. Lett*. **87**, 051908 (2005).

[Napolitani99] E. Napolitani, A. Carnera, E. Schroer, V. Privitera, F. Priolo and S. Moffatt, Appl. Phys. Lett. **75**, 1869 (1999).

[Napolitani01] E. Napolitani, A. Coati, D. De Salvador, A. Carnera, S. Mirabella, S.Scalese and F. Priolo, Appl. Phys. Lett. **79**, 4145 (2001).

[Nash] G. R. Nash, J. F. W. Schiz, C. D. Marsh, P. Ashburn, and G. R. Booker, Appl. Phys. Lett. **75**, 3671 (1999).

[Nieh] C.W. Nieh e L.J. Chen, Appl. Phys. Lett. **48**, 1528 (1986).

[Nygren] E. Nygren, M.J. Aziz and D. Turnbull, Appl. Phys. Lett. **47,** 232 (1985).

[Oberlin] J. C. Oberlin, A. C. Chami, E. Ligeon and, C. Prunier, Nucl. Instr. Meth. B **19**, 462 (1987).

[Olson] G. L. Olson and J. A. Roth, Mater. Sci. Rep. **3**, 1 (1988).

[OlsonHB] G. Olson, J. Roth, in: D.Hurle (Ed.),Handbook of Crystal Growth, vol. **3**, Elsevier Science B.V, chap. 7, p. 255, (1994).

[Orlowski] M. Orlowski, Appl. Phys. Lett. **55**, 1762 (1989).

[Pantelides] T. S. Pantelides, Phys. Rev. Lett. **57**, 2979 (1986).

[Park96] B. Park, Jpn. J. Appl. Phys. **35**, L 1611 (1996).

[Park99] Y.-J. Park and J.-J. Kim, J. Appl. Phys. **85**, 803 (1999).

[Pawlak04] B. J. Pawlak, R. Surdeanu, B. Colombeau, A. J. Smith, N. E. B. Cowern, R. Lindsay, W. Vandervost, B. Brijs, O. Richard and F. Cristiano, Appl. Phys. Lett. **84**, 2055 (2004).

[Pawlak05] B. J. Pawlak, W. Vandervost, A. J. Smith, N. E. B. Cowern, B. Colombeau and X. Pages, Appl. Phys. Lett. **86**, 101913 (2005).

[Pelaz] L. Pelaz, G. H. Gilmer, M. Jaraiz, S. B. Herner, H. –J. Gossmann, D. J Eaglesham, G. Hobler, C. S. Rafferty and J. Barbolla, Appl. Phys. Lett. **73**, 1421 (1998).

[Pfann] W. G. Pfann, *Zone Melting* (Wiley, New York, 1958).

[Pi] X.D. Pi, C.P. Burrows and P.G. Coleman, Phys. Rev. Lett. **90**, 155901 (2003).

[Priolo90] F. Priolo, C. Spinella and E. Rimini, Phys. Rev. B **41**, 5235 (1990).

[Rimini] E. Rimini, in *Ion Implantation: Basics to Device Fabrication* (Kluwer academic Publishers, Boston, 1995), and references therein.

[Roorda] S. Roorda, W. C. Sinke, J. M. Poate, D. C. Jacobson, S. Dierker, B. S. Dennis, D. J. Eaglesham, F. Spaepen, and P. Fuoss, Phys. Rev. B **44**, 3702 (1991).

[Roth90] J. A. Roth, G. L. Olson, D. C. Jacobson and J. M. Poate, Appl. Phys. Lett. **57**, 1340 (1990).

[Roth92] J. A. Roth, G. L. Olson, D. C. Jacobson, J. M. Poate and C. Kirschbaum, Mater. Res. Soc. Symp. Proc. **205**, 45 (1992).

[Roth93] J. A. Roth, G. L. Olson, D. C. Jacobson and J. M. Poate, Mater. Res. Soc. Symp. Proc. **297**, 291 (1993).

[Rudawski08] N. G. Rudawski, K. S. Jones and R. Gwilliam, Phys. Rev. Lett. **100**, 165501 (2008).

[Rudawski08b] N. G. Rudawski, K. S. Jones and R. Gwilliam, Mater. Sci. and Eng. R **61**, 40 (2008).

[Rudawski09] N. G. Rudawski, K. S. Jones, S. Morarka, M. E. Law, and R. G. Elliman, J. Appl. Phys. **105**, 081101 (2009).

[Rücker] H. Rücker, B. Heinemann, W. Röpke, R. Kurps, D. Krüger, G. Lippert and H. J. Osten, Appl. Phys. Lett, **73**, 1682 (1998).

[Sadigh] B. Sadigh, T. J. Lenosky, S. K. Theiss, M. –J. Caturla, T. D. de la Rubia and M. A. Foad, Phys. Rev. Lett. **83**, 4314 (1999).

[Saito81] T. Saito and I. Ohdomari, Philos. Mag. B **43**, 673 (1981).

[Saito84] T. Saito and I. Ohdomari, Philos. Mag. B **49**, 471 (1984).

[Saleh] H. Saleh, M. E. Law, S. Bharatan, K. S. Jones, V. Krishnamoorthy and T. Buyuklimanli, Appl. Phys. Lett. **77**, 112 (2000).

[Sands] T. Sands, J. Washburn, R. Gronsky, W. Maszara, D.K. Sadana and G.A. Rozgonyi, Appl. Phys. Lett. **45**, 982 (1984).

[Scholz] R. Scholz, U. Gösele, J.-Y Huh and T.Y. Jan, Appl. Phys. Lett. **72**, 200 (1998).

[Shao] L. Shao, J. Liu, Q. Y. Chen, W. –K. Chu, Mater. Sci. and Engin. R **42**, 65 (2003).

[Shauly] E.N. Shauly and S. Lachman-Shalem, J. Vac. Sci. Technol. B **22**, 592 (2004).

[Simpson] P.J. Simpson, Z. Jenei, P. Asoka-Kumar, R.R. Robison and M.E. Law, Appl. Phys. Lett. **85**, 1538 (2004).

[Smith55] V. G. Smith, W. A. Tiller and J. W. Rutter, Can. J. Phys. **33**, 723 (1955).

[Smith06] A. J. Smith, N. E. B. Cowern, R. Gwilliam, B. J. Sealy, B. Colombeau, E. J. H. Collart, S. Gennaro, D. Giubertoni, M. Bersani and M. Barozzi, Appl. Phys. Lett. **88**, 082112 (2006).

[Solmi90] S. Solmi, E. Landi, and F. Baruffaldi, J. Appl. Phys. **68**, 3250 (1990).

[Solmi91] S. Solmi, F. Baruffaldi and R. Canteri, J. Appl. Phys. **69**, 2135 (1991).

[Spaepen] F. Spaepen, Acta Metall. **26**, 1167 (1978).

[Stefan] M. Stefan, Thesis in Physics, *"Processi termici rapidi su materiali semiconduttori"*.

[Stillinger] F. H. Stillinger and T. A. Weber, J. Chem. Phys. **88**, 5123 (1988).

[Stolk95] P. A. Stolk, D. J. Eaglesham, H.-J. Gossman e J. M. Poate, Appl. Phys. Lett. **66**, 1370 (1995).

[Stolk97] P. A. Stolk, J. H.-J. Gossmann, D. J. Eaglesham, D. C. Jacobson, C. S. Rafferty, G. H. Gilmer, M. Jaraìz, J. M. Poate, H. S. Luftman and T. E. Haynes, J. Appl. Phys. **81**, 6031 (1997).

[Suni82] I. Suni, G. Goltz, M. G. Grimaldi and M. –A. Nicolet, Appl Phys. Lett. **40**, 269 (1982).

[Suni82b] I. Suni, G. Goltz and M. –A. Nicolet, Thin Solid Films **93**, 171 (1982).

[Suni84] I. Suni, U. Shreter, M-A. Nicolet, J. E. Baker, J. Appl. Phys. **56**, 273 (1984).

[Takeda] S. Takeda, Jpn. J. Appl. Phys., Part 2: Lett. **30**, L639 (1991).

[TRIM] J. F. Ziegler, J. P. Biersack, U. Littmark, *Stopping and Ranges of Ions in Matter,* New York: Pergamon (1985).

[Tsai] M. Y. Tsai, D. S. Day, B. G. Streetman, P. Williams and C. A. Evans, Jr., J.Appl. Phys. **50**, 188 (1979).

[Urli] X. Urli, C. L. Dias, L. J. Lewis and S. Roorda, Phys. Rev. Lett. **77**, 155204 (2008).

[van den Hoven] G. N. van den Hoven, Z. N. Liang, L. Niesen and J. S. Custer, Phys. Rev. Lett. **68**, 3714 (1992).

[van der Walle] C. G. van der Walle, F. R. McFeely and S. T. Pantelies, Phys. Rev. Lett. **61**, 1867 (1988).

[Werner] M. Werner, H. Mehrer and H. D. Hochheimer, Phys. Rev. B **32**, 3930 (1985).

[Williams] J.S. Williams and R.G. Elliman, Phys. Rev. Lett. **51**, 1069 (1983).

[Wilson] R.G. Wilson, J. Appl. Phys. **54**, 6879 (1983).

[Wormington] M. Wormington, C. Panaccione, K. M. Matney and K. Bowen, Phil. Trans. R. Soc. Lond. A 357, 2827 (1999).

[Windl] W. Windl, M. M. Bunea, R. Stumpf, S. T. Dunham and M. P. Masquelier, Phys. Rev. Lett. **83**, 4345 (1999).

[Wu] I.W. Wu e L.J. Chen, J. Appl. Phys. **58**, 3032 (1985).

[Zhang] J. Zhang, Y. Ashizawa, and H. Oka, *Proc. IWJT. Tech. Dig*. **50** (2006).

[Zographos] N. Zographos and I. Martin-Bragado, Mater. Res. Soc. Symp. Proc. **1070**, E03-01 (2008).

List of publications

Papers

1. **M. Mastromatteo**, D. De Salvador, E. Napolitani, G. Bisognin, A. Carnera, G. Impellizzeri, S. Mirabella and F. Priolo, "Fluorine redistribution and incorporation during solid phase epitaxial of pre-amorphized Si" *submitted for publication in Phys. Rev. B*

2. E. Napolitani, G. Bisognin, **M. Mastromatteo,** D. De Salvador, A. Carnera, C. Spinella, E. Bruno, S. Boninelli, G. Scapellato, S. Mirabella and F. Priolo, "Transient Enhanced Diffusion of B in pre-amorphized Ge" *submitted for publication in Appl. Phys. Lett.*

3. E. Bruno, S. Mirabella, G. Scapellato, G. Impellizzeri, A. Terrasi, F. Priolo, E. Napolitani, D. De Salvador, **M. Mastromatteo**, A. Carnera, "Radiation enhanced diffusion of B in crystalline Ge", Thin Solid Films *in press, corrected proof* doi:10.1016/j.tsf.2009.09.173 (2010)

4. G. Bisognin, S. Vangelista, **M. Mastromatteo**, E. Napolitani, D. De Salvador, A. Carnera, M. Berti, E. Bruno, G. Scapellato, A. Terrasi "Defects in Ge caused by sub-amophizing self-implantation: formation and dissolution", Thin Solid Films *in press, corrected proof* doi:10.1016/j.tsf.2009.09.136 (2010)

5. D. De Salvador, G. Bisognin, E. Napolitani, **M. Mastromatteo**, N. Baggio, A. Carnera, F. Boscherini, G. Impellizzeri, S. Mirabella, S. Boninelli, F. Priolo, F. Cristiano, "Formation and incorporation of SiF_4 molecules in F-implanted preamorphized silicon", Applied Physics Letter 95, 101908 (2009)

6. E. Bruno, S. Mirabella, G. Scapellato, G. Impellizzeri, A. Terrasi, F. Priolo, E. Napolitani, D. De Salvador, **M. Mastromatteo**, A. Carnera, "Mechanism of B diffusion in cristalline Ge under proton irradiation", Physical Review B 80, 033204 (2009)

7. M. Di Marino, E. Napolitani, **M. Mastromatteo**, G. Bisognin, D. De Salvador, A. Carnera, S. Mirabella, G. Impellizzeri, F. Priolo, H. Graoui, M. A. Foad, "B diffusion

and activation phenomena during post-annealing of C co-implanted ultra-shallow junctions", Nuclear Instruments and Methods in Physics Research B vol. 253, pages 46-49 (2006)

Oral presentation

1. **M. Mastromatteo**, E. Napolitani, D. De Salvador, G. Bisognin, , A. Carnera, G. Impellizzeri, S. Mirabella, S. Boninelli, F. Priolo, F. Cristiano, Presentazione orale al congresso European Materials Research Society, Symposium I, dal titolo "Fluorine diffusion and clustering in amorphous silicon during solid phase epitaxial regrowth" 2009

Posters

1. D. De Salvador, G. Bisognin, E. Napolitani, **M. Mastromatteo**, N. Baggio, A. Carnera, F. Boscherini, G. Impellizzeri, S. Mirabella, S. Boninelli, F. Priolo, F. Cristiano, XAFS Conference, July 36-31 2009, Camerino (Italy) poster session, "Formation of SiF_4-filled cavities in silicon: a soft X-ray absorption study"
2. G. Bisognin, S. Vangelista, **M. Mastromatteo**, E. Napolitani, D. De Salvador, A. Carnera, M. Berti, E. Bruno. G. Scapellato, A. Terrasi, European Materials Research Society 2009 poster session Symposium I, "Formation and dissolution kinetics of defects in Ge caused by sub-amorphizing self-implantation"
3. D. De Salvador, G. Bisognin, E. Napolitani, **M. Mastromatteo**, N. Baggio, A. Carnera, F. Boscherini, G. Impellizzeri, S. Mirabella, S. Boninelli, F. Priolo, F. Cristiano, European Materials Research Society 2009 poster session Symposium R, "XAFS investigation of F incorporation in Si"
4. **M. Mastromatteo**, E. Napolitani, D. De Salvador, F. Panciera, A. Carnera, G. Impellizzeri, S. Mirabella, F. Priolo, European Materials Research Society 2008 poster session, "Mechanism of fluorine segregation and in corporation during solid phase epitaxy of pre-amorphized silicon"

Ringraziamenti

Alla fine di questa tesi rivolgo un ringraziamento a tutte quelle persone che mi hanno sostenuto, spronato, insegnato ad andare sempre più a fondo nella comprensione di questa tematica di ricerca e che mi hanno trasmesso la forza di proseguire in questa affascinante ricerca.

Comincio ringraziando Enrico Napolitani, mio supervisore in questa tesi, per la fiducia che ha avuto nei miei confronti fin dai tempi della mia prima tesi di laurea, per avermi sempre spronato ad andare sempre più a fondo nella comprensione fisica di quello che studiavo e il continuo sostegno che da lui ho ricevuto anche in quei momenti che la vita rende difficili per tutti. Gli sarò sempre riconoscente per questo e non lo dimenticherò mai.

Voglio ringraziare Davide De Salvador per l'aiuto, il supporto e la pazienza che ha avuto nei miei confronti durante tutti i nostri colloqui, e anche per avere scritto il codice (e le sue innumerevoli versioni!) con il quale abbiamo potuto testare il nostro modello.

Sia ad Enrico che a Davide voglio fare un ulteriore ringraziamento comune: la gran parte di quello che ho imparato del lavoro di fisico lo devo esclusivamente a voi due. In questi anni ho potuto sviluppare insieme a voi sia l'aspetto sperimentale che teorico di tutte le tematiche che affrontavamo, riuscendo con il tempo a maturare sempre più una visione globale in senso fisico del problema affrontato. Inoltre vedendovi collaborare e sostenervi a vicenda ho avuto la più bella lezione su cosa significa il lavoro di gruppo. Non è stato facile per me nei primi tempi stare al vostro passo, ma fin da subito quello è stato il mio principale obiettivo. E, sebbene qualche passo avanti l'ho compiuto, tanto studio e molta strada dovrò ancora fare.

Non posso non ringraziare Gabriele Bisognin per l'appoggio e l'aiuto che mi ha sempre fornito con pazienza, competenza e cortesia.

Al Prof. Carnera, oltre a ringraziarlo per avermi accolto fin dalla prima tesi nel suo gruppo di ricerca e per i suoi preziosi suggerimenti, voglio fare i complimenti per il bel gruppo di persone che con il tempo ha saputo creare sia da un punto di vista scientifico, che soprattutto umano.

Voglio ringraziare il centro di ricerca MATIS-CNR INFM a cui afferisco e in particolare il Prof. Francesco Priolo, Giuliana Impellizzeri, Salvo Mirabella, Elena Bruno, Emanuele Francesco Pecora, Simona Boninelli per la loro amicizia, il loro aiuto e il tempo trascorso insieme ogni volta che ne abbiamo avuto occasione.

I would like to thank Brett C. Johnson for his friendship and the interesting discussions, that we did in Strasbourg and by emails.

Voglio anche ringraziare tutte quelle persone con le quali ho trascorso la maggior parte del mio tempo in Dipartimento. Grazie ad Annamaria Zaltron, Maria Vittoria Ciampollillo, Silvia Vangelista, Luca Bacci, Nicola Baggio, Maurizio Pesce, Ruggero Milazzo, Nicola Argiolas, Marco Bazzan, Cinzia Sada, Tiziana Cesca, Prof. Andrea Gasparotto, Prof. Marina Berti, e infine l'insostituibile Renzo Storti.

Colgo l'occasione per rendere grazie alla mia famiglia: a mia madre Lucia, alle mie sorelle Francesca e Angela, a mio cognato Alberto. Grazie per avermi sostenuto sempre e non avermi fatto mai mancare il vostro appoggio incondizionato. Ha significato molto per me. E questo mio lavoro è anche dedicato alla memoria di mio padre Michele.

Grazie a tutti coloro che ho incontrato e conosciuto in questi tre anni: dai miei coinquilini ai compagni delle diverse Scuole di Dottorato a cui ho partecipato, cosi come ai nuovi amici padovani. Dal continuo confronto reciproco ho imparato molto.

Un ringraziamento speciale e particolare va fatto alle "Pelli Sintetiche Family" e a tutti quelle persone che sentono di farne parte. Voi avete saputo accogliermi e donarmi la vostra amicizia, regalandomi un nuovo stile con cui affrontare la vita, più semplice e sereno verso il prossimo e il futuro. Grazie!